

FABRICATION, THERMAL STABILITY AND MECHANICAL
CHARACTERIZATION OF ELECTRODEPOSITED
NANOCRYSTALLINE FACE CENTERED CUBIC NI-FE ALLOYS

By

HONGQI LI

A DISSERTATION PRESENTED TO THE GRADUATE SCHOOL
OF THE UNIVERSITY OF FLORIDA IN PARTIAL FULFILLMENT
OF THE REQUIREMENTS FOR THE DEGREE OF
DOCTOR OF PHILOSOPHY

UNIVERSITY OF FLORIDA

2004

Copyright 2004

by

Hongqi Li

This dissertation is dedicated to my family and my advisor with love and gratitude.

ACKNOWLEDGMENTS

First of all, I would like to thank my advisor, Dr. Fereshteh Ebrahimi, for her guidance, encouragement, support, and patience throughout my four years of study. I am also grateful for the learning experience achieved under her supervision, which, I believe, will be of benefit to my future scientific career. I would also like to thank Dr. David Norton, Dr. Darryl Butt, Dr. Michael Kaufman, Dr. Anna Brajter-Toth and Dr. Simon Phillpot for their sincere help and participation on my supervisory committee.

I would also like to thank Dr. Karin Pruessner and Mr. Jerry Bourne for their sincere help in performing HRTEM and Nanoindentation analysis, respectively. I am also thankful to everyone in our group for a pleasant working environment.

My special acknowledgment goes to my wife for her love and mental support. Finally I am at a total loss of words in expressing the depth of my emotion for my parents for their constant support and inspiration.

This work was supported by the National Science Foundation under grant number DMR-9980213.

TABLE OF CONTENTS

	<u>page</u>
ACKNOWLEDGMENTS	iv
LIST OF TABLES	viii
LIST OF FIGURES	ix
ABSTRACT	xiv
CHAPTER	
1 INTRODUCTION	1
2 BACKGROUND	5
2.1 Fabrication of Nanocrystalline Ni-Fe alloys.....	5
2.1.1 Synthesis Methods.....	5
2.1.2 Electrodeposition of Ni-Fe alloys.....	7
2.2 Characterization of Electrodeposited Ni-Fe Alloys.....	10
2.3 Grain Boundary in Nanostructured Metals.....	13
2.4 Mechanical Properties of Nanocrystalline Metals.....	16
2.4.1 Annealing Effect.....	21
2.4.2 Strain-Rate Effect.....	22
2.5 Fracture Behaviors in Nanocrystalline Metals	23
2.6 Deformation Mechanisms.....	25
2.6.1 Computer Simulation.....	28
2.6.2 TEM Observation	33
2.7 Thermal Stability of Nanocrystalline Metals.....	35
3 EXPERIMENTAL PROCEDURES.....	40
3.1 Electrolyte Preparation	40
3.1.1 Ni-Fe Alloys	40
3.1.2 Pure Ni.....	41
3.2 Substrate Preparation.....	42
3.3 Electrodeposition.....	43
3.3.1 Experimental Setup	43
3.3.2 Electrodeposition of Ni-Fe Alloys.....	44
3.3.3 Electrodeposition of Pure Ni	45

3.4	Sample Preparation.....	45
3.4.1	Tensile Test Samples.....	46
3.4.2	TEM Samples.....	46
3.5	Analysis Methods and Experimental Characterizations.....	46
3.5.1	Compositional Analysis.....	46
3.5.2	X-ray Diffraction.....	47
3.5.3	Transmission Electron Microscopy (TEM).....	48
3.5.4	Scanning Electron Microscopy (SEM).....	48
3.5.5	Microhardness Measurement.....	49
3.5.6	Uniaxial Tensile Test.....	50
3.5.7	Nanoindentation.....	50
3.5.8	Heat Treatment.....	51
4	SYNTHESIS AND CHARACTERIZATION OF NI-FE ALLOYS.....	53
4.1	The Effect of Chemical Species.....	53
4.2	Compositional Analysis.....	58
4.2.1	The Effect of Ferrous Ion Concentration.....	58
4.2.2	Compositional Distribution.....	60
4.3	Microstructure.....	65
4.3.1	Grain Size and Lattice Strain.....	65
4.3.2	Texture and Lattice Parameter.....	68
4.3.3	TEM Observations.....	72
4.4	Microhardness.....	76
4.5	Microrcracking.....	80
4.6	Discussion.....	84
4.7	Summary.....	86
5	MECHANICAL PROPERTIES AND FRACTURE BEHAVIOR OF NANOCRYSTALLINE NI-15%FE ALLOY.....	88
5.1	Deformation and Fracture Behavior of the Ni-15%Fe Alloy.....	89
5.1.1	Microstructure.....	89
5.1.2	Tensile Results.....	91
5.1.3	Fracture Behavior.....	98
5.2	Discussion.....	106
5.3	Summary.....	110
6	THE INFLUENCE OF GRAIN SIZE ON MECHANICAL BEHAVIOR.....	112
6.1	Results and Discussion.....	113
6.1.1	Tensile Results.....	114
6.1.2	Fractography.....	119
6.1.3	Nanoindentation Results.....	125
6.2	Summary.....	127

7	THE EFFECT OF LOW TEMPERATURE ANNEALING ON MECHANICAL PROPERTIES	128
	7.1 Experimental Results	128
	7.1.1 Microstructure	128
	7.1.2 Tensile Results.....	131
	7.1.3 Constant Load Rate Indentation	133
	7.2 Discussion.....	135
	7.3 Concluding Remarks	137
8	THERMAL STABILITY AND GRAIN GROWTH KINETICS	138
	8.1 Isochronal Annealing.....	138
	8.1.1 Effect of Temperature on Grain Size.....	138
	8.1.2 Effect of Temperature on Internal Stresses	142
	8.1.3 Microhardness	146
	8.2 Isothermal Annealing.....	147
	8.2.1 Microstructure	147
	8.2.2 Microhardness	152
	8.3 Analysis	153
	8.4 Summary.....	159
9	CONCLUSIONS	160
	LIST OF REFERENCES	164
	BIOGRAPHICAL SKETCH	175

LIST OF TABLES

<u>Table</u>	<u>page</u>
4-1 The deposition parameters and properties for four designed baths.....	55
4-2 Electrodeposition parameters and properties of various Ni-Fe alloys.	59
4-3 The texture of electrodeposited nickel-iron alloys.....	70
4-4 The calculated internal stresses and predicted tensile strength of deposits.....	83
5-1 Tensile properties of as-deposited Ni-15%Fe alloys.....	92
6-1 Tensile results for Ni, Ni-6%Fe and Ni-15%Fe alloys.	116
7-1 A summary of the tensile results.	133
8-1 The texture of two Ni-Fe alloys annealed at different temperatures.	140
8-2 Texture as a function of time at two annealing temperatures.....	151

LIST OF FIGURES

<u>Figure</u>	<u>page</u>
2-1 Fe content as a function of Ni/Fe ion ratio in the electrolytes.	9
2-2 The influence of current density and electrolyte agitation on Ni-Fe electrodeposits' compositions.....	9
2-3 The variation of grain size with the Fe content in Ni-Fe deposits.	11
2-4 Microcracking on the surface of electrodeposited Ni-87%Fe alloy.....	12
2-5 HRTEM pictures of grain boundary of (a) electrodeposited Ni and (b) vapor deposited Pd.	15
2-6 Yield strength of nanocrystalline copper as a function of grain size.	17
2-7 Variation of strength with grain size for metals.....	19
2-8 Relationship between tensile elongation and grain size.....	20
2-9 Fracture surface of (a) electrodeposited Ni-W alloy with a grain size of approximately 8 nm and (b) conventional 4150 steel.	25
2-10 Microcrack propagation in nanocrystalline Ni by atomistic simulation under mode I tension.....	26
2-11 Computer simulation schemes atomic activities at grain boundary of grains 1 and 14 after being loaded.	29
2-12 Deformation mode at different grain sizes in copper. (a) The structure after 10% deformation, $d = 49$ nm; (b) shows the same for a system with $d = 7$ nm.....	31
2-13 TEM images show microstructures of electrodeposited Ni. (a) as-deposited; (b) abnormal grain growth at 493 K for 480 min; (c) normal growth at 603 K for 20 min.....	37
3-1 Experimental setup of (a) real and (b) schematic pictures.	43
3-2 The change in the current density with the applied potential.....	44
3-3 Vickers indentation marks on (a) unpolished and (b) polished surfaces.....	49

4-1	The effect of anion type on the dependency of the iron content of the Ni-Fe alloys on the Fe^{2+} concentration of the bath.....	54
4-2	SEM surface morphology of the Ni-15%Fe alloy deposited from different iron sources. (a) FeSO_4 and (b) FeCl_2 at low magnification; (c) FeSO_4 and (d) FeCl_2 at high magnifications.	56
4-3	Optical micrograph of the surface of the Ni-60%Fe deposits fabricated using (a) FeSO_4 and (b) FeCl_2	57
4-4	The iron content of deposited Ni-Fe alloys as a function of the Ni/Fe ion ratios. ...	58
4-5	Microprobe analysis results for the L20 sample..	62
4-6	Microprobe analysis results for the L13 sample..	63
4-7	The potential versus the deposition time, where the dotted line represents the average value.....	64
4-8	The effect of iron content on the grain size of electrodeposited Ni-Fe alloys	66
4-9	The lattice strain as a function of the iron content in the electrodeposited Ni-Fe alloys.	67
4-10	XRD diffraction patterns of (a) Ni-69%Fe alloy showing the duplex structure and (b) Ni-60%Fe alloy exhibiting single FCC phase.	69
4-11	Lattice parameter as a function of iron content in deposited Ni-Fe alloys.....	71
4-12	TEM images showing (a) bright filed and (b) corresponding selected area diffraction pattern and (c) dark filed for L07 deposit.....	73
4-13	TEM micrographs showing (a) bright filed and (b) corresponding selected area diffraction pattern and (c) dark filed for L13 deposit.....	74
4-14	The grain size distribution based on the grain number.	75
4-15	Flow stress as a function of grain size; (a) iron content from 4-7% and (b) deposits have a iron range of 51 to 60%.	77
4-16	Flow stress as a function of iron content.....	78
4-17	Microcracking pattern in different Ni-Fe alloys.....	81
4-18	The potential versus the deposition time for pure nickel.	84
5-1	TEM images of (a) bright filed, (b) dark field and (c) selected area diffraction pattern; (d) grain size distribution, inset number is the average grain size.	89

5-2	High resolution TEM picture of as-deposited Ni-15%Fe sample.	90
5-3	HRTEM pictures of (a) two adjacent grains and (b) four dislocations (red marks) sitting at grain boundary between grains 1 and 2.	90
5-4	Engineering stress-strain curves of as-deposited Ni-15%Fe alloys	91
5-5	Defects on the fracture surfaces of (a) #3, (b) and (c) #1 samples.	95
5-6	High resolution TEM micrograph of a deformed sample; (a) a 17 nm grain in the center; (b) amplified image of square region in (a) indicating the existence of a dislocation (red line).	95
5-7	Engineering stress-strain curves of partially loaded Ni-15%Fe specimens.	97
5-8	True stress-strain and strain hardening rate-strain curves.	97
5-9	Fracture geometries. (a) fracture scenario of all four specimens; (b) shear lip in sample #4; (c) and (d) magnified images of circled regions 1 and 2 in (b), respectively.	98
5-10	SEM photographs of the fracture surfaces. (a) and (b) taken from the mid-section and slanted regions, respectively; (c) shows a change from non-necked to necked portion.	99
5-11	SEM images of the fracture surface showing (a) the middle section and (b) the slanted portion at high magnifications.	100
5-12	TEM micrographs of (a) dark field and (b) bright field, showing the intergranular fracture.	101
5-13	SEM observations of (a) middle section and (b) slant area.	102
5-14	Notable plastic zones ahead of microcracks in (a) as-deposited and (b) annealed samples; (c) microcracking and deformation bands.	103
5-15	Connecting between two adjacent microcracks on the (a) substrate side and (b) the solution side; (c) and (d) the steps on the fracture surfaces.	105
5-16	Schematic diagram describing the fracture procedures in defect-free nanocrystalline metals.	107
5-17	Microcrack nucleation at the defects.	109
6-1	Grain size distributions.	114
6-2	Tensile stress-strain curves of Ni, Ni-6%Fe and Ni-15%Fe alloys.	116
6-3	Tensile elongation in FCC metals as a function of the grain size.	118

6-4	TEM micrograph of a deformed nickel sample.	118
6-5	Fracture surfaces of pure nickel at (a) low and (b) high magnifications.	120
6-6	SEM micrographs showing (a) deep dimples and (b) knife-edge behavior on the fracture surface of the Ni-6%Fe samples.	120
6-7	TEM dark field image of pure nickel shows the mixture of intergranular and intragranular fractures.	121
6-8	SEM images show the deformation bands in (a) pure nickel and (c) Ni-6%Fe alloy as well as the necking geometries of (b) pure nickel and (d) Ni-6%Fe alloy, respectively.	123
6-9	Stress-strain curves of Ni-6%Fe and Ni-15%Fe alloys with and without defects.	124
6-10	Fracture surface of one Ni-6%Fe sample with a defect.	124
6-11	Load-displacement (<i>P-h</i>) curves of (a) pure nickel and (b) Ni-15%Fe alloy at two different load rates. Each curve is an average of five indents at given load rate.	125
7-1	TEM bright field micrographs of (a) as-deposited and (b) annealed Ni-15%Fe specimens.	129
7-2	TEM dark field images of (a) as-deposited and (b) annealed Ni-15%Fe specimens. Insets denote the selected area diffraction patterns.	130
7-3	Grain size distribution of (a) as-deposited and (b) annealed samples.	131
7-4	Tensile stress-strain curves of as-deposited and annealed Ni-15%Fe samples.	132
7-5	Load-displacement (<i>P-h</i>) curves for (a) as-deposited and (b) annealed Ni-15%Fe samples.	134
7-6	High resolution TEM image of electrodeposited Ni-Fe samples shows no evidence of second phase at the grain boundary.	135
8-1	Variation of grain size as a function of annealing temperature for electrodeposited Ni and Ni-Fe alloys.	139
8-2	TEM micrographs of Ni-15%Fe alloy. (a) as-deposited; (b) annealed at 523 K and (c) annealed at 673 K.	142
8-3	Change of the lattice strain with (a) annealing temperature and (a) grain size.	144
8-4	The profile of (111) XRD peak at different annealing temperatures in cases of (a) Ni-21%Fe and (b) Ni-15%Fe samples.	146

8-5	Variation of hardness with the annealing temperatures.	147
8-6	The grain size as a function of annealing time for nanocrystalline Ni-15%Fe deposits at 523 K and 673 K.	148
8-7	The lattice strain versus the annealing time for nanocrystalline Ni-15%Fe deposits at 523 K and 673 K.	149
8-8	TEM bright field images of nanocrystalline Ni-15%Fe specimens annealed at 523 K. (a) as-deposited; (b) 90 min; (c) 3210 min and (d) 7490 min.	150
8-9	The profile of XRD (111) peak as a function of annealing time at (a) 523 K and (b) 673 K.	152
8-10	Microhardness as a function of the grain size in case of Ni-15%Fe and Ni-21% Fe alloys.	153
8-11	Plot of $\ln(D(t)-D_0)$ as a function of $\ln(t)$ for the Ni-15%Fe alloy isothermally annealed at 523 K and 673 K, respectively.	155
8-12	The Arrhenius curves for the grain growth in electrodeposited (a) Ni-15%Fe and (b) Ni-21%Fe alloys.	156

Abstract of Dissertation Presented to the Graduate School
of the University of Florida in Partial Fulfillment of the
Requirements for the Degree of Doctor of Philosophy

FABRICATION, THERMAL STABILITY AND MECHANICAL
CHARACTERIZATION OF ELECTRODEPOSITED
NANOCRYSTALLINE FACE CENTERED CUBIC NI-FE ALLOYS

By

Hongqi Li

May 2004

Chair: Fereshteh Ebrahimi

Major Department: Materials Science and Engineering

Various compositions of FCC (face centered cubic) Ni-Fe alloys with a grain size of less than 15 nm were successfully fabricated using the electrodeposition technique. It was found that the grain size, lattice strain, texture, lattice parameter, microhardness as well as the microcracking pattern are all dependent on the iron content of deposits.

Tensile results showed that defect-free nanocrystalline FCC metals are not inherently brittle and exhibit a good combination of super-high strength and a reasonable tensile elongation. Due to the high quality of samples, the tensile ductility obtained in the current study is a noticeable improvement in comparison to the previously reported results. In the case of the Ni-15%Fe alloy with a grain size of below 9 nm, the approximately 6% plastic tensile elongation is the first time to be reported in FCC metals at such grain size level. Based on the fractographic analysis, a model describing the fracture process in nanocrystalline metals was proposed. It was found that the stable propagation of the microcracks preceded the final fracture.

Low temperature annealing had considerable effect on the mechanical behavior of nanocrystalline Ni-Fe alloys and resulted in an increase in the strength and a reduction in the ductility, which is probably due to the grain boundary relaxation. In addition, the as-deposited samples exhibited loading-rate sensitivity and the annealed samples showed otherwise. These findings suggest that the grain boundary does play a significant role in the deformation process for nanocrystalline materials.

Isochronal and isothermal annealings were applied to study the thermal stability and the grain growth kinetics in nanocrystalline metals. A stabilization of nanocrystalline structure was found by the addition of iron to nickel. It is also of interest that two temperature regimes were identified in terms of the grain growth. Based on the calculation of the activation energy, it is suggested that the grain boundary diffusion dominates at low temperatures, whereas the lattice diffusion starts to make a contribution to the grain growth within the high temperature range. An abnormal grain growth was observed and the grain growth can still be described by the generalized parabolic grain growth model.

In conclusion, this dissertation elucidates that the addition of alloying element, grain size and the grain boundary state are three key parameters to be considered when studying the nanostructured materials.

CHAPTER 1 INTRODUCTION

Nanostructured materials were firstly introduced by Gleiter [1], and Grandqvist and Buhrman [2]. In general, nano materials are referred to those having an average grain size less than 100 nm. Because their small grain size is down to nanoscale – 10^{-9} meter level, approximately one thousandth of a typical human hair's diameter, nanocrystalline materials exhibit a wide variety of fascinating mechanical [3-5] and magnetic [6,7] properties, which cannot be achieved in coarse-grained materials. As a result, nanostructured materials have the potential of revolutionizing traditional materials design in many areas. For example, nanostructured materials can meet the recent need for miniaturization of magnetic recording devices and electromagnetic MEMS (microelectromechanical systems) devices [7,8]. In addition, nanostructured materials have also shown potential structural applications due to their ultra-high strength [3,5,9-13] and superior wear resistance [14]. In the past two decades, therefore, nanocrystalline materials have been attracting rapidly increasing attention [3-30].

It has been widely accepted that the nanocrystalline materials have high strength [3,5]. However, there is disagreement about ductility. Due to the limitation in obtaining fully-dense bulk nanocrystalline materials, the reported results on mechanical properties are mainly obtained using compression method [5,31], and the tensile results are relatively limited. Moreover, it is noteworthy that the experimental results to some extent were affected by the processing imperfections [10,31]. In spite of an expansion of research in the past twenty years on nanostructured metallic materials, the reasons for low

ductility observed in nanostructured materials are not understood. Some foretell that, based on the reported tensile and computational results, the nanocrystalline materials are inherently brittle [32]; others think the tensile results may in part be artificial [10,33].

The fracture characters may provide some clues to ductility. Basically, stable propagation and intragranular fracture are characteristic of ductile manner, and brittle fracture is represented by intergranular and unstable behaviors. However, with respect to knowledge of fracture behaviors in nanocrystalline materials, little is known. There are very limited published results on how the fracture develops, especially in bulk nanocrystalline materials with a grain size less than 20 nm.

In conventional polycrystalline materials, usually there are many numbers of lattice defects such as dislocation. Plastic deformation in coarse-grained metals is carried by the motion of dislocations [34]. The relationships between microstructures and mechanical behaviors have also been well developed based on dislocation mechanisms. When the grain size is reduced within the nano-regime, computer simulation shows that the dislocation activity within grains may become difficult and even cease [23,35-39]. In other words, the dislocation-based theories with regard to property-structure relationships, deformation and fracture mechanisms established in conventional materials may no longer hold in nanostructured materials. Thus, the most interesting point in the development of nanocrystalline materials is to characterize how the unique properties obtained in nanostructured materials change with structures when the grain size is at nanometer scale. In the aspect of theoretical understanding, most if not all works have been conducted by computer simulation, which is a valuable tool in scientific research, specially at the atomic level. The results demonstrate that grain boundary sliding

mechanism operates in nanocrystalline materials, in particular when grain size is less than 20 nm [35-40]. The studies in terms of the role of grain boundaries in mechanical responses will be beneficial for evaluating the grain boundary sliding mechanism proposed by computer simulations, whereas the supporting experimental evidences are limited and more information is required. In addition, computer simulation results illustrate a transition in deformation mechanism to attempt to understand the “inverse” Hall-Petch phenomenon observed experimentally [41,42]. It is reasonable to think that the tensile behaviors should be different beyond and below this transition point. The obtained deformation and fracture manners in turn are critical to support and understand the deformation mechanism predicted at atomic scale.

There is a large fraction of atoms sitting at the grain boundaries in nanomaterials and these atoms are in a non-equilibrium state. Unfortunately, up to now, thermal stability and growth kinetics are not well understood and established in nanocrystalline materials [43-45]. Low temperature annealing will result in grain boundary relaxation without grain growth [45]. At the high temperature, however, the grain growth will occur toward an equilibrium state with increasing temperature. Thus, the grain size dependent properties of nanostructured materials will be affected by heat treatments. As a result, a better understanding of growth kinetics will render us more information regarding nanocrystalline materials and the study of grain growth mechanism will provide valuable guides for future applications of nanocrystalline materials.

In this dissertation, the endeavor was firstly devoted to fabricate the dense nanocrystalline metallic materials with low impurity level and few defects using electrodeposition technique. The different microstructures were realized by controlling

the electrodeposition parameters. Experimental characterizations using tensile tests, TEM (transmission electron microscopy), SEM (scanning electron microscopy) and other techniques were performed to characterize the microstructures at nano-level. The dependence of the deformation and fracture behaviors on the grain size were also evaluated. Finally, via isothermal and isochronal heat treatment, the thermal stability and growth kinetics were investigated. A comprehensive analysis of the experimental results was conducted to aid in understanding the nanomaterials.

CHAPTER 2 BACKGROUND

Amongst utilizable materials in industry, FCC Ni-Fe alloys, also known as the soft magnetic materials, exhibit a spectrum of physical properties that have to widespread applications in high technology [46-48]. For example, one important application involves Permalloy (a binary Ni-Fe alloy usually with a approximate composition of ~20 wt.% Fe), which has been found in the thin-film head of a computer's hard disk drive and in the electromagnetic MEMS (microelectromechanical systems) devices [46,47]. However, recent requirements for recording heads to write on the high-coercivity media at high frequencies have not been met by the conventional Ni-Fe alloys. Nanocrystalline Ni-Fe alloys have been extensively investigated and become a potential candidate for recent technology requirements due to their improved strength, increased wear resistance and good soft magnetic properties [9,49-53]. As a result, nanostructured Ni-Fe alloys were chosen to be studied in the present dissertation.

This chapter is intended to provide knowledge concerning the fabrication of FCC nanocrystalline Ni-Fe alloys. Documented results regarding the fabrication-structure-mechanical properties, deformation mechanism, fracture behaviors, and thermal stability for nanocrystalline FCC metallic materials will also be reviewed.

2.1 Fabrication of Nanocrystalline Ni-Fe alloys

2.1.1 Synthesis Methods

In order to perform experimental studies on nanocrystalline materials, the first challenge is to achieve a fully-dense bulk material. To date, different laboratory-scale

processing techniques have been developed to synthesize the nanostructured metallic materials (pure metals and alloys). Examples of the processing techniques are inert gas condensation of particulates (IGC) [4,54,55], ball milling and compaction (BM) [15,56-60], sol-gel (SG) technique [61], sputtering [62,63], severe plastic deformation (SPD) [64], and electrodeposition [3,10,16,17,65,66]. The former five methods have major disadvantages. In the case of gas condensation, the shortcomings are small sample amounts, large sample porosity and high cost. For the ball milling, the contamination of powders during the mechanical processing is actually not avoidable, resulting in a high impurity level in samples. Large amount of lattice disorder is also developed during the milling process. Similar to the IGC method, the main deficiency of the sputtering and sol-gel techniques is the large sample porosity in specimens. In a word, the samples fabricated by these four techniques are not fully dense, i.e., the nanocrystalline materials produced by ball milling, gas-condensation, sputtering and sol-gel technique are highly defective. These kinds of disadvantages can be diminished using SPD technique. In this case, the purity in the finished samples only depends on the starting material. However, inside samples, there are many dislocations generated during the severe deformation. Additionally, this type of processing technique has the characteristics of cold-worked materials, where the plastic deformation has been primarily exhausted. It is also worth mentioning that the grain size obtained from this technique still remains at a level of more than 100 nm.

As early as 1932, Dehlinger and Geisen reported the electrochemical synthesis of brass [67]. Since then, particularly in the past two decades, the electrodeposition technique consisting of direct and pulsed current methods has been widely used to

manufacture the metallic materials. This technique has proven to be a simple, versatile, and inexpensive way to make nanomaterials. One of the advantages of electrodeposition is that it is capable of fabricating a fully-dense metal with a relatively narrow grain size distribution. In recent years, both pure metals (Ni [3,10], Cu [68], Pd [69], Co [70]) and binary alloys such as Ni-Cu [66], Ni-Fe [17,65], Ni-W [18,71] have been successfully produced via electrodeposition. Another virtue of electrodeposition is the easy control of grain size and thickness by varying parameters such as current density, agitation, electrolyte solution, and deposition time. For example, an addition of W into Ni allows to be produced a grain size less than 20 nm [18]. In addition, recent studies with the use of electron microscopy and positron lifetime spectroscopy indicated that the electrodeposited samples were denser than those made by IGC and high-pressure torsion (HPT) [72]. As a result, the electrodeposition technique will be employed to fabricate the nanocrystalline Ni and Ni-Fe alloys in the current study.

2.1.2 Electrodeposition of Ni-Fe alloys

The essence of electrodeposition is that, during the electrodeposition process, the current is applied to pass through an electrolyte and then the reduction action takes place at the cathode surface. In the case of plating Ni-Fe alloys, the anodic ions such as Fe^{2+} and Ni^{2+} are reduced into Fe and Ni elements, respectively. In this process, part of the applied current may be consumed by hydrogen evolution. In fact, Fe is only electrodeposited from its ferrous ions and the excess of ferric ions is detrimental. It also has been well recognized that Ni-Fe plating is an “anomalous” co-deposition condition. That is, according to the single element deposition rates, the rate of depositing Ni is expected to be faster than that of reducing Fe. However, the fact is that the deposition rate for Fe is much larger than that for Ni during simultaneous electrodeposition of Ni and Fe

[73]. This is ascribed to the inhibition of the Ni reduction process due to the presence of the Fe ion [74-77].

It is summarized from the literature that the basic contents of the electrolyte for depositing Ni-Fe alloys consist of Ni sulfate/chloride, ferrous sulfate/ferrous chloride, and boric acid. In the actual electrodeposition, other chemicals such as ascorbic acid and sodium dodecyl sulfate ($\text{CH}_3(\text{CH}_2)_{11}\text{OSO}_3\text{Na}$) were also added. In general, the results show that the Fe content in electrodeposits was primarily dependent on the ratio of Ni/Fe ions in the solution [78,79]. Figure 2-1 presents the change of the Fe content in deposits with the ratio of $\text{Ni}^{2+}/\text{Fe}^{2+}$ in the electroplating bath [17,80]. It can be seen that the Fe content decreases rapidly with decreasing Fe ion concentration. In addition, the current density and the degree of agitation are also important and can be used to control the compositions of the deposits. Figure 2-2 displays the variation of the Fe concentration with the current density and agitation for the specific baths [81]. The $\text{Ni}^{2+}/\text{Fe}^{2+}$ ratios in these two cases were 5:1 and 25:1, respectively. The results indicate that the milder the agitation, the lower the percentage of Fe in the deposits, as well as that the Fe content decreased with increasing the current density. Once again, it is apparent that the Fe content in the deposited Ni-Fe alloys strongly depends on the $\text{Ni}^{2+}/\text{Fe}^{2+}$ ratio.

A comparison between baths 5:1 and 25:1 reveals that the sensitivity of the deposit composition to the current density and the degree of agitation increased with increasing the ratio of $\text{Ni}^{2+}/\text{Fe}^{2+}$ in the bath. In terms of the deposition mechanism, the dependence of the Fe content on the current density and rotation speed is related to the plating efficiency. It has been found that the plating efficiency is not significantly sensitive to the bath species; it is high, as was typically observed [77,82]. For any given plating bath, it

appears that the plating efficiency decreased with an increase in the degree of agitation and increased as the current density was increased. Referring to Figures 2-2, it could be concluded that the plating efficiency decides the Fe concentration in the deposits in such a way: the Fe content increases when the plating efficiency decreases.

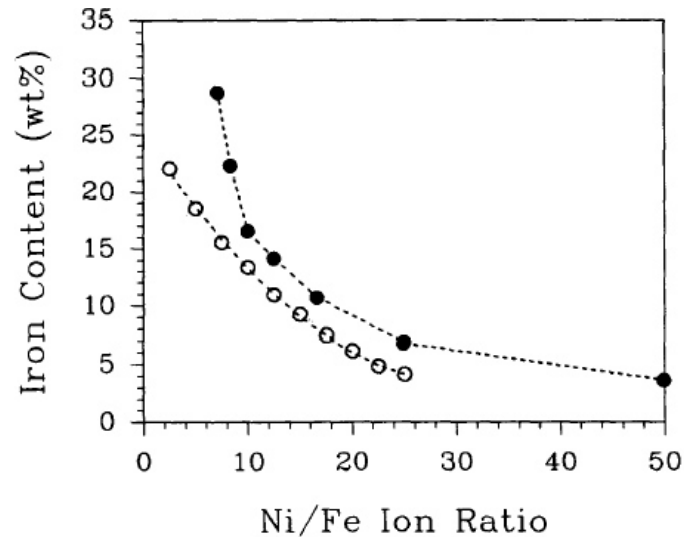


Figure 2-1. Fe content as a function of Ni/Fe ion ratio in the electrolytes [17,80].

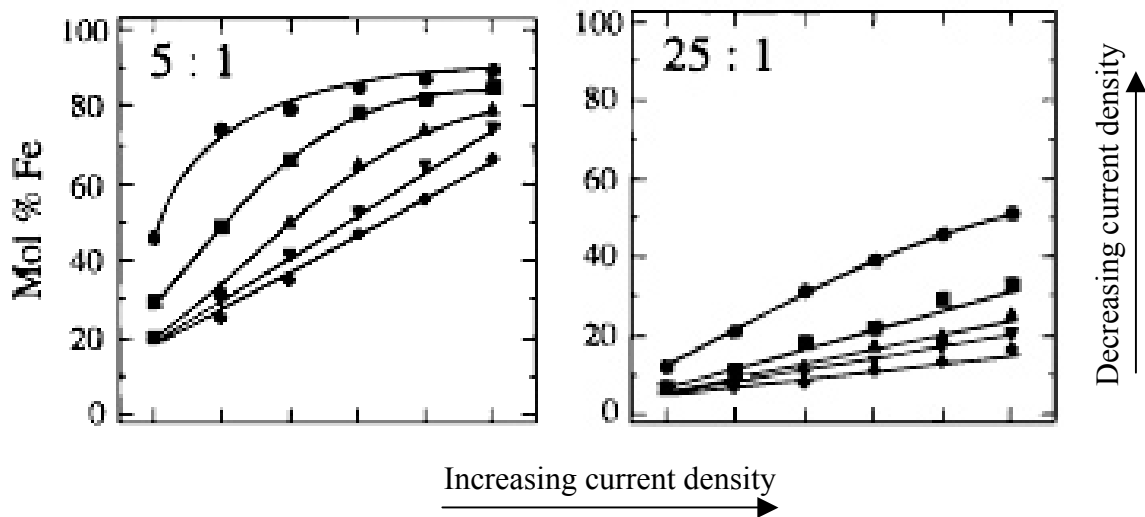


Figure 2-2. The influence of current density and electrolyte agitation on Ni-Fe electrodeposits' compositions [81].

In addition to these decisive parameters, the pH, boric acid and additives also play a role. Commonly, the solution used to plate the Ni-Fe alloys contains boric acid. Consequently, it is of importance to make clear what the boric acid's acting role is in the electrodeposition. Kieling [83] reported that boric acid had a function of preventing the formation of hydroxide films and its presence led to the reduced Fe content in deposits. However, another research group [76] reported that the boric acid acts as a surface agent and functions as a selective membrane which permits the Fe reduction but blocks the passage of the Ni reduction. The pH value of the bath has no apparent effect on the composition of the alloy, but a higher pH than 3.6 generally results in unaccepted samples with high residual stress [80].

In summary, by changing the deposition parameters, the fully-dense nanocrystalline Ni-Fe alloys with a wide range of concentrations and different microstructures can be achieved, which makes it possible to carry out investigations to understand the inherent rules operative in the nanostructured materials.

2.2 Characterization of Electrodeposited Ni-Fe Alloys

It has been reported that the microstructures of the deposits, such as phase and grain size, were dependent on the Fe content in the electrodeposited Ni-Fe alloys [17,84]. For instance, there was a transition from FCC (face centered cubic) phase to BCC (body centered cubic) phase within the Fe concentration range of 60 to 70 wt% (weight percent) [84]. Throughout the whole text, if not specifically mentioned, the composition percent is referred to as the weight percent. The lattice constant is another characteristic parameter of the microstructure. Grimmett *et al.* [84] compared the lattice parameters of the electrodeposited Ni-Fe alloys with those for the thermally prepared FCC Ni-Fe alloys [85] and the results indicated a good match between the two series of data. The linear

change in the lattice parameter with the Fe content points to the fact that the Ni-Fe electrodeposits are true alloys. Figure 2-3 shows the variation of the grain size as a function of the Fe content in the Ni-Fe deposits [84]. Within the FCC range the grain size decreased gradually when increasing the Fe content, suggesting that an addition of alloying element can miniaturize grains. The grain size reached a minimum value at the composition of the BCC and FCC mixed phase. However, beyond this regime, the grain size increased with a further increase in the Fe content. Due to the change in the grain size with the Fe content, it is consequently difficult to study the relationships between the mechanical behaviors and the Fe concentration at one given grain size level. Further efforts need to be devoted to develop the Ni-Fe alloys with the different compositions but the same grain size.

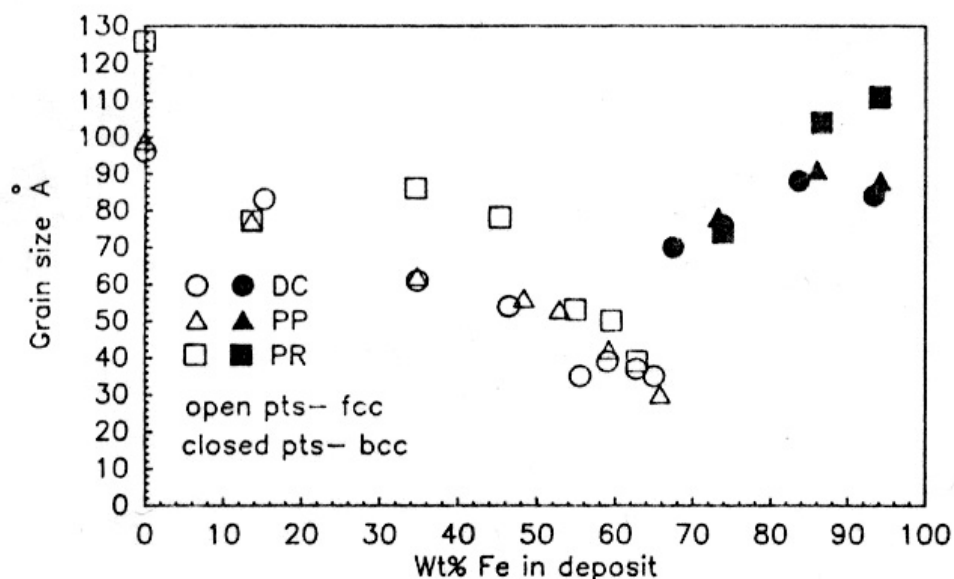


Figure 2-3. The variation of grain size with the Fe content in Ni-Fe deposits [84].

The electrodeposition process is an atom by atom accumulation. Due to the linking of adjacent grains and other interrelated variables involved in the plating process, there usually exist residual stresses, also called internal stresses, in the electrodeposits. The theories developed to explain the origins of the residual stresses are ordinarily classified

as [86] 1) the crystallite-joining; 2) hydrogen theory; 3) effect of substrates and 4) lattice defect theory. Considering the electrodeposited Ni-Fe alloys, at a given deposition condition, the internal stresses increased when the Fe content increases [84]. There is also a correlation between the internal stresses and the grain size. In general, they increase with a reduction in the grain size. If the internal stresses are high enough, microcracks will form, which limits the exploitation of deposits. For example, Figure 2-4 is an example of the microcracking happened in the electrodeposited Ni-87%Fe alloy with a grain size of approximately 6 nm [87,88]. One efficient way to reduce the internal stresses is to add various components such as saccharin into the electrolyte. However, the level of the impurities rises largely as a result of the addition of this stress reliever.

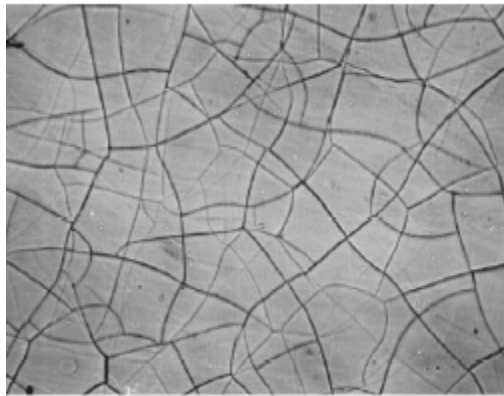


Figure 2-4 Microcracking on the surface of electrodeposited Ni-87%Fe alloy [87].

It is well known that the quality required for the tensile specimens in nanomaterials is extremely high because the mechanical properties have been proven to be affected by the processed flaws. This review on the reported results about the synthesis of the metallic materials is of benefit to guide us in how to make better samples by the use of the electrodeposition technique.

2.3 Grain Boundary in Nanostructured Metals

As a fact, the grain boundary width is not different between nanocrystalline metals and their conventional counterparts. The large volume fraction of the grain boundaries in nanomaterial is associated with its small grain size. For the sake of simplicity, let us assume that the grains are spherical (with a mean grain size of d), and the grain boundary thickness is δ . Then, the volume fraction of the grain boundaries can be calculated as:

$$f_{gb} = \frac{\frac{4}{3}\pi[(d + \delta)/2]^3 - \frac{4}{3}\pi(d/2)^3}{\frac{4}{3}\pi[(d + \delta)/2]^3} = 1 - \left(\frac{d}{d + \delta}\right)^3 \quad (2-1)$$

Previous results have shown that, for the FCC Ni₃Fe alloy, the width of the grain boundary was about 0.5 nm using Mössbauer technique [89]. With the 12 nm and 6 nm crystallites, the volume fraction of atoms at and near the grain boundaries is about 12% and 21% based on the equation (1), respectively. These values are comparable with the reported data by the computer simulations [90,91].

It is because of the higher fraction of the grain boundary volume that many of the physical and mechanical properties of the nanocrystalline materials such as the thermal expansion, elastic constants, fracture stress, ductility and the diffusivity are widely different from those of the same materials with the conventional grain size [92]. In other words, grain boundaries are bound to play a critical role in determining the nanocrystalline materials' properties [1,93]. A computer simulation study on the deformation of nanophase Ni at temperatures up 500 K emphasized the role of the grain boundary type in the deformation process [94,95]. Recent results have shown that, during the deformation in the nanocrystalline metallic materials, the grain boundary is the origin of the dislocation emission and the grain boundary sliding, resulting in the local

plasticity. In addition, the large fraction of the grain boundary atoms is thought to be the cause of thermal instability in nanomaterials. Therefore, it is necessary and important to characterize the grain boundary structure for nanocrystalline materials.

Currently, two controversial results have been issued about the structures of the grain boundaries in nanocrystalline materials. One of them supported by some experiments and computer simulations suggests that the grain boundaries are non-equilibrium, highly disordered, “frozen-gas-like” zones [1,96-99], substantially different from the structures in the coarse-grained polycrystalline materials. The other one argues that the structures of the grain boundaries in the nanocrystalline metals are not anomalous but similar to these found in the conventional polycrystals [100-107].

HRTEM (high resolution TEM) is believed to be an important and powerful experimental technique in the analysis of the grain boundaries in that it can provide direct observations of the grain boundaries. Figure 2-5 illustrates the HRTEM images of the grain boundary structures in the nanocrystalline Ni (~30 nm) [108] and Pd (~6 nm) [100]. Here, Ni was prepared using electrodeposition technique and Pd by physical vapor deposition. It is found that the lattice structure in Ni remains up to the grain boundary, having no second phase and the same characters as in the coarse-grained counterpart, as seen in Figure 2-5(a). However, in Figure 2-5(b), A-B and D-E are ordered and disordered grain boundaries, respectively. “D” denotes a disordered region in the Pd sample. The differences in the grain boundary between Ni and Pd are probably associated with the different synthesis methods. As mentioned in the prior section, electrodeposition can fabricate relatively fully-dense metals. However, the physical vapor deposition method used for making nanocrystalline palladium usually results in porous materials. On

the other hand, it is not clear if it is related to their different grain sizes. Although one recent study on the electrodeposited Ni-W alloy with a grain size of about 4-9 nm demonstrated that the disordered phase was observed in HRTEM, it is still not detected to be prevalent at all grain boundaries. Further work needs to be done on the electrodeposited metals. In addition, it should be careful to correlate the phenomena achieved in HRTEM to the grain boundary nature of the bulk materials due to the thin sample problems. Fortunately, this worry was rooted out by the experimental and theoretical attempts [106,109].

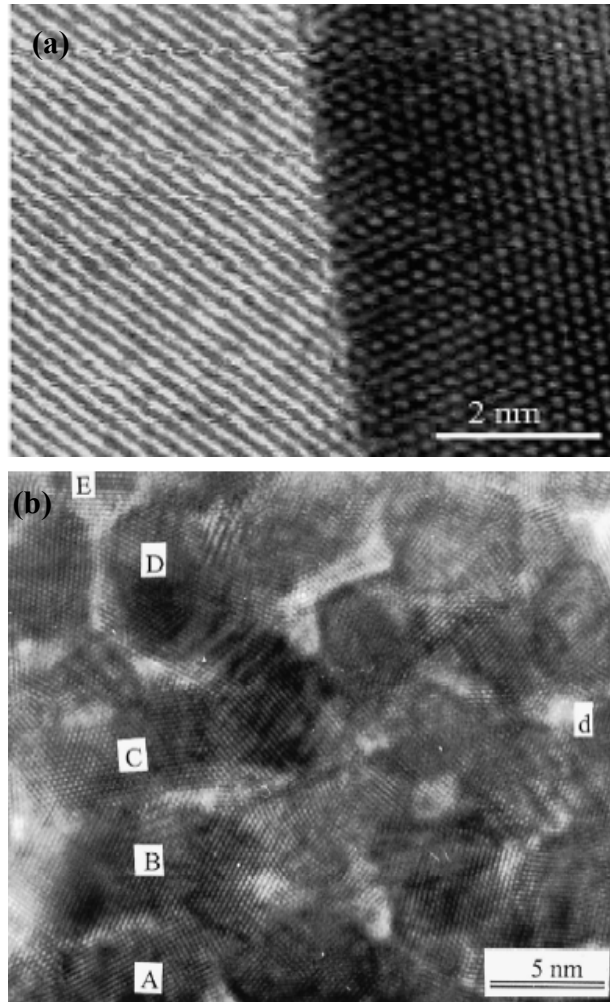


Figure 2-5. HRTEM pictures of grain boundary of (a) electrodeposited Ni [108] and (b) vapor deposited Pd [100].

Besides HRTEM, computer simulation is another useful tool to study the grain boundaries at the atomic level. Recent atomistic simulation results demonstrated that the grain boundary structure in the nanocrystalline FCC materials had the similar features found in conventional materials [37,107]. However, it should be noted that, in the computer simulation, the grain boundary features depend, to some extent, on the methods employed to construct the grain boundaries. A detailed discussion can be found in reference [108].

2.4 Mechanical Properties of Nanocrystalline Metals

Due to the possibility of potential applications of the nanocrystalline materials, it is now becoming more and more attractive to investigate their mechanical properties. Because of the difficulty in fabricating fully-dense, large-scale nanostructured metals, most if not all mechanical characterizations such as the yield strength, fracture strength, and ductility are confined to hardness measurement, compression tests or micro- and nano- indentation. To date, the results coming from the tensile tests are still very limited.

Based on Hall-Petch relationship derived from the dislocation pile-up theory [110,111], it is anticipated that the strength of polycrystals increases with decreasing the grain size. Meaning, the yield strength is proportional to the reciprocal of square root of the grain size as follows:

$$\sigma = \sigma_0 + k.d^{-0.5} \quad (2-2)$$

where σ_0 is the intrinsic friction force required to move individual dislocation, k the constant depending on nature of materials, and d the average grain size. Because of the small grain size, accordingly, nanocrystalline metals have higher (typically 3-10 times) yield strengths relative to their conventional counterparts [3,5,10-13,19-21,112-

117]. For example, electrodeposited nanocrystalline Ni with a grain size of 26 nm had a yield strength as high as 1162 MPa at 0.2% offset of the plastic strain [10]. While, the yield stress of the typical Ni is only 59 MPa. In the case of pure copper, the yield strength for the specimens having a grain size of approximately 20 nm has been measured at 850 MPa [31], which is also more than ten times stronger than the coarse-grained copper strength of about 50 MPa. With more increasing data obtained from the tensile tests, it is interesting to find that there is asymmetry in the strength, in particular at the small grain size regime, between the compressive and the tensile data. Figure 2-6 displays the strength measured from the tensile tests and calculated from hardness values in the IGC nanocrystalline copper [5,31]. It is apparent that the values, acquired from the microhardness and compression tests were in good agreement with those extrapolated from the Hall-Petch behavior of the coarse-grained copper. However, there was an increasing offset in the yield strength relative to the extrapolated values as the grain size was decreased.

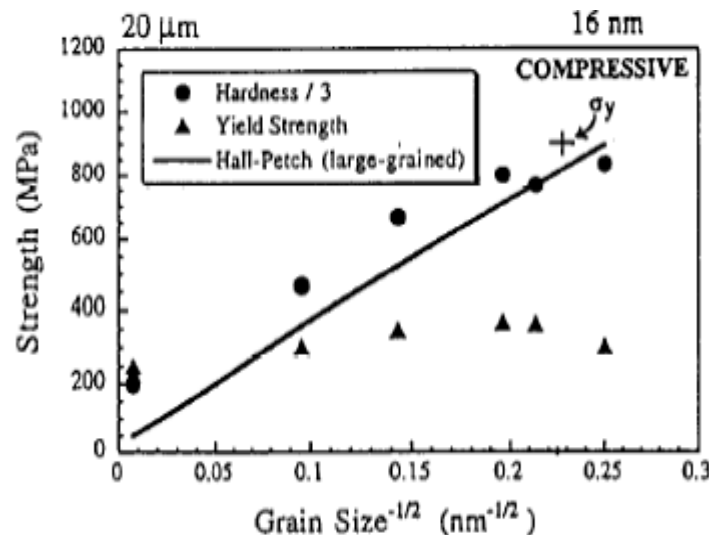


Figure 2-6. Yield strength of nanocrystalline copper as a function of grain size [31].

It has been suggested that this difference is probably attributed to the imperfection of the tested samples [10,31]. As discussed in the fabrication section, there is always

processing porosity in samples prepared by IGC. These defects like the gas-filled pores and flaws have little effect on the hardness measurements, whereas they are extremely detrimental to the tensile tests. Weertman group verified that this shortfall in the yield strength was indeed caused by the presence of the defects by testing the samples with and without flaws [118]. Furthermore, the computer simulations confirm that the porosity in samples did soften the material [40]. Even for the electrodeposited samples with approximately the same grain size, the distribution of the grain size also plays a noticeable role in the mechanical properties [10]. Using 3 and 20 mm tensile specimens, the tensile results for the electrodeposited Ni confirmed that the changes in the mechanical properties observed in different sized samples were related to the inhomogeneous microstructure [11].

Although the Hall-Petch law has been widely accepted to describe how the yield strength rises with decreasing grain size, it is believed there should be a limitation to the application of the Hall-Petch relationship. In the past, due to the restriction in the synthesis technology, the grain size achieved in nanomaterials was usually larger than 20 nm. Recently, with more effort devoted to improve the processing technique, many metals with a grain size less than 20 nm have been successfully constructed via the electrodeposition technique [6,9,16-18,71,119], making it possible to characterize the mechanical behavior at grain sizes below 20 nm. It is a surprise that an “inverse” Hall-Petch relationship was experimentally obtained [6,9,16,119,120] in both hardness and tensile tests. Meaning, when the grain size is reduced below one critical value, the yield strength did not increase any more, but decreased with decreasing grain size. The scheme is displayed in Figure 2-7 [121,122]. For the FCC metals, this critical value is usually

thought to be about 10 to 20 nm, which of course is dependent on the nature of the material. For instance, it is about 12 nm in Permalloy [9,17] and near 10 nm in pure Ni [16] on the basis of the microhardness measurement. Furthermore, it was confirmed that the crossover value of 10 nm for pure Ni was consistent with the theoretical number computed based on the dislocation pile-up mechanism [3]. According to the recent computer simulations, Al [41] and Cu [42] have the critical grain sizes of approximately 18 nm and 14 nm, respectively. The breakdown of the classic Hall-Petch relationship is likely because the conventional dislocation theory no longer holds. That is, the deformation mechanism has changed when the grain size is less than the critical value. This has been substantiated by the computer simulations, which will be discussed in detail in a later section.

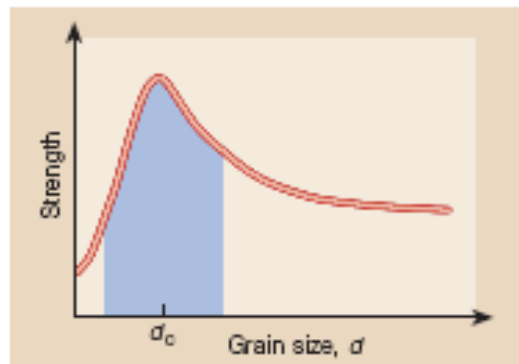
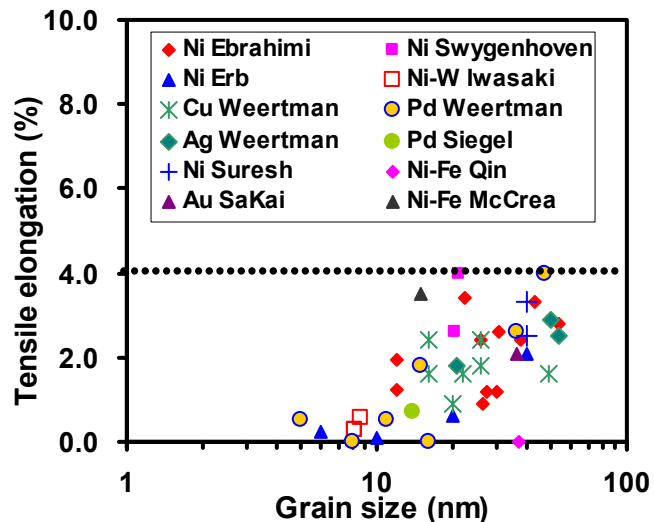


Figure 2-7. Variation of strength with grain size for metals [121,122]. Here, d_c refers to critical grain size.

It is well known that the nanocrystalline metals have the ultra-high strength, rendering them the possibility of potential application in industry. In addition to the strength, when considering the structural utilities, ductility is another important material parameter and defined as the ability of one material to plastically deform without fracture under the external stress. According to the extrapolation from the relationship between

the ductility and the grain size in the conventional metals, the ductility of nanocrystalline materials is expected to be improved [123]. However, the experimental results indicate otherwise. The tensile elongation in nanocrystalline metals was very low, typically less than 4%, at room temperature. For example, the nanostructured Ni and Cu with a grain size of 20-26 nm only exhibited a plastic strain as low as 2% [10,12]; sometimes they even fractured within the elastic regime [12]. Figure 2-8 plots the available tensile results in the FCC metals with a grain size less than 60 nm. Despite the scatter in the data probably due to different fabrication techniques, generally speaking, it is obvious that the tensile ductility decreases with a reduction in the grain size. When grain size approaches 10 nm, tensile elongation is almost zero.



deposited Ni exhibited much higher ductility than DC magnetron sputtered samples and revealed that the latter contain high porosity at the grain boundaries [63]. Others argue that the lack of the dislocation activity in nanomaterials, especially when the grain size is smaller than 20 nm, may be the cause of the low ductility. In addition, plotting the tensile elongation via the strength explicitly indicates that there is a trend of decreasing the ductility with increasing the strength [20,33]. As a result, one may think if the nanocrystalline FCC metals are intrinsically brittle due to their super-high strength. A recent attempt to study the nanostructured Zn has proposed that the decrease in the ductility with a decrease of the average grain size could be an inherent phenomenon in nanocrystalline materials, not determined by the processing artifacts [124]. So far, however, it is still not clear why the ductility is so low when the grain size is less than 20 nm and now the increasing efforts are being devoted to uncover this puzzle.

2.4.1 Annealing Effect

Recently, the temperature dependence of the mechanical behaviors has been evaluated by conducting the tension or compression tests at elevated temperatures [125-127]. It is not surprising that the yield strength decreased for samples tested at the high temperatures or annealed at high temperatures because of significant grain growth.

In order to understand the role of grain boundaries in plastic deformation, low temperature annealing is a better choice because low temperatures just lead to grain boundary relaxation (more equilibrium) but does not change the grain size remarkably. Using the molecular dynamics simulation method, grain boundaries with different degrees of order were created to mimic as-deposited and annealed conditions for pure Ni with a mean grain size of 12 nm; the results showed that the grain boundary relaxation and the increased order of grain boundaries due to annealing resulted in a reduction in the

deformation experienced at a given stress level and an increase in the strength [128]. The hardness results in the case of electrodeposited Ni supports this simulation result. For example, in spite of a slight increase in the grain size from a starting grain size of 19 nm to 26 nm after 20 min annealing at 493 K, the microhardness obviously increased [45]. While the results regarding the electrodeposited Cu having a grain size of approximately 250 nm suggested otherwise [129]. It was found that the tensile elongation went up from 1.6% to 6% after annealing at 423 K for 6 hours [129]. It is possible that the grain size of the as-deposited copper is too large to be considered as a nanocrystalline material (<100 nm), so the grain boundary condition may already be close to the equilibrium state. Or, it could be that the deformation mechanism in deposited copper is the same as in conventional metals. However, tensile experiments of nanostructured FCC metals, with a grain size less than 20 nm, have not been reported.

2.4.2 Strain-Rate Effect

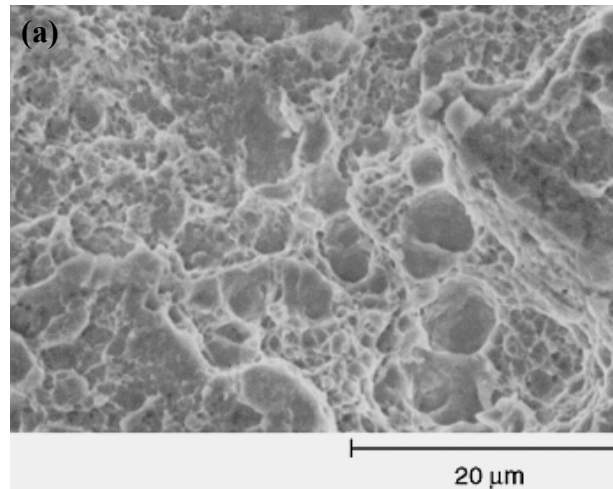
When evaluating the mechanical properties as well as understanding the deformation mechanism, strain rate plays a key role. In general, the tensile stress depends on the strain rate according to the relationship $\sigma = C(\dot{\varepsilon})^m$ at a constant temperature and strain [34]. Here, σ is the tensile stress, C is the constant, $\dot{\varepsilon}$ is the strain rate and m is the strain rate sensitivity. Both compression and tensile tests have shown that nanocrystalline materials display the strong strain-rate sensitivity. For example, a recent compression test conducted on the Ni-19%Fe alloy with a grain size about 37 nm indicates that the yield strength increased as the strain rate was raised at room temperature [114]. In addition, it is interesting that the degree of the strength's dependence on the strain rate at room temperature increased with a decrease in the grain size [130-132]. Nanocrystalline Ni

with a grain size of 40 nm was more sensitive to strain-rate than the ultra-fine Ni. The conventional Ni even exhibited independent plastic flow over the range 3×10^{-4} to $3 \times 10^{-1} \text{ s}^{-1}$ and a simple model based on a strain-rate sensitive grain boundary affected zone was suggested [132]. However, the electrodeposited Ni with a grain size of approximately 20 nm exhibited the opposite observations -- the tensile strength was essentially independent of the strain rate within the range of 5.5×10^{-5} to $5.5 \times 10^{-2} \text{ s}^{-1}$ [11]. This is possibly associated with the difference in the grain size. When the grain size is less than 50 nm, twofold variation in the grain size may result in fundamental changes in the mechanical and deformation behaviors. On the other hand, it is worth pointing out that, within the nano-regime, there is no substantial relationship between the tensile ductility and the strain-rate although little increase in the tensile elongation was observed when the strain-rate was decreased for a 21 nm Ni sample [11]. Reference [108] presents a summary of the experimental results available in literature concerning the strain-rate effect on the yield strength for the FCC nanocrystalline materials. Careful examination discovers that the reported data are all about materials having a grain size larger than 20 nm. Let me remind you that, for FCC materials, the critical value to show the inverse Hall-Petch phenomenon is 10 to 20 nm. Meaning, currently studied samples are all in the “conventional” range. The deformation is still dislocation governed. There are no documented results for metals with a grain size below 20 nm, which is probably due to the unavailability of the required specimens.

2.5 Fracture Behaviors in Nanocrystalline Metals

Figure 2-9 demonstrates the SEM fractographs of the electrodeposited Ni-W samples (~8 nm) fractured in the tension tests at room temperature [18] and the

conventional 4150 steel tested as a Charpy V-notch specimen at 273K [133]. For conventional ductile metals, it has been well established that the dimple pattern (Figure 2-9(a)) obtained on the fracture surface is caused by the microvoid coalescence mechanism, typically a transgranular fracture mode [34,134]. In the case of nanocrystalline metals, as shown above, their ductility is very little, implying a brittle fracture. However, it is surprising and interesting that their fracture surfaces also exhibited a microvoid structure even when the grain size was as low as 8 nm [18], as shown in Figure 2-9(b). The dimple size varying from 20 to 200 nm was about 2 to 25 times the average grain size. Similar observations have been obtained in other nanomaterials such as the electrodeposited Ni (30-40 nm [108,135], ~20 nm [11,117]), laminated Cu/Ag composite (30-70 nm) [30] and the electrodeposited pure copper (~250 nm) [136]. To date, how these microvoids developed in nanocrystalline materials is not known.



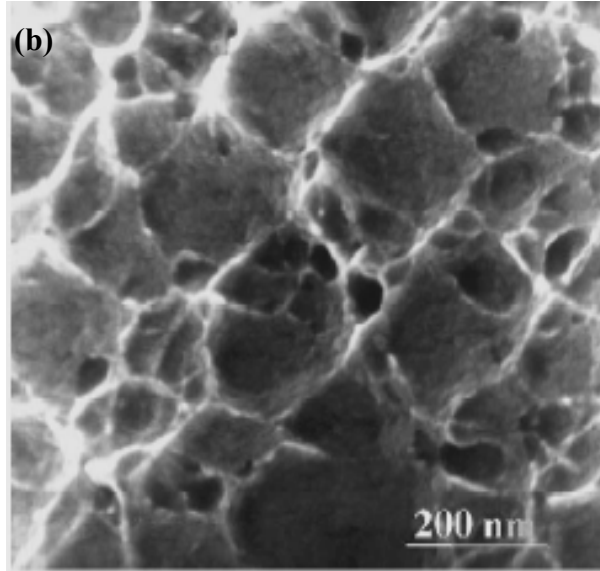


Figure 2-9. Fracture surface of (a) electrodeposited Ni-W alloy with a grain size of approximately 8 nm [18] and (b) conventional 4150 steel [133].

Computer simulation results suggest that local shear planes form around several grains that cannot participate in the grain boundary accommodation process due to their particular misorientation and then fracture occurs along these local planes, resulting in the dimple structures [137]. But no experimental verification is available. Based on TEM *in-situ* observations, Kumar [135] argues that the dimple pattern still originates from the microvoid evolution and the break of ligaments. Besides the microvoid fracture surface, sometimes, nanocrystalline FCC metals fracture in a knife-edge manner typical of a ductile behavior, which has been widely scrutinized in the electrodeposited Ni samples having a grain size of approximately 20 to 50 nm and a thickness of 35 μm [3,10,19]. Consequently, the examined fracture features (ductile manner) significantly disagree with the achieved tensile elongation -- brittle character, this opposition is still puzzling scientists today.

In terms of the fracture manner-intragranular or intergranular in the nanostructured materials, the experimental evidences in the bulk materials are not available. TEM is

another choice. TEM observations of the deformed area from a Vickers indent in the nanocrystalline Ni with a grain size of 28 nm exposed microcracks located at the grain boundaries [12]. However, we should be careful of applying the observed phenomena under TEM into the bulk material because of the thin-film problems.

2.6 Deformation Mechanisms

It has been described in the earlier sections that the mechanical and fracture behaviors in nanocrystalline metals are quite different from those observed in conventional materials, which strongly implying that the deformation mechanism may have changed for nanomaterials. In order to understand why the nanocrystalline materials show unique mechanical properties, it is necessary to take insights into the deformation behaviors at nano-scale. Currently, endeavors have been taken in the theoretical and experimental aspects.

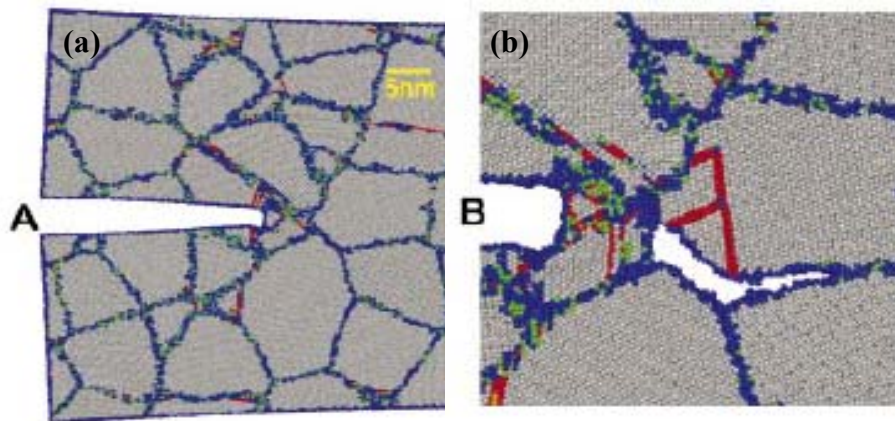


Figure 2-10. Microcrack propagation in nanocrystalline Ni by atomistic simulation under mode I tension [138].

Figure 2-10 presents the crack propagation behaviors in nanocrystalline Ni with a grain size 10 nm by using atomistic simulation method [138]. Initially, a pre-existing crack 'A' was introduced and the crack tip is located within a grain as shown in Figure 2-

10(a). After applying further load, the crack tip emitted a number of dislocations and then blunted 'B'. At the same time, the nanovoids nucleated at the grain boundaries ahead of the crack tip seen in Figure 2-10(b). Later, these nanovoids joined the main crack. Repeated such processes resulted in a intergranular fracture. Furthermore, the results indicate that for all grain sizes from 5 to 12 nm, pure intergranular fracture was observed [138]. In the electrodeposited Ni (30-40 nm), a mixture of intergranular and transgranular fracture paths was seen in TEM [135]. The difference is probably due to either the grain sizes or the applied study methods. In order to make clear what kind of fracture model should be utilized in nanocrystalline materials, more experimental studies are necessary. The importance of investigating the fracture behaviors lies in that, in some senses, it can provide proof that nanocrystalline materials are brittle or ductile. In general, the stable crack propagation represents the ductile manner, otherwise it is brittle. Despite such need, unfortunately, very few published results are currently available, regarding the crack propagation in bulk nanocrystalline FCC metals under the tensile condition.

2.6 Deformation Mechanisms

It has been described in the earlier sections that the mechanical and fracture behaviors in nanocrystalline metals are quite different from those observed in conventional materials, which strongly implies that the deformation mechanism may have changed for nanomaterials. In order to understand why nanocrystalline materials show unique mechanical properties, it is necessary to have insight into the deformation behaviors at nano-scale. Currently, endeavors have been taken in the theoretical and experimental aspects.

2.6.1 Computer Simulation

As the “inverse” Hall-Petch phenomenon was first found in nanocrystalline copper and palladium [139], it has driven scientists to study the deformation mechanism operative in the nanomaterials. It is well known that the classical Hall-Petch law is based on the dislocation theory, so its breakdown means that the conventional dislocation slip mechanism could cease to be operational when the grain size is small enough. Because it is difficult to observe deformation directly in nanocrystalline materials, studies have turned to computer simulations. Tensile results for pure copper with a grain size range of 3 to 7 nm illustrate that, in such materials, most of the plastic deformation is due to a large number of small sliding events on the atomic planes at the grain boundaries – grain boundary sliding [35,40]. Apart from the tensile method, another approach has also been taken to simulate the deformation behavior, where the atom activities are recorded at a constant load, i.e. creep test. Considerable work has been carried out on nanocrystalline Ni [36-39]. The results not only confirm that grain boundary sliding is the main deformation mechanism, but also show that two distinguished atomic processes (atomic shuffling and stress-assisted free-volume migration) were involved during the sliding in the interface [36]. Figure 2-11 presents the detailed atomic activities occurred at the grain boundary between grain 1 and grain 14 in pure Ni (12 nm) [36]. When load was applied, the atoms occupying regions 1 and 2 slid away from grain 14, resulting in an excess free volume locally. After that, two atoms belonging to grain 1 moved toward region 2, transferring the free volume. Then it was observed that an atom of region 4 refilled the vacancy left in region 3, indicating that the atomic shuffling took place.

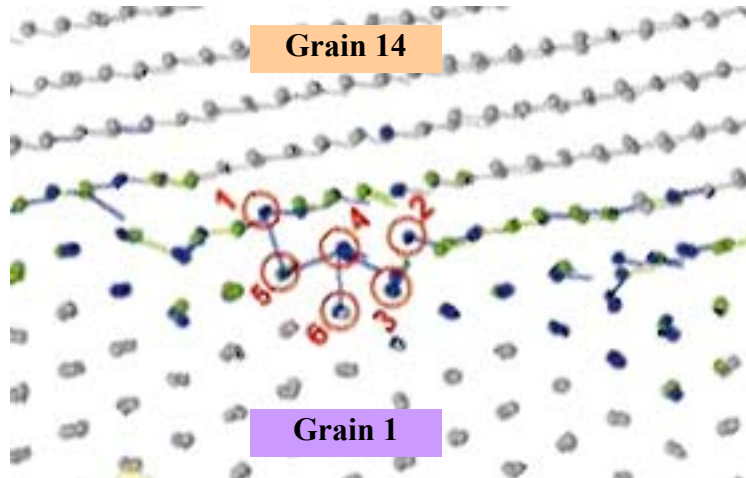


Figure 2-11. Computer simulation schemes atomic activities at grain boundary of grains 1 and 14 after being loaded [36].

Additionally, the result concerning pure Ni demonstrates that the degree of the intergrain sliding depended on the grain size [37,38]. When the grain size was about 3 nm, the plastic deformation was completely controlled by the grain boundary sliding; while, in crystals with a grain size of about 12 nm, the competing mechanism between intergrain and dislocation emission from the grain boundary was observed [38]. Further study on Al recognizes that, if the dislocation splitting distance (width between two partial dislocations) was smaller than the grain size, two Shockley partial dislocations were generated from the grain boundary and went across grains as a perfect dislocation, leaving no microstructure change behind; whereas when the grain size was less than the splitting width, the partial dislocations were emitted from the grain boundary and then glided through grains, leaving a grain transected by a stacking fault [22]. Newly published results have explained that the stacking fault energy not only determines the critical grain size but also plays a significant role in the hardening rate [23].

As a summary of all computer simulations, the common point is that the grain boundary is not only the source but also the absorbed site of dislocations. Besides

dislocations and grain boundary sliding, mediated plastic deformation are both triggered by the atomic shuffling. At this time, it is very clear why the importance of the grain boundaries in nanocrystalline materials was discussed many times in earlier sections.

Although the above mentioned results provide insight into the deformation mechanism in nanocrystals, it is still not sufficient to understand the deformation transition within a wide range of grain sizes, because nearly all simulations are only concerned with grain sizes below 15 nm, which is less than critical value. As a result, comprehensive studies are desired and have recently been performed by two research groups. One attempt was afforded on Al using creep test [41] and the other studied Cu using tensile test [42]. Both results demonstrate that there indeed exists a “strongest size” as observed in the hardness measurements, which is approximately 18 nm and 14 nm in Al [100] and Cu [42], respectively. Across this critical value, there is a continuous change in the deformation mechanism. Figure 2-12 shows the deformation behaviors in different sized Cu [42]. The blue atoms are in a perfect FCC crystal, the yellow atoms are at stacking faults and twin boundaries, and the red atoms are in grain boundaries and dislocation cores. It is found that, as the grain size went beyond the critical value, the deformation is dislocation controlled, while the grain boundary sliding mechanism was dominant when the grain size was smaller than the crossover value. Of course, such change is not abrupt, i.e. the deformation involves two activities, but the degree of contribution to the deformation by these two activities varies with the grain size. Now, it has been acknowledged that the “inverse” Hall-Petch relationship is attributed to the increased sliding content at the grain boundaries with a decrease in the grain size.

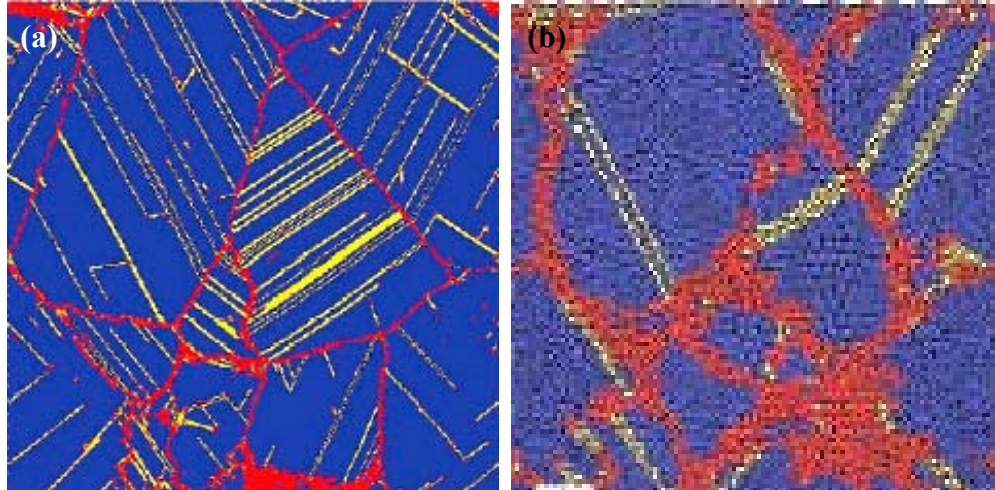


Figure 2-12. Deformation mode at different grain sizes in copper. (a) The structure after 10% deformation, $d = 49$ nm; (b) shows the same for a system with $d = 7$ nm. Here, the major deformation occurs in the grain boundaries [42].

It should be of note that the computer simulation has intrinsic shortcomings. For example, in computer simulations, regardless of the tensile or creep method, the samples deform at an unusual strain rate as high as 10^8 s⁻¹ and a short time scale of nano-second. Usually, the real tests are carried out at a strain rate lower than 1 s⁻¹. In addition, the starting materials constructed in simulations are all dislocation-free. However, actual nanocrystalline materials always contain either the processed dislocations within the large grains or the grain boundary dislocations. Accordingly, the computer simulation only renders a prediction, not a conclusive answer to the deformation as well as the other behaviors. Convincing experimental evidence needs to be provided to support the computer simulation results.

In conventional metals in which the plastic deformation is controlled by the dislocation motion, the resistance to the dislocation activities by the grain boundaries resulted in the hardening effect – the strength increases with continuous straining. On the basis of revealing the existence of the dislocation pile-up in nanocrystalline copper with a

mean grain size of 49 nm by computer simulation [42] and the direct observations of the considerable dislocation activities in 40 nm Ni under TEM [135], it appears that the strain hardening still comes from the dislocation pile-up theory when the grain size is larger than critical value. According to the classic theory, it can be inferred that strain hardening will be very low or even disappears as the grain size is reduced lower than the critical value, resulting in low ductility, especially the uniform tensile elongation. This seems to be in agreement with experimentally obtained results – low tensile elongation [5,11,12]. In addition, it has been proposed that the strain hardening rate is also related to the stacking fault energy; only if the stacking fault energy was low enough, then strain hardening could be achieved [42,140]. The calculated results provide evidence that strain hardening was not observed in Al – high stacking energy of 122 mJ cm^{-2} , but showed up in Pd – low stacking fault energy of 8 mJ cm^{-2} [42]. However, the experimental fact is that the strain hardening rate was very high in nanocrystalline materials and increased with decreasing the grain size [10,16]. For example, the electrodeposited Ni with a grain size 6-10 nm, having a stacking fault energy of approximately 150 mJ cm^{-2} [34], exhibited a much higher strain hardening rate [16]. The reasons are in part associated with the following issues. Due to the grain size distribution in real materials, which could be described to be composites [141], dislocation motions still exist in big grains. In addition, under tension, the level of plastic strain varies among grains of different size, and at a given level there exists a fraction of grains which deform only elastically [10,141]. In this case, the internal stresses that develop due to the strain incompatibility among various grain sizes cause strain hardening. Aiming to verify the computational

predictions, it is necessary to do studies on Al (very high stacking fault energy) at a grain size level of 10 nm.

The previously discussed mechanical phenomena caused by low temperature annealing and strain rate can now be reasonably interpreted using grain boundary sliding mechanism. It has been shown by computer simulation that grain boundary sliding was gradually involved with increasing the applied stress and the yielding was dislocation-generation controlled [42]. After the grain boundary relaxation, not only will the pre-existing dislocation and porosity be removed but also the dislocation emission from the grain boundaries would be more difficult. Thereby the microhardness or yield strength will increase after low temperature annealing (usually lower than 573K) [45]. It is well known that, in nanocrystalline materials, the grain boundary events such as atomic shuffling during plastic deformation are a short-range shift and also stress sensitive. In other words, the grain boundary sliding is time dependent. As has been acquired in the experiments, therefore, low strain rate led to the low strength [11,132]. In addition, with decreasing grain size – increasing the grain boundary fraction, the strain rate sensitivity is increasing.

2.6.2 TEM Observation

Because it has been discussed that the dislocation sources may no longer operate in nanocrystalline metals, it is not possible in a sense to examine the dislocations in the post-deformed samples. Yet, *in-situ* straining in TEM offers useful information. The nanocrystalline gold film, having an average grain size of 10 nm and a thickness of 10-20 nm, prepared by the ion beam sputter deposition has been employed to study the deformation behaviors by use of *in-situ* HRTEM at low strain rate [142]. The results show that there were no dislocation activities during and after the deformation, but

relative grain rotation as high as 15 degrees was detected [142]. Such observations strongly suggest that the deformation happened via the grain boundary sliding. However, similar studies on the pulsed laser deposited and DC magnetron sputtered Ni (17-19 nm) clarify that the prevalent dislocation nucleation and motion have been observed in grains as small as 10 nm [63]. It is probably related to the different stacking fault energies in these two materials. The stacking fault energy is approximately 150 and 50 mJ cm⁻² for Ni and gold, respectively [34]. In the confined geometry of nanocrystalline grains, the dislocation emission can be blocked if the stacking fault energy is low enough [140]. Of course, other factors such as the sample thickness could be involved. Moreover, it is not surprising to see clear evidence of dislocation activity in the silver sample with a grain size of about 110 nm [142], because considerable dislocations has been directly discerned in 40 nm Ni sample [135].

It is well known that, due to the high stacking fault energy, the deformation twinning in coarse-grained Al has never been detected. However, computer simulations suggested possible presence of the twins in nanocrystalline Al because of the partial dislocations' traveling through the grains [24,25]. Recently, increased attention has been paid to HRTEM observations for nanocrystalline Al [27,28,143]. The results indicate that the deformation twinning was observed in nanocrystalline Al within grains larger than 25 nm [143], Liao *et al.* also announced that no partial dislocations were inspected in grains smaller than 45 nm [27]. It is worth pointing out that the grains where the deformation twinning was detected were all more than Al's critical value of about 18 nm [41] predicted by computer simulations.

Based on the available TEM results, it is suggested that the deformation is assisted by the dislocation activity when the grain size is over the critical grain size. Within the low grain size regime, it is still not clear how much dislocations participate in the deformation process. Once again, TEM's thin sample problem should be taken care of. Computer simulation, where the sample's thickness is comparable with that of actual TEM specimen, has shown that the surface effect is proportional to the grain size [144]. For instance, in the sample with a grain size of 5 nm, the intergranular deformation increased at the surface, and there was a profound increase in the dislocation activity when the grain size was 12 nm [144]. Therefore, it is very valuable to make clear what observation in TEM are intrinsic properties of the nanomaterials and which observation are artifacts of the thin film geometry.

2.7 Thermal Stability of Nanocrystalline Metals

Even in conventional materials, the grain boundary diffusion rate is much faster than the lattice diffusion rate. A high volume fraction of grain boundaries in nanocrystalline materials will thus increase the diffusion paths. Furthermore, in the experimental aspect, the grain boundary diffusivities for nanocrystalline materials exceed the corresponding values in coarse-grained materials by several orders of magnitude [145-148]. It can therefore be imagined that, due to the large fraction of grain boundaries, the nanocrystalline materials under elevated temperatures are not thermodynamically stable, with a strong tendency to transform from nano-scale materials into coarse-grained polycrystals, i.e. grains grow; also, the growth kinetics in the nanocrystalline materials could be different from that operative in the conventional materials.

In general, the grain growth is a diffusion-controlled process and can be classified into two types: normal grain growth and abnormal grain growth. The former denotes that the grains grow in a rather uniform way. As a result, the distribution of the grain size and shape is relatively narrow. However, in some cases, a few grains may grow excessively by consuming the neighboring smaller grains. This process is known as abnormal grain growth. The kinetics of grain growth originates from the curvature of the grain boundaries. Whichever takes place, the resulted situation is only that the average grain size becomes increased. Hence, the nanocrystalline materials' wealthy properties such as high hardness [3] and low coercivity [149], which are all grain size dependent, may diminish or even vanish when they are applied in elevated-temperature environments. As a result, it is of immense importance and interests to investigate the thermal stability and growth kinetics in nanocrystalline materials for the purpose of future technological applications.

Studies concerning thermal stabilities in nanostructured materials such as Fe, palladium, copper, pure Ni and Ni-Fe alloys have already been paid a lot of attention in recent years [43-45,66,150-158]. The differential scanning calorimetry (DSC) investigations have shown that electrodeposited Ni samples with a grain size of 10 and 20 nm were stable only up to 353 K [150]. Within a temperature range of 353-562 K, abnormal grain growth was observed and with a continuous increase in temperature beyond this range, normal grain growth occurred [150]. Meaning, low temperature leads to sudden grain growth in few grains, and normal grain growth prefers high temperature. Figure 2-13 is an example of abnormal and normal grain growth in the electrodeposited Ni, whose beginning grain size is approximately 20 nm [45,155]. It is found that, in

Figure 2-13(b), just several grains grew and others remain unchanged after annealed at 493 K for 480 min [45]. However, heat treatment at 603 K resulted in normal growth, as shown in Figure 2-13(c).

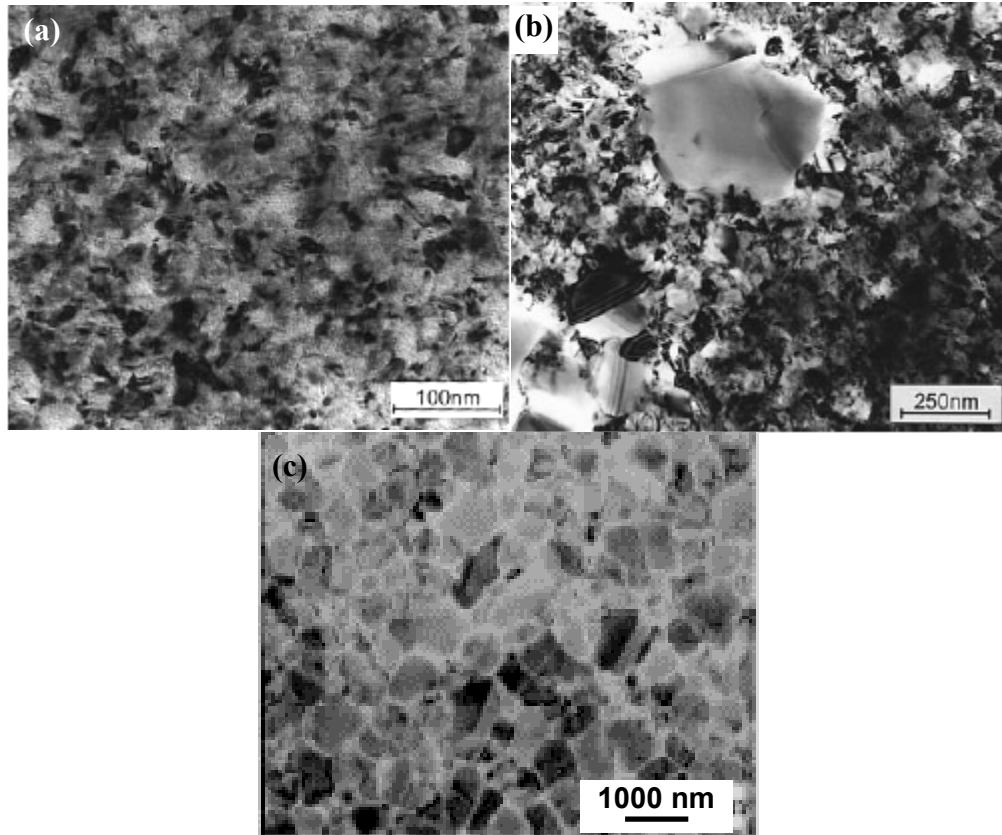


Figure 2-13. TEM images show microstructures of electrodeposited Ni. (a) as-deposited [45,155]; (b) abnormal grain growth at 493 K for 480 min [45]; (c) normal growth at 603 K for 20 min [155].

Even at the same temperature, the grain growth exhibits two distinct regimes. Isothermal results elucidate that grains grow faster in the early state and then follow a gradual increase in grain size with time. In the case of electrodeposited pure Ni where the applied temperature is 673 K, the grains grew rapidly from an initial value of 19 nm to about 120 nm after only 4 min annealing time, and beyond this time the grain size changed only slightly [156].

The existences of the grain boundary segregation [159-161], solute drag [162], impurities [150], second phases drag [163,164], pore drag [165] and chemical ordering [166-168] also can improve the thermal stability of nanocrystalline materials because of their drag-forces on the grain boundaries. For example, due to the formation of a second phase, nanocrystalline Ni-1.2%P exhibited no structural changes after annealing at temperatures up to 473 K [164]. In addition, the reported results for electrodeposited nanocrystalline Ni-50% Fe alloys reveal that the structure is much more stable than pure Ni, and abnormal grain growth only started to be seen at 673 K [45]. It is probably due to the effect of adding alloying element.

The grain growth of nanocrystalline materials upon the heat treatment may also be accompanied with a change in texture. The random texture of an electrodeposited Ni-45% Fe alloy upon annealing at 673 K for more than 60 min has been shown to change into a (111) texture [154]. However, the study of the Ni-50% Fe alloy has revealed that the grains' orientations were closer to random after annealing at 673 K for 90 min [45].

The grain growth is associated with the exponential dependency of the grain size on temperature through an Arrhenius-type equation [169]:

$$D^n - D_0^n = kt \exp(-Q/RT) \quad (2-3)$$

Here, D is the average grain size at time t , D_0 is the initial grain size, n is the time exponent, k is the constant, Q is the activation energy, R is the gas constant, and T is the absolute temperature. Among these variables, the time exponent n and activation energy Q are the key parameters to describe the grain growth kinetics. In the case of nanocrystalline Ni, several experiments have been performed by different groups. The primary grain size was at the scale of 20 nm and the applied temperature ranged from 463

to 683 K. All results reported the similar activation energy value, varying from 102 to 131 mJ/mol [44,45,155] which is comparable to the activation energy (108.3 mJ/mol [170]) for the grain boundary diffusion in coarse-grained Ni. As a result, it was suggested that the grain boundary diffusion controlled the grain growth in nanomaterials. For nanocrystalline pure Fe, however, two regions in terms of the grain growth have been suggested as follows [157]: at low temperatures, the activation energy number (100 mJ/mol) was consistent with that of nanocrystalline Fe; while at higher temperatures, it was 175 mJ/mol, corresponding to the literature value for the grain boundary self-diffusion in conventional Fe. However, it has not been widely accepted. Apart from the activation energy, the discussion on the time exponent n of nanocrystalline materials has also been published. It has been shown that the time exponent n value in nanocrystalline Ni was around 7 [155], which is much higher than classic data of 2 under ideal condition. The variation of n values in nanomaterials is still not well understood and the relevant results are also very small.

CHAPTER 3 EXPERIMENTAL PROCEDURES

This chapter will describe the detailed experimental procedures regarding the production of nanocrystalline Ni and Ni-Fe alloys, and characterization and testing of them.

3.1 Electrolyte Preparation

3.1.1 Ni-Fe Alloys

The electrolyte used to synthesize Ni-Fe alloys was composed of 1.2 M (mole) nickel sulfamate $\text{Ni}(\text{NH}_2\text{SO}_3)_2$ (nickel source), 0.5 M boric acid (H_3BO_3), 2 g/liter (L) L-ascorbic acid ($\text{C}_6\text{H}_8\text{O}_6$) and 0.5 g/L SNAP (sulfamate nickel anti-pit). Boric acid can hinder the formation of hydroxide [83], and L-ascorbic acid helps prevent oxidation of ferrous ions during electrodeposition [83,84]. SNAP has a function of removing hydrogen bubbles from the cathode surface, but does not get incorporated into the deposits. In order to fabricate Ni-Fe alloys with different compositions, an appropriate mass of $\text{FeCl}_2 \cdot 4\text{H}_2\text{O}$ or $\text{FeSO}_4 \cdot 7\text{H}_2\text{O}$ was added into each bath to satisfy the specified Ni/Fe ion ratio. For purpose of reducing the impurity level, all chemicals are certified brand and water was deionized. After all chemicals were completely dissolved, pH value was adjusted at room temperature (electrodeposition temperature). The pH value was measured by a Corning-brand pH meter with the error ± 0.04 . It has been discussed in chapter 2 that the internal stress is unacceptable if the pH is higher than 3 [80]. In addition, stress reducers such as saccharin were not used in this study in the interest of obtaining high quality samples. Based on analyzing the reported results, therefore, a low

pH value of 2 was chosen in the present study. In general, the initial pH value of as-prepared solution was about 3.6. Proper quantity of sulfuric acid or chloride acid was added into the solution to decrease the pH down to 2 at room temperature. To avoid incorporating un-dissolved particles in the deposits, finally, the solution was filtered using a vacuum filter with 0.45 μm membrane to eliminate the particles floating in the electrolyte. It should be noted that the ferrous ions are easily to be oxidized and thus it is better to make the deposition when the solution is still “fresh”.

3.1.2 Pure Ni

In the case of pure Ni, the relationship between the microstructures and electrodeposition parameters has been well established by our group [171]. The employed electrolyte was a sulfamate based solution, consisting of 1.53 M nickel sulfamate as nickel source, 15 g/L boric acid, and 0.07 g/L SNAP. Because there is no Fe ion in the solution, the ascorbic acid was not used here. In addition, for the same purpose in the issue of Ni-Fe deposit, no additives (stress reliever) were used. Because it has been recognized that a pH value of 4.6 to 4.8 usually resulted in high quality samples, the pH of 4.7 was adopted. The beginning pH value of the as-made solution is approximately 4.6. A small amount of nickel carbonate was added to bring the pH value up to around 4.7 at room temperature (298 K). In fact, pure nickel was electrodeposited at 313 K. Although the pH value, in theory, will decrease with increasing temperature, the change in pH was negligible in the present condition. Before applying electrodeposition, the solution was also filtered to remove the excess nickel carbonate and other particles.

It needs to be noted that, in both cases, the electrolyte was deaerated by blowing nitrogen gas for at least 60 minutes to remove the air immediately prior to electrodeposition.

3.2 Substrate Preparation

The substrate was a pure copper disc with a diameter of 35 mm and thickness of approximately 100 μm . Two types of substrates were used in this study: annealed (AN) and cold-worked (CW). The CW substrates were annealed under argon environment at 698 K for 1 hour to prepare AN substrates. The annealed substrates show an out of plane texture of (100), which was proven to be the most suitable crystallographic orientation to avoid nodule formation. The texture of CW substrate is (110).

The substrates should be well electropolished prior to electrodeposition. The AN or CW substrates were cleaned using citranox on both sides and rinsed in water. After drying in air, the substrates were glued onto the working electrode – a piece of steel also having a diameter of 35 mm using conductive silver epoxy glue. The substrates were then put into a box furnace to cure at 373 K for 1 hour. After complete cooling down, once again, the substrate was cleaned by citranox and washed in water. After this step, the substrate was electropolished in a solution including 82.5% phosphoric acid and 17.5% deionized water using the potentiostat/galvanostat PAR system. The applied potential was -1.1 V and the time was about 25 to 40 minutes depending on individual substrates. The cathode was a piece of stainless steel and the electrolyte was stirred vigorously to remove the hydrogen bubbles that form on the cathode surface during polishing. Once the electropolishing was finished, the substrate was rinsed in deionized water and put into a 10% sulfuric acid solution balanced with deionized water for 15 sec to activate the surface. Then, the substrate was immediately transferred into the deposition cell.

3.3 Electrodeposition

3.3.1 Experimental Setup

The potentiostat/galvanostat PAR 273 system and the rotator were interfaced with a personal computer. The rotation speed can be controlled by computer or be manually set up. The required temperature was kept using a FisherScientific brand iso-temperature water bath with an error of ± 0.2 °C. The anode was a 10 x 10 cm² square platinum foil, and the potential was measured relative to a saturated calomel electrode (SEC). Figure 3-1 shows the configuration of the experimental and schematic setups.

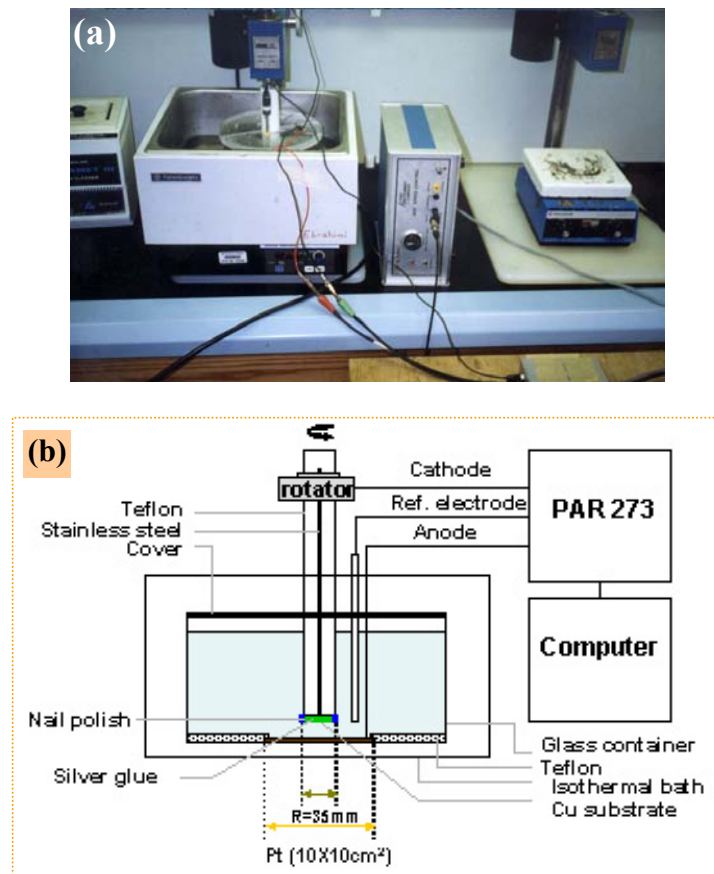


Figure 3-1. Experimental setup of (a) real and (b) schematic pictures.

3.3.2 Electrodeposition of Ni-Fe Alloys

It has been acknowledged that the current density plays a critical role in electrodeposition. In order to find proper current density, cyclic voltammetry was conducted at a rate of 16.7 mV s^{-1} between 0 and -2 V to analyze the relationship between the potential and the current at room temperature. The electrolyte was made of 1.2 M nickel sulfamate, 0.15 M ferrous chloride, 0.5 M boric acid, 2 g/L L-ascorbic acid and 0.5 g/L SNAP. The pH value is 2.1 and the rotation speed was 500 rpm (rotation per minute). Figure 3-2 demonstrates the current density versus applied potential, where the arrows denote the increase and decrease in the applied potential. The limit current density is defined as the point at which the current will saturate or level off with further increasing potential, and it can be seen that the limit current density is about 36 mA cm^{-2} under current condition. The suitable deposition current density cannot exceed this limit. But, if it is too small, the deposition speed will be low. Accordingly, the current density of 25 mA cm^{-2} was chosen in depositing Ni-Fe alloys.

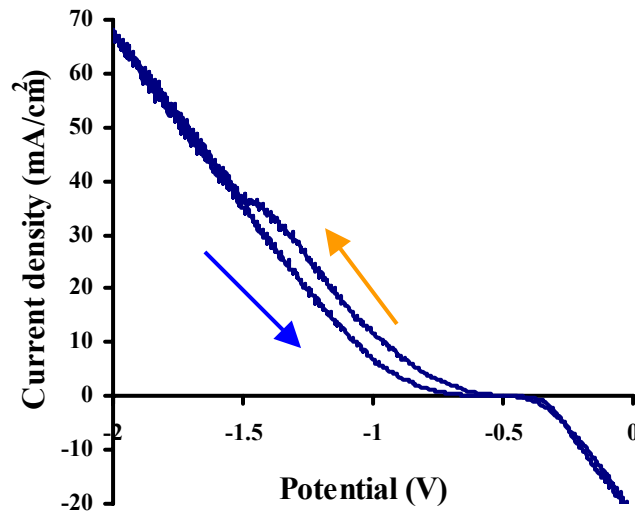


Figure 3-2. The change in the current density with the applied potential.

In summary, Ni-Fe alloys were deposited at room temperature with a DC (direct current) current density of 25 mA cm^{-2} . The pH value and the rotation speed were 2.0 and 500 rpm, respectively. For some selected deposits, the pH value was 3.6 and the rotation speed was 400 rpm. The applied time was between 2 and 5 hours, resulting in the thickness varying from 20 to 40 μm .

3.3.3 Electrodeposition of Pure Ni

It has been identified that Ni deposits with good qualities can be produced using a current density of DC 25 mA cm^{-2} [171]. Temperature and rotation speed were 313 K and 400 rpm, respectively. The pH value was 4.7.

For Ni, both thin and thick samples were fabricated. The thin one (35 μm thick) was deposited for 2 hours. In the case of thick deposits, two variable speed pumps were used to circulate the solution between the plating cell and a reservation of solution bath to compensate for the consumed Ni ions in the deposition cell. The electrolyte in this solution bath was exactly the same as that in the plating cell. Its temperature was also kept in an iso-temperature water bath at 313 K.

3.4 Sample Preparation

After electrodeposition was finished, the cathode was taken out deposit and cleaned it with water. Then, the deposit was removed from steel plate by putting the assembly into the methylene chloride to dissolve the silver epoxy. After this point, the deposit was cut into four rectangular strips ($24 \times 6 \text{ mm}^2$) using a slow diamond saw. Finally, the copper substrate was stripped off in a commercial solution, which does not attack the deposit.

3.4.1 Tensile Test Samples

The strips were placed between two CW copper sheets, whose sizes were similar to those of the strips. Afterwards, they were put between two dog-bone shaped steel templates. Using metal files, the strips were ground into template's dog-bone shape with a width of 3 mm and a gauge length of 5 to 10 mm. For annealing, the well prepared samples were sealed into a quartz tube filled with argon gas. The box furnace was firstly pre-heated up to the desired temperature and then the tube was put in the furnace and held for the required time period. Once completed, took out the tube and left it in air to cool down.

3.4.2 TEM Samples

3 mm discs were punched out of strips (as-deposited or annealed). TEM samples were prepared using a twin-jet eletropolisher at approximately 257 K. The electrolyte was composed of 32 ml perchloride acid, 150 ml butanol, 53.3 ml butyl-cellose, and 245.3 ml ethyl alcohol. The applied voltage was 80 V.

3.5 Analysis Methods and Experimental Characterizations

3.5.1 Compositional Analysis

EPMA JEOL 733 superprobe was employed to analyze the composition distribution with an error of $\pm 0.5\%$. The cross-section sample was made by cool mounting method to avoid thermal effect on the results and then was mechanically polished up to 0.05 μm alumina powder. In order to evaluate the deposit's quality, two different scans were applied: one along thickness and the other along radial direction. For every type, at least two scans were performed. The scan step size was 2 μm per step in thickness direction and 1 mm per step in the radial direction.

The sulfur impurity level in one deposit was analyzed by Wah-Chang company using a LECO CS-444 carbon-sulfur analyzer, where the combustion method with an infrared detection system was employed.

3.5.2 X-ray Diffraction

Philips APD 3720 X-ray diffractometer (XRD) was used to evaluate the phase type and the crystallographic texture. The x-ray peak line broadening is a suitable method to characterize the grain size and lattice strain of nanocrystalline materials by means of the line-profile program. The Line Profile Analysis technique is a technique that uses the shape of X-ray diffraction peak profiles to achieve the information about the microstructure of crystalline materials, such as the finite grain size and lattice disorder. Briefly the mean grain size, D , and the lattice strain, e , vary differently with the diffraction angle θ as given by the following equations:

$$D = \frac{k\lambda}{\beta \cos \theta} \quad (3-1)$$

$$e = \frac{\beta}{4 \tan \theta} \quad (3-2)$$

Here, k is a constant, λ is the wavelength of radiation source and β is the integral breadth. The “Line Profile” software that accompanies the Philips APD 3720 system allows the analysis of the single line profile in three stages: (1) correction for the background, Lorentz polarization, and stripping of the $K_{\alpha 2}$ contributions, (2) Stokes/Fourier deconvolution and (3) grain size and internal strain calculation based on the above equations.

In the case of Ni-Fe alloys, the single line method was applied using the (111) peak. The corresponding standard peaks were scanned from a standard sample – a piece

of single crystalline quartz. It is worthy of mentioning that the applied parameters such as step size and the time per step in scanning the standard quartz must be the same as those for the analyzed sample. In order to get accurate data, the difference in the peak position (2θ) between the analyzed and standard peaks should be less than 5 degrees.

3.5.3 Transmission Electron Microscopy (TEM)

Apart from the XRD technique, TEM (JEOL 200CX) is also a powerful tool to measure the grain size and its distribution. For grain size measurement, dark field pictures were taken at high magnifications. The grains were measured at both the longest direction and the diagonal perpendicular to it. The average value was considered the grain size. Usually, more than 200 grains were measured to obtain statistically accurate results. The number frequency was plotted versus the grain size, and then the mean grain size was calculated. Assuming that every grain has a spherical shape, the volume fraction versus the grain size was plotted.

JEOL 2010F TEM was utilized to estimate the grain size scale in nanocrystalline deposits. More importantly, the grain boundary and the lattice defects such as dislocations and twins were characterized in a high resolution TEM (HRTEM).

3.5.4 Scanning Electron Microscopy (SEM)

The surface features of as-deposited samples were checked in a JEOL JSM 6400 SEM. Because the thickness of deposits was less than 40 μm and the ordinary micrometers is not accurate at this level, the precise thickness was measured in SEM. In addition, SEM was practiced to exam the fracture surfaces, crack propagation mechanism, fracture geometry as well as the features on the side surface of fractured tensile-tested samples.

3.5.5 Microhardness Measurement

Microhardness was measured using a Micromet II microhardness tester with an applied load time of 15 sec. The applied load was chosen to be 10 or 25 kgf. At least 10 measurements, conducted at different regions, were made for each same sample. In microhardness measurement, the surface condition is very important, especially in the case of thin films, where the applied load is small and the resulting diagonal size is only a few micrometers. Figure 3-3 displays the Vickers indentation marks on as-finished and polished sample surfaces at similar applied load and time. It is obvious that the surface of the as-deposited sample is very rough and the indentation mark is not sharp and it is difficult to distinguish the edges of the impression, as shown in Figure 3-3(a). However, Figure 3-3(b) demonstrates that the indentation mark is sharper and clearer in the polished samples. Moreover, its diagonal length of $10.9\ \mu\text{m}$ is larger than that from unpolished surface, which was measured to be $9.8\ \mu\text{m}$. As a result, the measured hardness from polished surface is more accurate and also lower than that measured on the unpolished surface.

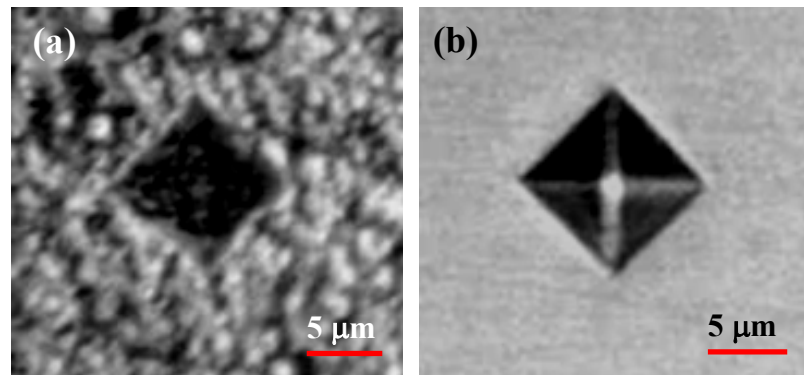


Figure 3-3. Vickers indentation marks on (a) unpolished and (b) polished surfaces.

The flow stress was estimated from microhardness value according to the following equation:

$$\sigma_{flow} (MPa) = \text{Microhardness} (kgf / mm^2) \times 1.422 \times 6.895 / 3 \quad (3-3)$$

3.5.6 Uniaxial Tensile Test

MTS (materials test system) and Instron systems were utilized to carry out the tensile test. The sample was hold by a pair of pneumatic grips with an applied pressure of approximately 655 MPa. Two pieces of AN copper were put on both sides of every specimen shoulder to avoid the damage by grips. For thick Ni specimens, due to their large thickness, the grips were directly applied on them without the use of AN copper protective sheets. In addition, the alignment is very important and was carefully examined. The required strain rate was achieved by changing the cross head speed. In the present dissertation, the applied strain-rate arranged from 10^{-2} to 10^{-6} s^{-1} . A 18 bits A/D converter in connection with the LABVIEW software was used for data acquisition.

3.5.7 Nanoindentation

It has been discussed in chapter 2 that both strain-rate and grain boundary relaxation play the key role in the mechanical behaviors. There is, therefore, a critical need for examining the strain-rate sensitivity in nanocrystalline metals. In order to obtain accurate and believable results, at least two tests are required under similar conditions. That is, many samples are needed. Up to now, however, it is still difficult to produce large amounts of deposits. Nanoindentation is an alternative method to evaluate the effect of the strain-rate. The apparent advantage is in that multitudinous tests with different strain rates can be conducted on only one sample.

As-deposited and annealed Ni-15%Fe alloys as well as as-deposited pure Ni were tested. The sample surface was mechanically well polished using the Buehler brand 0.03 μm alumina powder. A load rate control model was applied using a Triboindenter, with a pyramidal tip shape and a tip radius of approximately 200 nm. The applied load rates were 2000 μN and 200 μN per second. This nanoindenter's capability is 10 mN and the applied maximum load in the present study was 6000 μN . That is, the applied load was firstly increased at a constant loading rate up to 6000 μN and held at this maximum value for a given time period. Then, the samples were unloaded at the respective loading rates. For each load rate, 5 indentations were performed.

3.5.8 Heat Treatment

Isothermal and isochronal heat treatments were employed to evaluate the thermal stability and the grain growth kinetics in nanocrystalline Ni-Fe alloys. Although it has been confirmed that it is almost same in the grain size and internal strain, there still is little difference in microstructures such as the grain size distribution between different deposits. To rule out the possible influence from different deposits, in either situation, the different pieces were cut from the same deposit. The applied temperature ranged from 373 K to 773 K.

With respect to isochronal annealing, the Ni-21%Fe samples were annealed at temperatures of 373, 423, 473, 523, 573, 623, 673, 723 and 773 K for 90 min. The 373 K and 423 K annealings were carried out in boiling water and silicon oil, respectively. The heat treatments at high temperatures (from 473 to 773 K) were done in a preheated box furnace. After annealing, the samples were cooled in air and then cleaned with a 30% sulfuric acid + 20% nitric acid + water solution to remove the oxide layer. Finally, the

microhardness, grain size and internal strain were measured following the procedures mentioned above. Different pieces from the same deposit were used for different annealing temperatures.

Based on the results from the isochronal study, it was recognized that there is a transition temperature at 575 K [29] regarding the grain growth. In the case of the isothermal heat treatment, therefore, two temperatures were determined for examining the grain growth kinetics, respectively in the low and high temperature ranges. One was 523 K lower than 573 K, and the other was 673 K larger than the transition temperature. Two pieces of Ni-15%Fe samples were cut from one strip and then polished using Buehler brand 0.03 μm alumina power. The samples were isothermally annealed at 523 K and 573 K for 5, 15, 30, 60 sec and 1, 5, 15, 30, 60, and 90 min each. This time, the salt bath containing 50% KNO_2 + 50% NaNO_3 was used to relieve the oxidation problems encountered in the isochronal processing of Ni-21%Fe alloys at high temperatures. The salts were put in a stainless steel cup and pre-melted in the box furnace at temperatures of 523 K or 573 K, respectively. A K-type thermocouple thermometer was used to monitor the salt-bath temperature. After the desired temperature was attained in the bath, the sample was put in and held for the required time. Once annealing was completed, the sample was taken out and immediately put it in the water. After each heat treatment, the microhardness, grain size, internal strain and crystallographic texture were analyzed. To compare with the results for the Ni-21%Fe alloys, the isochronal annealing was also done on the Ni-15%Fe samples using the salt baths for heat treatment.

CHAPTER 4 SYNTHESIS AND CHARACTERIZATION OF NI-FE ALLOYS

4.1 The Effect of Chemical Species

When making Ni-Fe deposits, two salts are commonly used as the iron source, i.e. iron sulfate and iron chloride. Some people like ferrous chloride [9,17,81,84,87,88,172], and the others prefer the ferrous sulfate [83,113,173]. A study has reported that the current efficiencies are different in sulfate and chloride baths [74]. As a consequence, the deposit's composition could be affected by the anion type. In order to investigate this effect, different Ni-Fe alloys were fabricated from sulfate and chloride salts, respectively.

Figure 4-1 plots the Fe content in the deposits as a function of the Fe ion concentration. It can be seen that the iron salt type has no significant influence on the iron amount of the deposits.

Another remained question is whether the deposits produced from different iron sources have different microstructures such as the grain size. To answer this question, four deposition baths were designed. There were two baths at low and high iron ion concentration regions, respectively. Furthermore, the two baths having similar iron ion concentration were made respectively from the ferrous sulfate and the ferrous chloride. The bath parameters and properties of the deposited Ni-Fe alloys are summarized in Table 4-1. Note that all the alloys were deposited using exactly the same deposition parameters such as current density, rotation speed and temperature. Once again, it is confirmed that the effect of anion type on the iron content in the deposits is negligible. It is also found that the Ni-Fe alloys have quite similar grain sizes if they were deposited

with similar iron ion concentrations, independent of the salt type. For example, with 0.005 M iron ion concentration, the iron content and the grain size are respectively 14.9% and 10.4 nm for the Ni-Fe alloys deposited from the sulfate salt, and the corresponding values are 14.8% and 10.3 nm in the deposit made from chloride salt. In addition, detailed examinations disclose that the deposition potentials and the post-deposition pH values are also consistent with each other for a given Fe^{2+} concentration, i.e., no effect of the anion type. With the consistency of the potentials and the pH values between the baths with different anion types, it is expected that the deposited Ni-Fe alloys have similar iron contents and grain sizes.

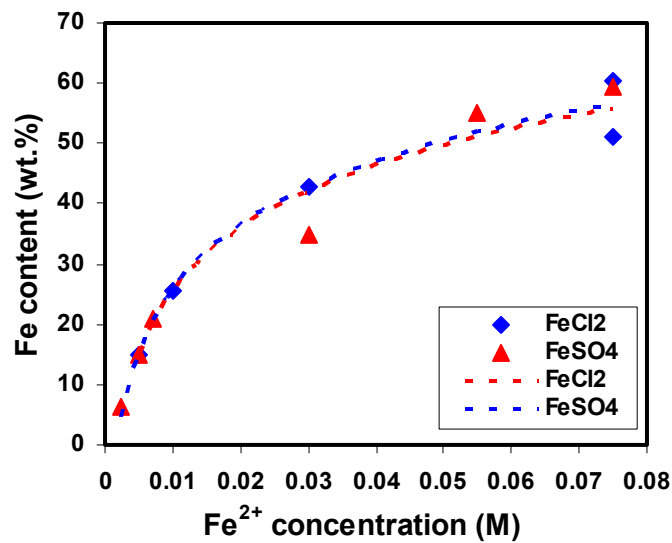


Figure 4-1. The effect of anion type on the dependency of the iron content of the Ni-Fe alloys on the Fe^{2+} concentration of the bath.

Table 4-1. The deposition parameters and properties for four designed baths.

Sample #	Chemical species	Fe⁺² (M)	pH before	pH after	potential (V)	Fe (wt.%)	Grain size (nm)
L22	FeSO ₄	0.005	2.0	1.92	1.492	14.9	10.4
L23	FeCl ₂	0.005	2.03	1.97	1.442	14.8	10.3
L24	FeSO ₄	0.075	2.01	1.96	1.542	59.3	9.2
L25	FeCl ₂	0.075	2.0	1.95	1.466	60.3	6.8

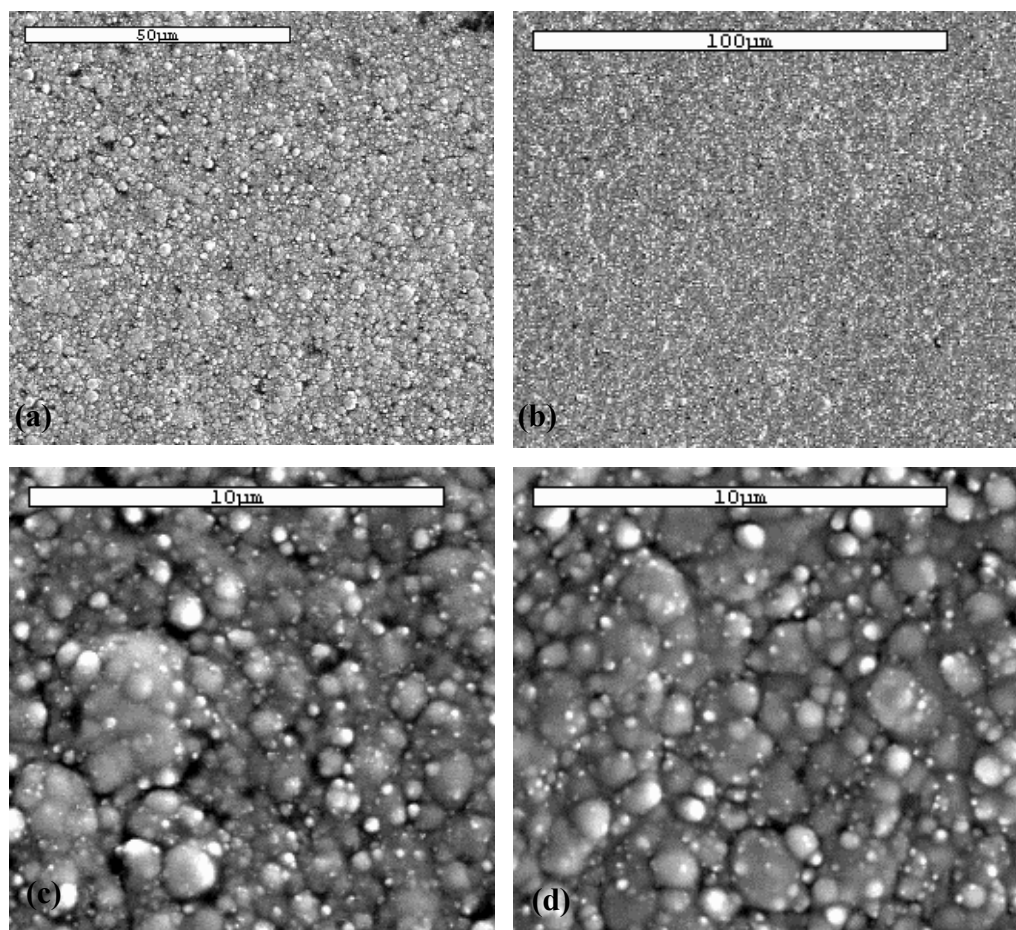


Figure 4-2. SEM surface morphology of the Ni-15%Fe alloy deposited from different iron sources. (a) FeSO_4 and (b) FeCl_2 at low magnification; (c) FeSO_4 and (d) FeCl_2 at high magnifications.

Figure 4-2 displays the solution side surface of the Ni-15%Fe deposits made from sulfate and chloride baths, respectively. The solution side is defined as the finished side of deposits, i.e., the surface in touch with the solution during the electrodeposition. It is apparent that there are no differences between the morphology of deposits fabricated from different iron sources. But it can be seen in Figures 4-2(c) and (d) that the as-deposited surface is very rough.

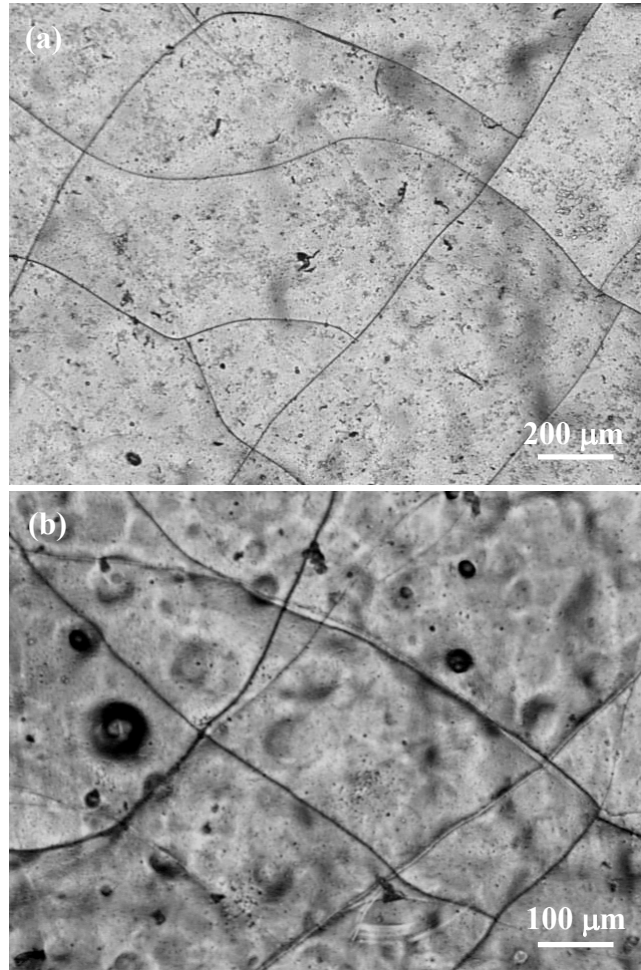


Figure 4-3. Optical micrograph of the surface of the Ni-60%Fe deposits fabricated using (a) FeSO_4 and (b) FeCl_2 .

The high iron content deposits exhibited extensive microcracking due to the presence of large internal stresses. A detailed study of the surface of deposits produced from baths containing FeSO_4 or FeCl_2 revealed that the anion type has no noticeable effect on the extent of microcracking. Figure 4-3 presents an example of such a comparison for the Ni-60%Fe alloy. Consequently, it is concluded that the deposits made from chloride and sulfate baths had similar properties. In the following sections, the type of bath will not be of a consequence.

4.2 Compositional Analysis

4.2.1 The Effect of Ferrous Ion Concentration

The deposition parameters and the measured properties of the electrodeposited Ni-Fe alloys are summarized in Table 4-2. The iron concentration in the deposits as a function of Ni to Fe ion ratio is plotted in Figure 4-4. The Ni/Fe ion ratios were calculated based on the concentration of the electrolytes used for the deposition of the Ni-Fe alloys. Initially, with increasing the Ni/Fe ion ratio, the iron content of the deposits decreased rapidly, which is consistent with previous studies [17,80]. When the Ni/Fe ion ratio was increased beyond 200, a further increase of the Ni/Fe ion ratio did not decrease the iron content significantly. Even as the Ni/Fe ion ratio is over 200, the iron content in deposits is still as high as 15%, which is related to the anomalous phenomenon in the Ni-Fe co-deposition system [73-77].

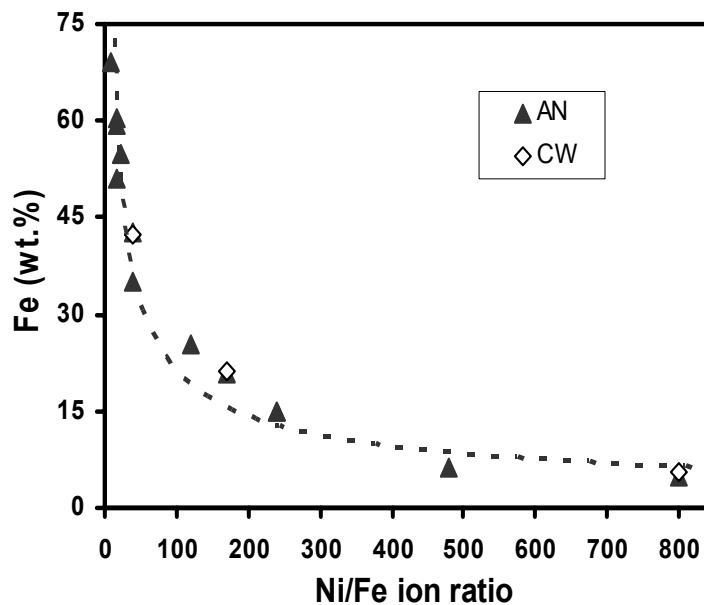


Figure 4-4. The iron content of deposited Ni-Fe alloys as a function of the Ni/Fe ion ratios.

Table 4-2. Electrodeposition parameters and properties of various Ni-Fe alloys.

Sample #	L01	L02	L25	L24	L15	L03	L05	L06	L04	L13	L07	L20	L21	L22	L23	L10	L11	L12	L16	L08	L09
FeCl ₂ .4H ₂ O (mM)	150	75	75			30	30		10						5						
FeSO ₄ .7H ₂ O (mM)				75	55			30		7	7	7	7	5		2.5	2.5	2.5	1.5	1.5	1.5
Rotation Speed (rpm)	500	500	500	500	500	500	500	500	500	500	500	500	500	500	500	400	400	500	500	400	500
Substrate	AN	AN	AN	AN	AN	AN	CW	AN	AN	AN	CW	AN	AN	AN	AN	AN	AN	AN	CW	AN	AN
pH (± 0.04)	2	2	2	2	2	2	2	2	2	2	2	2	2	2	2	3.27	2	2	2	2	2
Deposition time (h)	1.5	1.5	3	3	1.5	3	3	3	3	3	3.5	4	4	4	4	4	4	3	5	4	4
Fe (wt.%)	69	51	60.3	59.3	55	42.7	42.3	35	25.5	21	21.2	21	21	14.9	14.8	6.0	4.2	6.2	5.6	4.0	4.7
Grain size (nm)	3.7	11	6.8	9.2	11.4	11	10	10.5	10.8	14	10.5	12.5	12.2	10.4	10.3	29	20	18	22	88	52
Strain (%)	---	0.736	0.535	0.73	0.687	0.664	0.622	0.567	0.387	0.326	0.267	0.287	0.308	0.199	0.15	0.09	0.2	0.133	0.069	0.064	0.036
MicroHardness (VHN)	440	507	496	579	542	583	687	640	830	805	896	---	---	898	900	605	642	720	572	360	548
Std. Dev. of Hardness (VHN)	25	19	36	44	43	32	52	34	35	42	46	---	---	52	35	34	28	38	41	48	18
σ_{flow} (MPa)	1438	1657	1621	1892	1771	1905	2245	2091	2712	2631	2928	---	---	3003	2941	1977	2098	2353	1869	1176	1791

In Cheung et al.'s study [17], using a sulfate-based solution with no agitation, a Ni/Fe ion ratio of 7.5 led to an alloy of approximately Ni₇₂Fe₂₈ composition. However, in the present study, a Ni/Fe ion ratio of 8 using a sulfamate-based solution resulted in a Ni₃₁Fe₆₉ composition. This difference is attributed to the different deposition parameters, such as electrolyte type, pH value, current density, temperature and rotation speed, which have strong influences on the composition of alloys [6,83,172]. For example, the rotation speed has a direct effect on the iron concentration of the deposit [81]. A comparison of the composition of L11 with L12 sample (see Table 4-2) indicates that the iron content increases with increasing the rotation speed. However, the difference in the composition of L08 and L09 is within the accuracy of microprobe analysis. The increase in the iron concentration is attributed to a reduction in the diffusion layer thickness [174]. Also, a comparison of the composition of L10 with L11 deposit reveals that an increase in the pH of the electrolyte led to a higher iron content. However, an increase in the pH for an unstirred nickel sulfate electrolyte has been reported to decrease the iron content [83]. The results presented in Figure 4-4 indicate that the copper substrate condition (annealed or cold-worked) did not affect the iron concentration of the deposits.

4.2.2 Compositional Distribution

Not only is the average composition important but also the compositional distribution plays a key role in discussing the properties of electrodeposited metals because the non-uniform composition distribution usually results in the inhomogeneous microstructures. It has been documented that the differences in mechanical properties can be related to the inhomogeneity of microstructures [11]. As a result, it is of importance to evaluate the compositional distribution in the deposited samples. In addition, it is

desirable to know whether deposits fabricated under similar conditions consistently show the same compositions.

Two deposits of L13 and L20 (see Table 4-2) were picked to compare in every aspect. In the gross, it is observed from Table 4-2 that the average iron concentration, the grain size measured by XRD and the internal strain are all almost same between L13 and L20 deposits.

For purpose of evaluating the uniformity of the composition distribution, microprobe scans were applied on the cross section of the deposits along thickness and radial directions, which offer the comprehensive overview regarding the composition distribution. Figure 4-5 illustrates the scan positions for the L20 deposit and the chemical analysis results. Scans 1, 2 and 3 were perpendicular to the deposit surface. Scan 4 was parallel to the deposit surface and the measurements were taken at the mid-thickness along the radius of the deposit. The results shown in Figures 4-5(b), (c), (d) and (e) demonstrate that the composition distribution throughout the deposit is quite homogeneous. The change in different scans is within the microprobe analysis error of $\pm 0.5\%$. Figure 4-6 shows the same analysis for L13 sample. Again, it is clear that the compositional distribution in this deposit is uniform, indicating the homogeneous microstructure through the whole deposit. In addition, the average iron content in the sample L20 is about 20.8%, which is similar to the L13's mean iron weight percent of 20.7%. As a result, not only the composition distribution is homogeneous in each deposit, but also there is no significant difference between them.

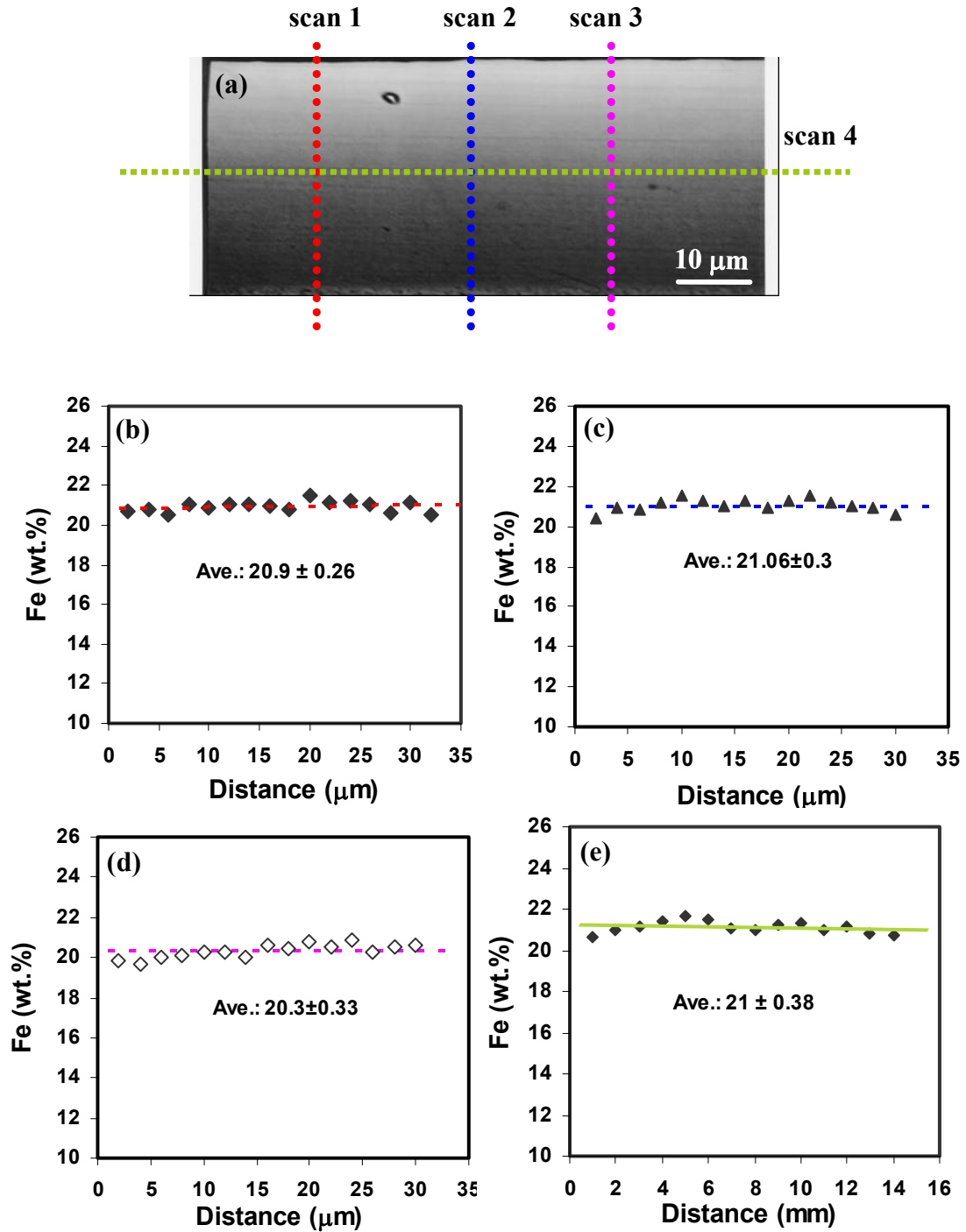


Figure 4-5. Microprobe analysis results for the L20 sample. (a) the orientation of the scans relative to the cross section of the deposit; (b) (c) and (d) the iron composition along the thickness direction; (e) the iron distribution along the radial direction.

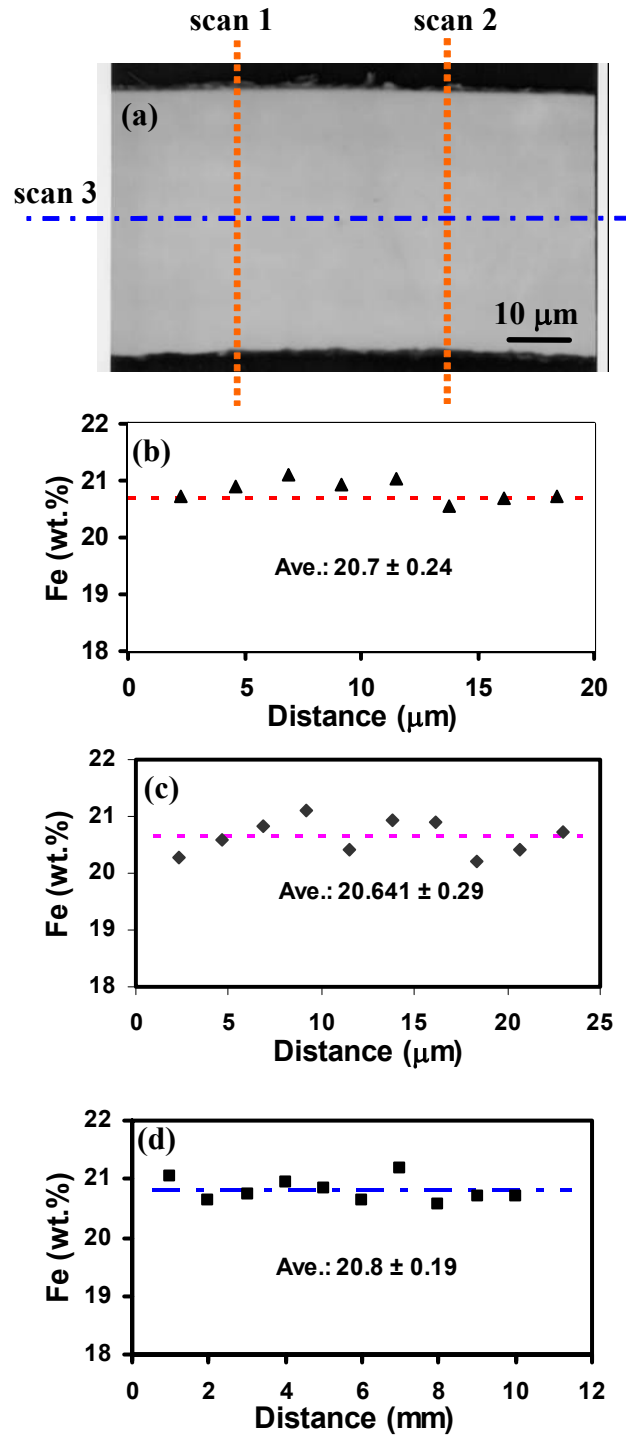


Figure 4-6. Microprobe analysis results for the L13 sample. (a) the orientation of the scans relative to the cross section of the deposit; (b) and (c) the iron composition along the thickness direction; (d) the iron distribution along the radial direction.

Figure 4-7 exhibits the potential as a function of deposition time during the fabricating of a Ni-21%Fe alloy. The results show that the potential was relatively constant throughout the deposition period. With regard to the electrolyte, in the case of the Ni-21%Fe deposits, the Ni/Fe ion ratio of electrolyte is 171 prior to electrodeposition. Assuming the thickness of deposit is 35 μm (the actual thickness varies from 30 to 36 μm), the consumed iron mass is approximately 0.058 g. The detailed calculation shows that the ratio of Ni to Fe ions is about 185 in solution after electrodeposition. From Figure 4-4, it is obvious that the change in the Ni/Fe ion ratio from 171 before deposition to 185 after finishing plating does not affect the iron content in the deposit significantly. Moreover, extrapolated from the simulated curve (dashed line) in Figure 4-4, the difference in composition resulted from the change of Ni/Fe ion ratio is only 0.6%. Accordingly, all the electrodeposition parameters were approximately constant during plating, which explains well that the produced Ni-Fe alloys have homogeneous composition distribution, as shown in Figures 4-5 and 4-6.

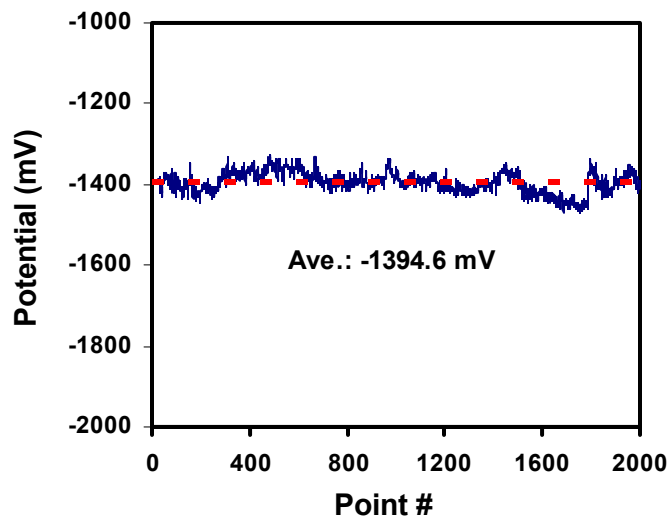


Figure 4-7. The potential versus the deposition time, where the dotted line represents the average value.

In addition, another factor indicating the quality of the electrodeposited metals is the impurity level. Still in an example of Ni-21%Fe deposit, the average sulfur content was measured to be as low as 74 ppm (parts per million by weight). This value is much smaller than the reported value in deposits produced with the addition of saccharin in the bath, where the sulfur level has been as high as 884 ppm [45]. This is probably due to the absence of additives in the current study.

4.3 Microstructure

4.3.1 Grain Size and Lattice Strain

Figure 4-8 illustrates the variation of grain size with the iron content of the deposited Ni-Fe alloys at 500 rpm cathode rotation. When the iron content was decreased below 15%, the grain size increased very rapidly. This finding is consistent with Cheung et al.'s results [17] although they employed different deposition parameters. The published results show the gradual decrease in the grain size with increasing iron content [17,84]. However, the grain size here remained approximately constant (~11 nm) for electrodeposited FCC alloys with iron content in the range from 15 to 55%. When the iron content was increased beyond 55%, the grain size started to decrease further with raising the iron content. As shown in the section 4.3.2, the crystal structure of the alloy changed from FCC into BCC+FCC at the iron content of 69%, where the grain size decreased drastically to 3.7nm. Consistently, a previous study has shown that for Ni-Fe-Co alloys, a mixture of BCC+FCC crystals has a finer grain size than either BCC or FCC deposits [7].

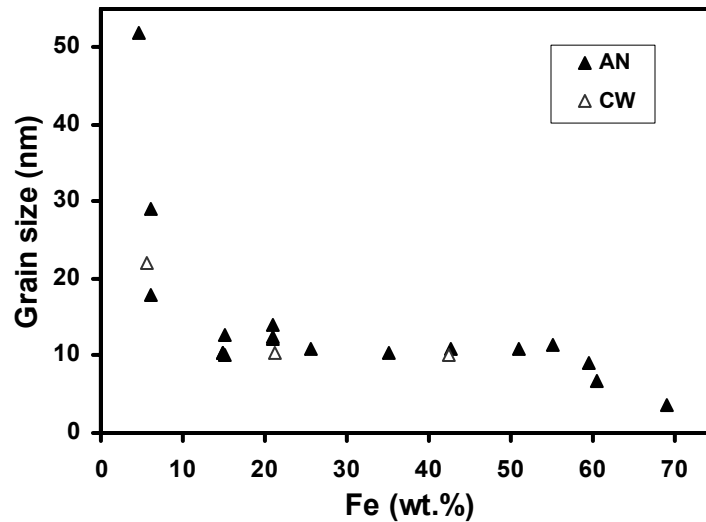


Figure 4-8. The effect of iron content on the grain size of electrodeposited Ni-Fe alloys.

In addition to the deposition parameters, the substrate also influenced the grain size of the deposits. Deposits made on the CW substrates showed a smaller grain size than the deposits formed on the AN substrates. This observation is in contradiction with the results reported for pure nickel deposits [171]. However, as seen in Table 4-2, a comparison of the L03 with L05, L07 with L13, and L09 with L16 deposit reveals that the effect of substrate is most noticeable for low iron content alloys. Also as shown in Figure 4-8, a small change in the iron content below 7% iron can have a significant effect on the grain size. The largest variation in the grain size due to the substrate was observed in deposits of L16 and L09. The L16 deposit, which was made on the CW substrate, also exhibited high iron content. Within the iron content from 15% to 55%, the CW substrates have no significant effect on the iron content and thus no considerable influence on the grain size. Therefore, the apparent effect of the substrate in nickel-iron deposits may be in reality associated with a change in the iron content. A comparison of L11 with L12 and L08 with L09 deposit shows that the rotation speed also affects the grain size. The alloys

deposited with 400 rpm had larger grain sizes than those deposited with 500 rpm because of the lower iron content of the former deposits.

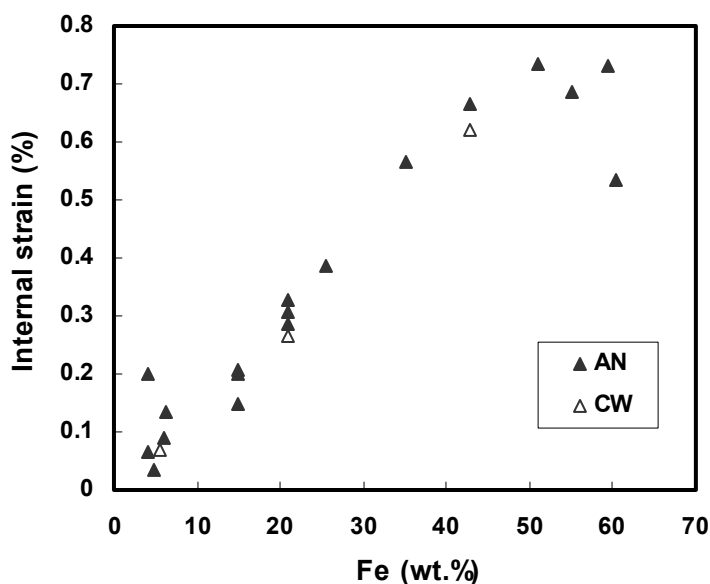


Figure 4-9. The lattice strain as a function of the iron content in the electrodeposited Ni-Fe alloys.

Figure 4-9 presents the lattice strain values versus the iron content. These values were calculated based on the XRD peak broadening. It is found that the lattice strain of the deposits strongly depended on their iron content. In addition, the condition of copper substrate (CW vs. AN) did not have a noticeable effect on the lattice strain. While there is some scatter in the lattice strain at low iron contents, the lattice strain increased linearly with increasing the iron content of the FCC Ni-Fe alloys. The scatter in the low iron alloys may be attributed to the variation in the grain size in these deposits. In general, the smaller the grain size, the larger the lattice strains at a given composition. Since the Ni-Fe alloys with iron content equal or more than 15% had similar grain sizes of approximately 11 nm, the increase in the lattice strain cannot be ascribed to the change in the grain size. The formation of defects such as vacancies, dislocations, voids and twins as well as the

lattice misfit between the deposit and the substrate can contribute to the development of lattice strains.

4.3.2 Texture and Lattice Parameter

Figure 4-10 displays the XRD spectrum of Ni-69%Fe and Ni-60%Fe alloys. The results indicate that the deposit with 69% Fe had BCC + FCC mixed phase, as shown in Figure 4-10(a). As the iron content is equal or below 60%, the Ni-Fe alloys exhibited single FCC phase, which is in a good agreement with the previous results [84]. Figure 4-10(b) is an example of the XRD diffraction pattern of Ni-60%Fe alloy.

The results of texture analysis are presented in Table 4-3, where the intensities of the peaks are normalized relative to the peak with the highest intensity. The alloys with low iron concentrations (4-6.2%) showed a strong (100) texture. Furthermore, with increasing the grain size, the strength of the (100) texture increased which is consistent with the results reported for electrodeposited pure nickel [3]. However, FCC Ni-Fe alloys rich in iron ($\geq 15\%$) exhibited almost random orientation with a slight tendency for the (111) planes to be parallel to the substrate surface. It has been previously shown that an increase in the crystallite size enhances the texture of pure nickel [3]. Therefore, the stronger textures observed for the low iron content alloys are due to their large grain sizes. Comparing the alloys deposited under similar conditions using different substrates, it was observed that substrate has little influence on the texture (compare L03 with L05, L13 with L07 and L09 with L16).

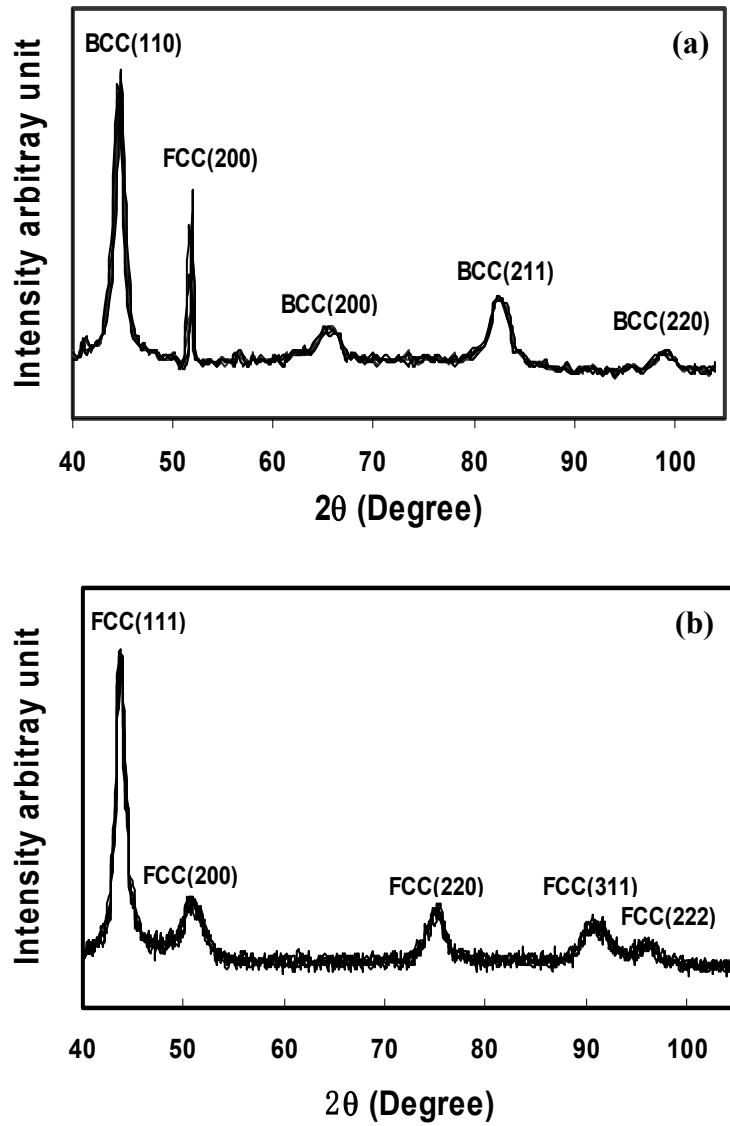


Figure 4-10. XRD diffraction patterns of (a) Ni-69%Fe alloy showing the duplex structure and (b) Ni-60%Fe alloy exhibiting single FCC phase.

Table 4-3. The texture of electrodeposited nickel-iron alloys.

FCC peak	111	200	Fe content (Wt.%)	Grain size (nm)
Stand. int.	100	60		
L25	100	18	60.3	6.8
L24	100	12	59.3	9.2
L15	100	17	55	11.4
L02	100	39	51	11
L03	100	25	42.7	11
L05 ^a	100	19	42.3	10
L06	100	41	35	10.5
L04	100	24	25.5	10.8
L13	100	21	21	14
L07 ^a	100	28	21.2	10.5
L21	100	22	21	12.2
L22	100	25	14.9	10.4
L23	100	27.8	14.8	10.3
L12	14	100	6.2	18
L11 ^b	7	100	4.2	20
L16 ^a	7	100	5.6	22
L10 ^b	6	100	6.0	29
L09	6	100	4.7	52
L08 ^b	4	100	4.0	88

^a Cold worked substrate was used.

^b Rotation speed was 400 rpm.

Due to the strong (100) texture in the low iron deposits, the {100} planes are mostly parallel to the substrate surface. For the high iron content alloys with slight (111) texture, the {111} planes are partially inclined to the substrate surface. Therefore, the lattice parameters of the FCC were calculated by converting the measured average atomic plane spacing of the (111) planes ($a_{FCC} = \sqrt{3}d_{111}$) and (200) planes ($a_{FCC} = 2d_{200}$) for high and low iron content deposits, respectively. Ni-69%Fe sample was approximately considered as pure BCC alloy while calculating the lattice parameter ($a_{BCC} = \sqrt{2}d_{110}$).

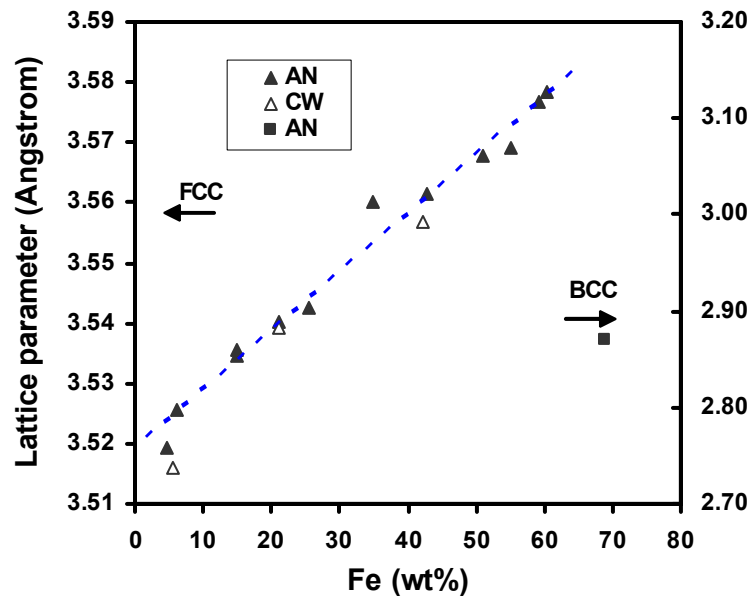


Figure 4-11. Lattice parameter as a function of iron content in deposited Ni-Fe alloys.

Figure 4-11 plots the lattice parameter with the iron content. The results show that the lattice parameter increased with increasing the iron content in the deposited FCC nanocrystalline nickel-iron. Also, the substrate condition has no apparent influence on the lattice parameter. The lattice parameters measured in this study are slightly smaller than the previously reported values for electrodeposited Ni-Fe alloys [81], which matched the values for the thermally prepared alloys [85]. Because of the residual stresses in the

deposited alloys, the lattices are slightly distorted. As a result, the lattice parameters calculated from diffracting planes parallel and normal to the substrate plane are expected to be different. In the deposits studied here, the stresses were tensile within the deposit plane and compressive along the growth direction. Consistently, the lattice parameters reported, which were measured based on the diffraction from the crystallographic planes that were mostly parallel to the substrate surface, are smaller than the thermally prepared alloys.

4.3.3 TEM Observations

Generally speaking, the measurements by use of XRD technique only give the average grain size. TEM has apparent advantages of not only providing direct observations of the microstructure but also offering the detailed grain size distribution. In order to evaluate the accuracy of the measured grain size using XRD technique and further characterize the consistency between different deposits fabricated under the same conditions, L07 and L13 deposits having a iron content of about 21% were chosen to do TEM analysis. Figure 4-12 shows the bright field, dark field and selected area diffraction pattern of L07 sample. It can be seen in Figures 4-12(a) and (c) that there is no obvious tendency for several grains to cluster together. Presumably, the grain boundaries are dominantly type of high angle grain boundary. Also, the microstructure is quite homogeneous and the grain size distribution is relatively narrow. Figure 4-12(b) demonstrates the diffraction pattern of ring type, indicating a fine grain structure. The homogeneous distribution of the diffraction spots in the rings indicates the absence of microtexture.

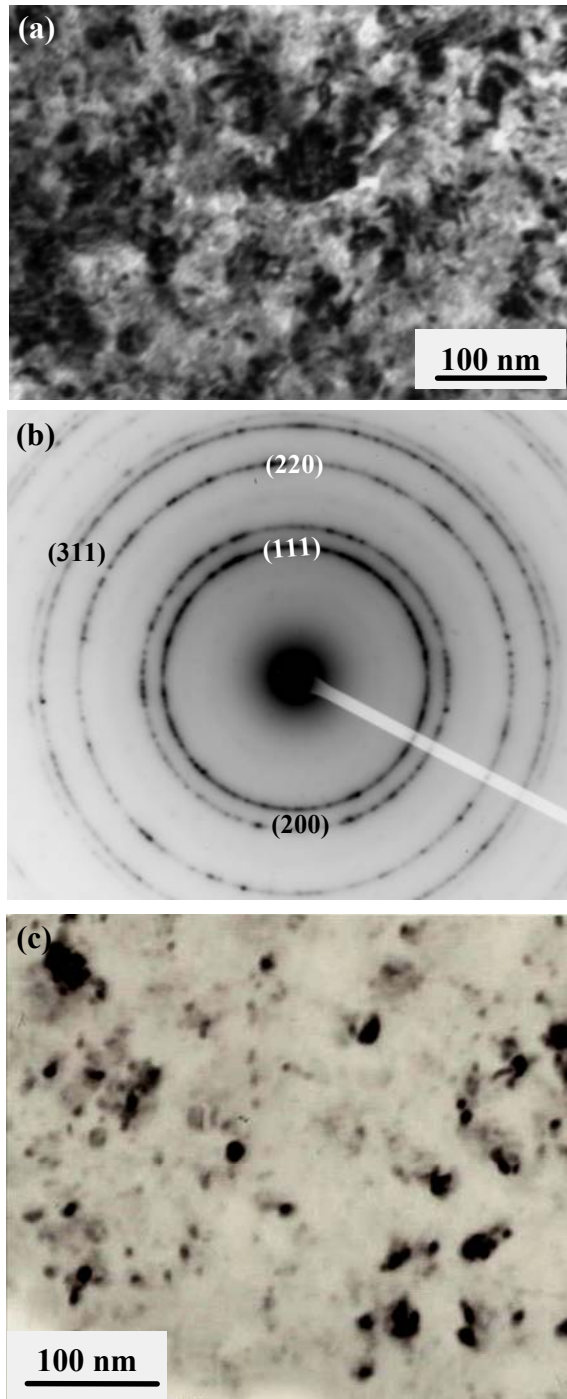


Figure 4-12. TEM images showing (a) bright filed and (b) corresponding selected area diffraction pattern and (c) dark filed for L07 deposit.

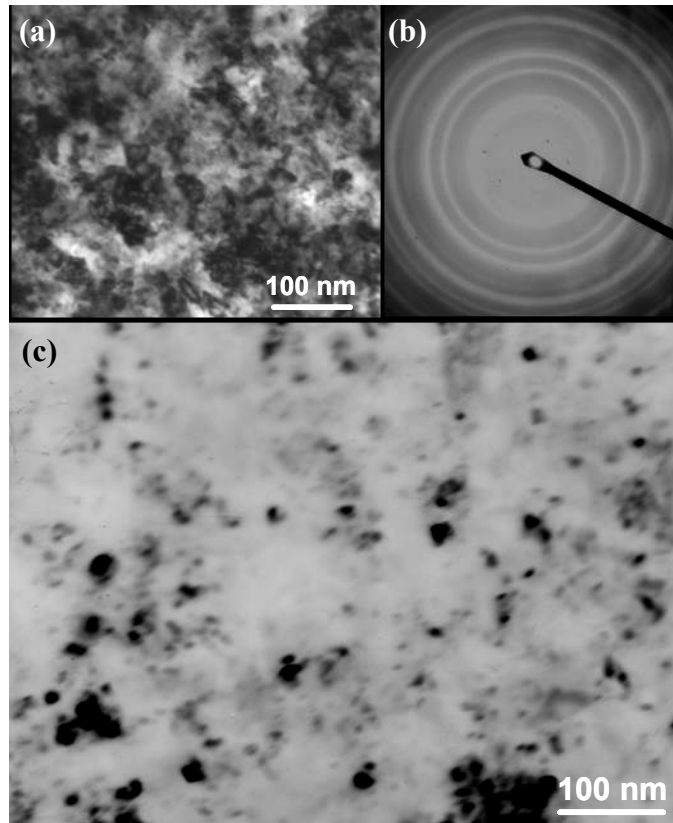


Figure 4-13. TEM micrographs showing (a) bright filed and (b) corresponding selected area diffraction pattern and (c) dark filed for L13 deposit.

Figure 4-13 illustrates the same TEM analysis for deposit L13, which also exhibited a narrow grain size distribution and uniform microstructure. A comparison between L07 and L13 reveals that, as shown in previous sections, there are no significant differences in their microstructures between them. It is reasonable to make detailed analysis on one given deposit and then assume that all deposits produced with exactly similar conditions have the same microstructures. It is worthy of noting that, although not shown here, there always exist some nano-pores with a size of about 1-2 nm in the electrodeposited metals [18,72].

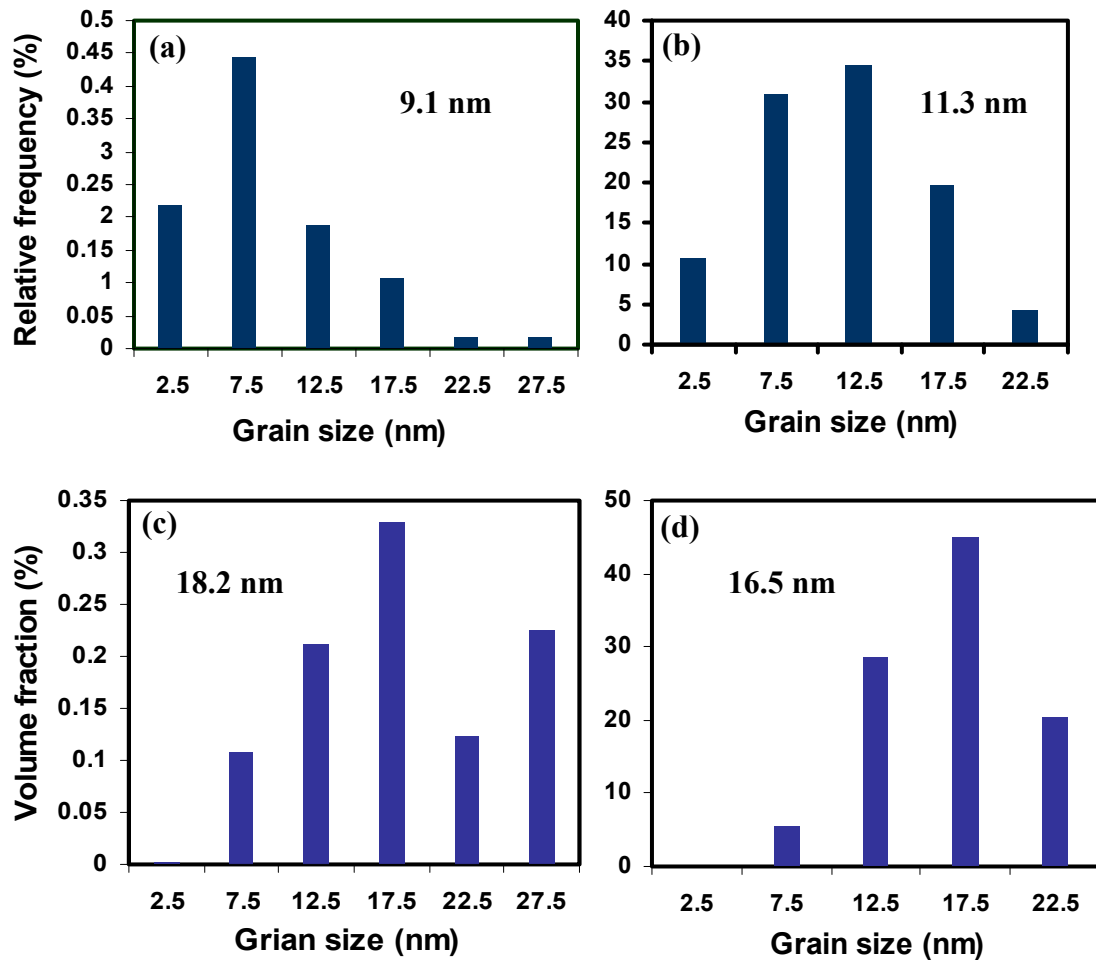


Figure 4-14. The grain size distribution based on the grain number in as-deposited (a) L07 and (b) L13 samples; (c) and (d) show the volume fraction of L07 and L13 deposits, respectively. Inset number in every figure denotes the average grain size.

On the basis of several dark field images of high magnifications, the grain size distribution in L07 and L13 deposits were evaluated and plotted in Figure 4-14. For every sample, more than 150 grains were measured. Generally, these two deposits have similar grain size and grain size distribution, as stated in last section. The mean grain sizes of L07 and L13 samples are 9.1 and 11.3 nm, respectively, which are comparable with the values (10.5 and 14 nm for L07 and L13, respectively) measured by XRD line

broadening method. That is, the XRD is a reliable technique to characterize the grain size, though it cannot estimate the grain size distribution. Careful examinations discovered that, although the microstructure is similar, there were still slight difference between deposits of L07 and L13. For example, the L07 deposit's grain size distribution is slightly wider than that of L13. Also, many grains have the size scale from 5 to 10 nm in the L07 sample, while, in the case of L13, more grains range from 5 to 15 nm.

Comparing Figures 4-14(a) and (b) with Figures 4-14(c) and (d), it is found that the apparent average grain sizes computed on the account of volume fraction are larger in comparison to the values calculated based on the frequency number. The reason is that the grain volume is proportional to d^3 (d is the grain size), and thus even a few large grains can occupy quite large fractions of the total volume, resulting in a bigger average grain size value. Additionally, a comparison of Figures 4-14(c) with (d) reveals that the broader grain size distribution led to a larger shift in the grain size based on the volume fraction relative to that calculated from frequency number. Such a shift is about 5 nm in the L13 sample, whereas it is as high as 9 nm for the L07 specimen, which has a wider grain size distribution. Generally saying, when considering the role of grain size in properties, the frequency based grain size value is used. Of course, the grain size computed from the volume fraction also deserves attention.

4.4 Microhardness

The measured microhardness values have been given in Table 4-2. Assuming that the solid solution strengthening in deposits with 4-7% iron is approximately the same, the effect of grain size on the flow stress was evaluated amongst these deposits. The flow stress was estimated according to $\sigma_{\text{flow}} = (\text{Hardness})/3$. The change in the flow strength

with grain size followed the Hall-Petch relationship, as presented in Figure 4-15. A comparison with the Hall-Petch relationship for the pure nickel deposits [3,10] showed that the addition of about 4-7% iron caused significant solid solution strengthening.

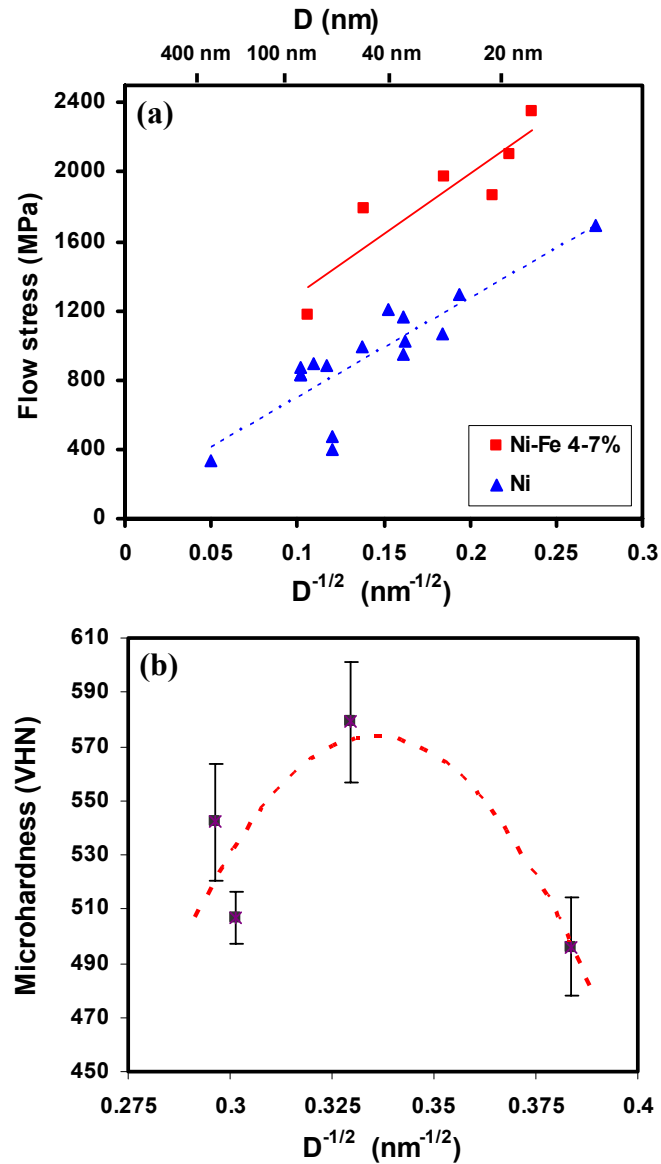


Figure 4-15. Flow stress as a function of grain size; (a) iron content from 4-7% and (b) deposits have a iron range of 51 to 60%.

However, as the grain size is below 15 nm, an inverse Hall-Petch phenomenon was observed, as shown in Figure 4-15 (b), where the solid solution hardening effect was neglected for deposited Ni-Fe alloys with the iron content of 51 to 60%. A maximum

hardness occurred at a grain size of approximately 10 nm. Similar observations have been obtained in previous studies on Ni-Fe alloys [9,17,119,120]. For instance, the electrodeposited Permalloy (Ni-20%Fe) exhibited the strongest hardness at the grain size of 12 nm [9], similar to the current results. In addition, computer simulation suggested that such phenomena are due to the change in deformation mechanism from dislocation controlled to grain boundary sliding dominated at the crossover grain size [41,42].

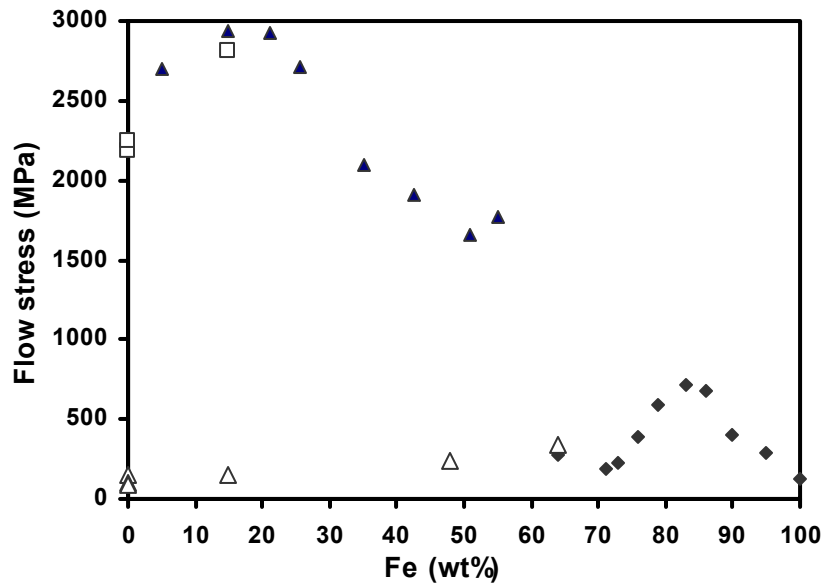


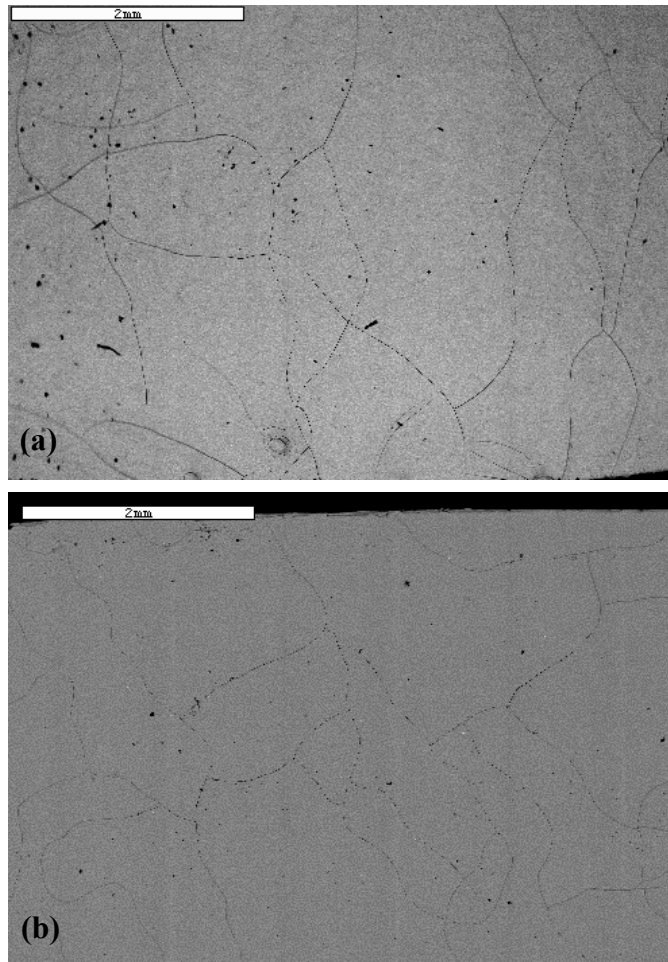
Figure 4-16. Flow stress as a function of iron content. ▲ nanocrystalline nickel-iron alloys; □ nanocrystalline nickel and nickel-iron alloys from references [9,10,119]; △ conventional nickel-iron alloys from reference [175]; ◆ conventional polycrystalline nickel-iron alloys taken from reference [176].

Deposits with equal or more than 15% iron had approximately similar grain size (~11 nm), and therefore the strength of FCC nickel-iron alloys could be investigated as a function of the iron content, as shown in Figure 4-16. In this figure, data for pure nickel [10,119], Ni-13% Fe [9] and Ni-5% Fe with grain size of 11 nm are also included. The Ni-5% Fe data point was extrapolated from the Hall-Petch curve shown in Figure 4-15(a). According to the results presented in Figure 4-16, electrodeposited FCC nanocrystalline

alloys show the maximum strength at approximately 15-25% iron. So far as we know, there are no systematic data for the strength of conventional FCC nickel-iron alloys as a function of iron content. However, the handbook data for the conventional FCC alloys [175] indicate no maximum in strength and only a slight increase in the strength due to solid solution hardening with increasing the iron content. It is interesting that for the iron rich conventional alloys the strength shows a maximum around 18% nickel [176], as shown in Figure 4-16. Such maximum in strength at ~18% Ni is probably associated with the formation of duplex FCC+BCC structures. A recent study [49] suggests that there is a larger probability of forming ordered Ni₃Fe in nanocrystalline nickel-iron alloys due to the faster grain boundary diffusion in comparison to the conventional alloys. Therefore, the occurrence of the maximum strength in the vicinity of Ni₃Fe composition maybe associated with the ordering of the structure. It should be noted that the ordering behavior could not be detected by the XRD analysis performed in this investigation. Within the nanocrystalline FCC alloys, the higher strength values for the pure nickel and nickel rich alloys in comparison to the iron rich alloys can be attributed to the change in shear modulus with the iron content. For example, the estimated strength values of pure nickel and Ni-51% Fe with the grain size of 11 nm are 2220 MPa and 1657 MPa, respectively. The shear modulus, G , decreases significantly with the addition of iron, and the shear modulus values for pure nickel and Ni-51% Fe are 85.7 GPa and 64.5 GPa, respectively [177]. Consequently, the σ_{flow} / G values for these two deposits are comparable (pure Ni = 25.9×10^{-3} and Ni-51% Fe = 25.7×10^{-3}).

4.5 Microrcracking

The internal strain in deposits increased with increasing the iron content, as shown in Figure 4-9. A network of microcracks was observed on the surface of deposits with equal or more than 35% Fe. Further studies revealed that the cracking pattern depended on the iron content in the deposits. Figure 4-17 illustrates the change of microcracking paths with the iron content.



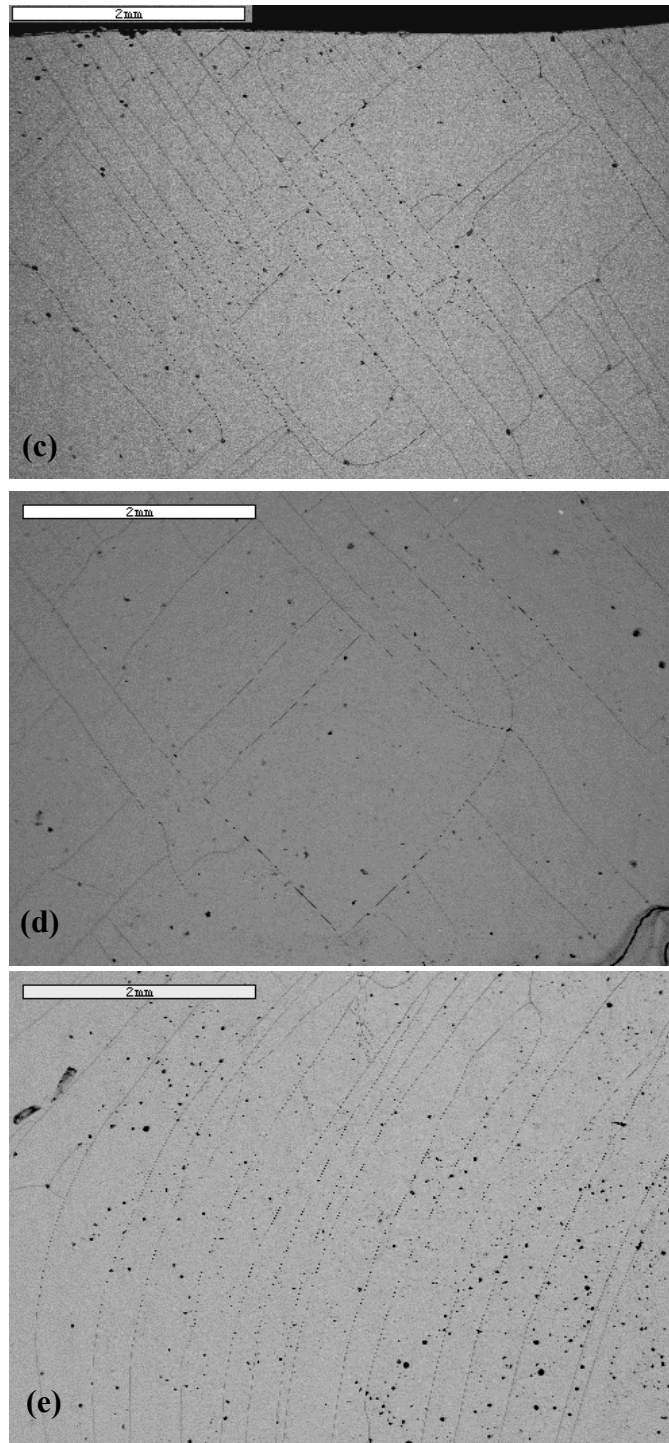


Figure 4-17. Microcracking pattern in different Ni-Fe alloys. (a) 69% Fe, AN substrate; (b) 55%Fe, AN substrate; (c) 51% Fe, AN substrate; (d) 42.7% Fe, AN substrate; (e) Similar composition as (d), CW substrate. The horizontal direction is parallel to the rolling direction of the substrate.

For the BCC + FCC alloy, the paths of microcracks exhibited a random pattern (Figure 4-17(a)), which is consistent with previous studies of the Ni-87% Fe alloy [87,88]. In addition, in case of FCC alloys with the iron content equal or larger than 55%, the microcrack patterns still displayed the random paths, as seen Figure 4-3 and Figure 4-17(b). For FCC alloys with an iron concentration less than 51%, however, the paths of microcracks changed dramatically. The microcracks developed along two distinct directions, which were perpendicular to each other, as shown in Figures 4-17(c) and (d). Moreover, the angles between cracks and the rolling direction of the copper substrate were approximately 45 degrees. Since the nanocrystalline alloys do not show a strong in-plane crystallographic texture, the geometry of the crack pattern should be associated with the substrate texture. The substrate texture is anticipated to influence the development of residual stresses in the deposits, which in turn would affect the crack path. Consistently, the condition of the copper substrate also influenced the microcracking pattern. For alloys deposited on the CW substrates, the microcracks developed along only one set of lines, which were curved, as shown in Figure 4-17(e). The difference in the microcracking pattern due to the change in the crystal structure suggests that internal stresses were developed differently in FCC and BCC alloys.

Assuming that the internal stress-state is biaxial with $\sigma_{xx} = \sigma_{yy}$, and $\sigma_{zz} = 0$, it can be shown that:

$$\sigma_{xx} = \sigma_{yy} = -\frac{E\varepsilon_{zz}}{2\nu} \quad (4-1)$$

Here E is the modulus of elasticity, ν is the Poisson's ratio and z denotes the direction perpendicular to the substrate surface. As a first approximation, we have assumed that the XRD analysis is mainly due to the residual strain along the growth

direction (ε_{zz}). It is acknowledged that this is just a rough approximation, in particular for the high iron content alloys. Based on such assumption, the σ_{xx} values were calculated from equation (4-1) and are presented in Table 4-4. The associated E values, which depend on the compositions, are also given in Table 4-4. The results presented in Table 4-4 show that, for FCC alloys deposited with iron content beyond 35%, the internal stresses are comparable to the strength of the alloy as measured by the microhardness testing. Consistently, these alloys demonstrated extensive microcracking. However, cracking did not happen when the iron content was below 35%, which is again consistent with the fact that the level of internal stresses was much smaller than their measured strength. Comparing L05 with L06, it is speculated that one direction cracking in the L05 deposit, Figure 4-17(e), is probably associated with the lower internal stress relative to its flow strength.

Table 4-4. The calculated internal stresses and predicted tensile strength of deposits.

SAMPLE #	I25	L15	L02	L03	L05*	L06**	L04	L13	I09
Fe (wt.%)	60.3	55	51	42.7	42.3	35	25.5	21	4.7
σ_{flow} (MPa)	1621	1771	1657	1905	2245	2091	2712	2631	1791
E (GPa)	155	160	168	184	184	191	203	210	221
σ_{xx} OR σ_{yy} (MPa)	1382	1832	2063	2037	1908	1806	1311	1140	133
Microcracking	Yes	Yes	Yes	Yes	Yes	Yes	No	No	No

* Cold worked substrate was used.

** Some microcracking was observed near the edges of the deposit.

4.6 Discussion

The current results show that the addition of iron into nickel resulted in a reduction in the grain size, as seen in Figure 4-8. In the case of electrodeposition, in general, the decrease in the grain size can be realized by increasing the number of the grain nucleation sites. It has been admitted that both the high potential and the foreign molecules have a function of increasing such nucleation sites [178]. As a result, in the present study the decrease in the grain size is in part related to the addition of the iron element. Figure 4-19 plots the potential versus the deposition time for fabricating pure nickel. The average potential was -1255.9 mV. A comparison between Figures 4-18 and 4-7 reveals that the over-potential increased after adding the iron element, which is probably another reason why the addition of the alloying element iron into nickel led to the reduction in the grain size. The constant grain size within the iron range of 15% to 55% is probably due to no significant changes in the potential within this iron range. The further reduction in the grain size, as the iron content is beyond 55%, may be associated with the tendency of the development of duplex structure of BCC + FCC phases, which usually leads to the finer grains [7].

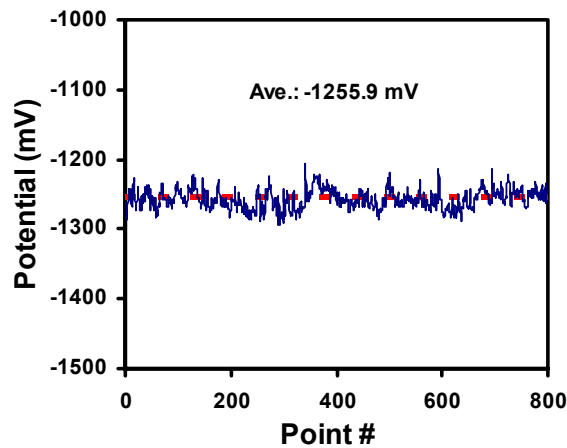


Figure 4-18. The potential versus the deposition time for pure nickel.

Recently, using the atomistic interactions, the orientation dependency of the surface energy in electrodeposited Ni-Fe alloys has been calculated [179]. The results reveal that the $\{111\}$ plane has the lowest surface energy, and the next is $\{100\}$ plane [179]. In other words, there is a competitive process between the development of (111) and (100) textures. Based on the energy minimization theory, a (111) texture is preferred. However, during the deposition, hydrogen codeposition always takes place. Simulation proposes that $\{100\}$ plane is more active to absorb hydrogen than $\{111\}$ plane; also, the surface energy of $\{100\}$ plane decreases faster than $\{111\}$ plane due to the modification by hydrogen [179]. As a result, a closely random texture, as confirmed by the current study, is anticipated. The strong (100) texture in low iron content alloys is consistent with the previous results for pure nickel [3,171]. Such observations imply that the reduction of nickel still dominated the electrodeposition in the case of low iron deposits.

Electrodeposition is an effective technique to produce nanocrystalline materials. But, a major disadvantage of this method is the generation of high internal stress, especially in the high iron content alloys, where it is so high that microcracks develop, as presented in Figures 4-3 and 4-17. Several theories, for example the lattice misfit between deposit and substrate, hydrogen evolution, lattice defects and crystallite joining theory, have been proposed to explain the origin of the internal stress [86]. Generally, the hydrogen codeposition depends on the current density, overpotential and electrolyte agitation. For all deposits, the current density and the rotation speed were the same in this study. In addition, Table 4-1 suggests that the overpotentials were not dependent on the bath composition. The hydrogen codeposition theory, therefore, does not hold here. As to the lattice misfit theory, the substrate usually affects only the first few micrometers of the

deposit. Secondly, with an increase in the iron content, Figure 4-11 demonstrates that the lattice parameter increased to approach the copper's lattice constant of 3.6148 Å, i.e. the misfit decreases with increasing iron concentration, in contradiction to the increase in the internal stresses with the iron content. Such being the case, this mechanism is also ruled out. As a consequence, the defects generated during electrodeposition are suggested to be the source of the internal stresses. Because the applied deposition temperature was low, the relaxation of the deposits was negligible. The rearrangement of atoms takes place only on the surface between the electrolyte and the deposit. The increase of the iron content in the bath may reduce the surface diffusion. Therefore, more microstructural defects are anticipated in the high iron deposits, resulting in the high internal stresses. Furthermore, it has been shown that the internal stress level changes along the growth direction in the case of the high iron alloys [88], which is to some extent relevant to the release of the built-up internal stress due to microcracking.

4.7 Summary

Without the use of any additives, nanocrystalline Ni-Fe alloys with various compositions were deposited onto annealed and cold worked substrates via a galvanostatic electrodeposition technique in sulfate and chloride baths. The composition of different Ni-Fe alloys was varied by changing the Ni/Fe ion ratios in the electrolytes. The results show that the anionic species did not have significant influences on the properties of deposits; neither did the type of substrate. The composition was primarily dependent on the Ni/Fe ion ratio. Furthermore, detailed characterization revealed that the compositional distribution is homogeneous, and the sulfur level is lower than reported results [45].

An increase in the iron content within the 4-15% resulted in a significant grain refinement. Parallel to this variation in the grain size, the texture accordingly changed from a strong (100) texture into a slight (111) texture. Beyond this range, increasing the iron content did not further decrease the grain size within the FCC composition regime. The grain size was the smallest in the alloys with the BCC + FCC duplex microstructure. The lattice parameter of the FCC deposits increased linearly with an increase in the iron content and so did the lattice strain and the internal stress. When the internal stress was high enough, i.e., the iron content was more than 35%, a network of microcracks was observed on the surface, and the microcracking pattern seemingly depended on the iron content and to some extent the substrate condition.

The addition of approximately 5% iron into nickel led to a considerable solid solution hardening. The strength of these alloys as a function of grain size followed the classical Hall-Petch relationship. Nevertheless, an “inverse” Hall-Petch relation was observed within in the iron content region. The crossover grain size of about 10 nm is consistent with the previous results for Ni-Fe deposits using microhardness measurements [9,17,119,120]. In addition, the strength of deposited Ni-Fe alloys with similar grain size was dependent of the iron content. A maximum was measured at the iron content of approximately 20%.

CHAPTER 5
MECHANICAL PROPERTIES AND FRACTURE BEHAVIOR OF
NANOCRYSTALLINE NI-15%FE ALLOY

It is well known that the strength and ductility are two key mechanical properties for any load bearing applications. High strength or hardness has been reported for metallic nanocrystals. For FCC copper with a grain size larger than 100 nm [180,181], the results have been reported that their deformation behaviors and the larger tensile elongation were characteristic of those achieved in the case of conventional metals, which is in a good agreement with the theoretical prediction [41,42]. However, with regard to the FCC metals having the grain size less than 15 nm, the studies are mainly confined to compressive tests [21,31,114,125,182], and tensile results are quite limited. Available results show that the tensile elongation in nanocrystalline FCC metals is typically very low at room temperature [3,5,11,12]. It is interesting whether the nanostructured metals with such grain size level are inherently brittle. In addition, the mechanical behavior and the fracture manner are also little known when the grain size is less than 15 nm. In chapter 4, it has been identified that Ni-15%Fe deposits had a grain size of approximately 10 nm and low internal stress. Also, the texture of these deposits was negligible. As a result, this chapter is intended to study how the materials behave in Ni-15%Fe samples.

5.1 Deformation and Fracture Behavior of the Ni-15%Fe Alloy

5.1.1 Microstructure

TEM micrographs of as-deposited Ni-15%Fe samples are presented in Figure 5-1. The grain size distribution was relatively tight from 5 to 30 nm, as shown in Figures 5-1(a) and (b). High resolution TEM observations further confirmed that some grains (marked by arrows in Figure 5-2) are as small as approximately 4 nm. Based on measuring more than 700 grains on several dark field pictures, the mean grain size was calculated to be approximately 9 nm. The detailed grain size distribution for this alloy is plotted in Figure 5-1(d).

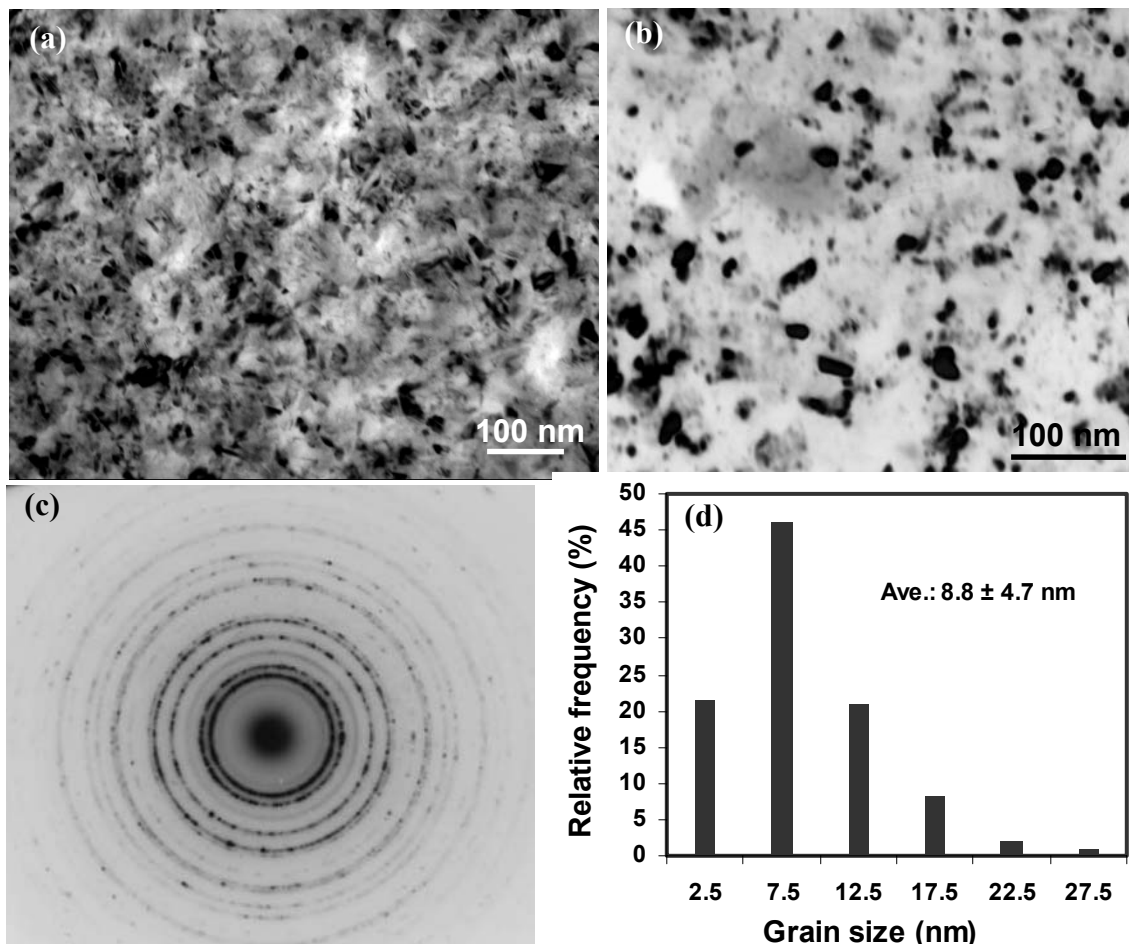


Figure 5-1. TEM images of (a) bright field, (b) dark field and (c) selected area diffraction pattern; (d) grain size distribution, inset number is the average grain size.

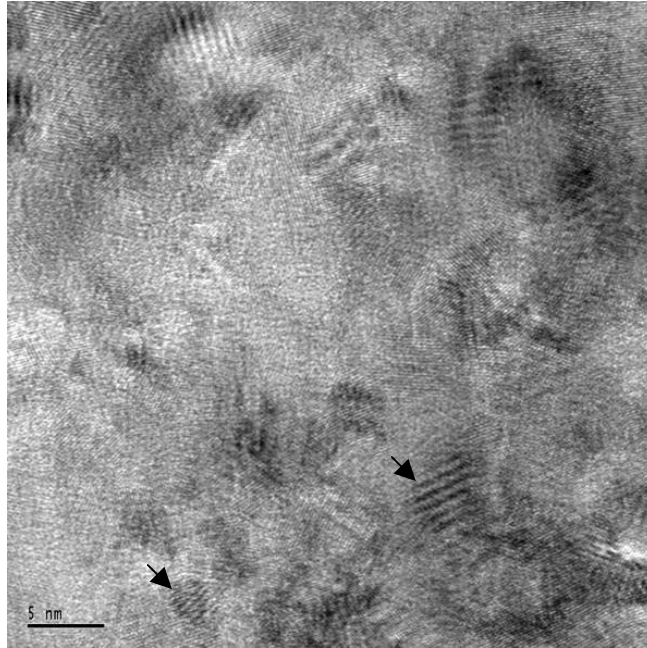


Figure 5-2. High resolution TEM picture of as-deposited Ni-15%Fe sample.

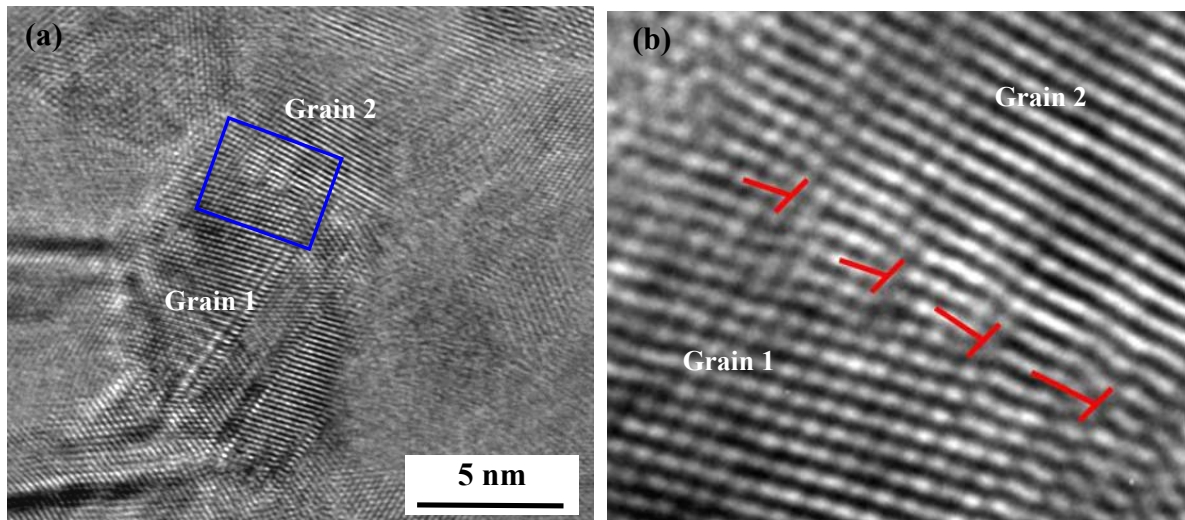


Figure 5-3. HRTEM pictures of (a) two adjacent grains and (b) four dislocations (red marks) sitting at grain boundary between grains 1 and 2.

Although the TEM micrographs indicate that the grain boundaries are primarily high angle boundaries, there are still some low angle grain boundaries, composed of dislocations. For example, Figure 5-3(b) displays the magnified image of marked area in Figure 5-3(a), where at least four dislocations (red marks) were observed along the grain boundary between grain 1 and grain 2.

5.1.2 Tensile Results

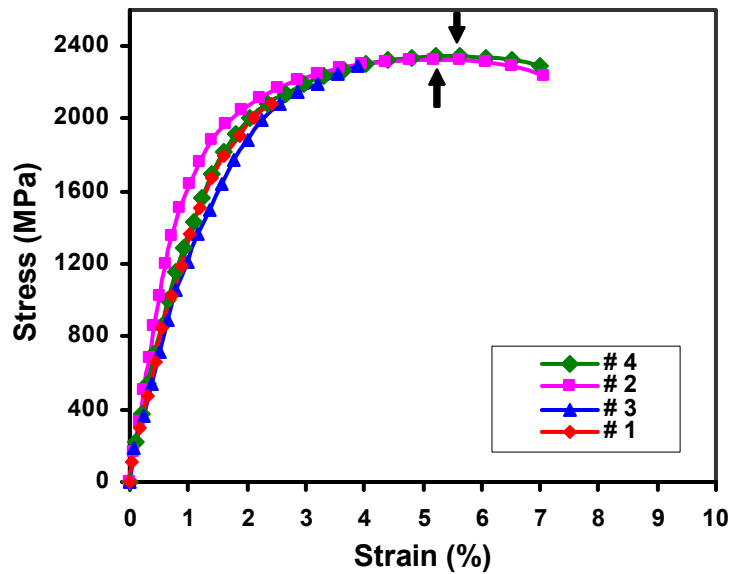


Figure 5-4. Engineering stress-strain curves of as-deposited Ni-15%Fe alloys.

Dog-bone shaped specimens were prepared with a width of 3 mm and a gauge length of 5 mm for the tensile experiments, which were conducted at a strain rate of $4.2 \times 10^{-3} s^{-1}$ at room temperature. The engineering stress-strain curves are plotted in Figure 5-4, where the upward and downward arrows denote the maximum strength point of curves 2 and 4, respectively. The tensile properties are summarized in Table 5-1. The results show that the as-deposited defect-free specimens had a strength as high as 2356 ± 30 MPa, which is nearly ten times higher than the tensile strength of a conventional FCC Ni-Fe alloy [183]. But it is impressive that the plastic elongation to failure at this level of

strength is as much as $5.8 \pm 0.2\%$. To the best of our knowledge, this is the first time to report a combination of such large tensile elongation and high tensile strength in a nanocrystalline FCC metal with a grain size below 10 nm. Previous studies demonstrated that the nanocrystalline nickel with an average grain size of approximately 20-30 nm shows only 2-3% plastic elongation [10,11], even no plastic deformation [12] at a strength level of 1400-1600 MPa.

Table 5-1. Tensile properties of as-deposited Ni-15%Fe alloys.

Sample #	Yield strength (MPa)	Tensile strength (MPa)	Plastic elong. (%)
2	1634	2326	6.0
4	1540	2386	5.6
1*	1572	2081	1.1
3*	1500	2280	2.1

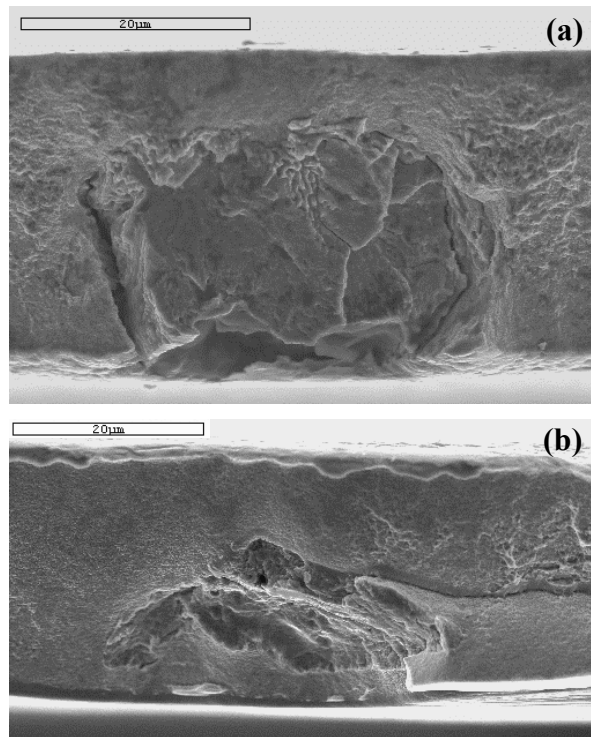
* containing defects.

On the basis of the Considère criterion ($d\sigma/d\varepsilon = \sigma$) the large uniform elongation (4.1%) of these samples is associated with their very high strain-hardening rates that persist as the deformation proceeds [184]. In coarse grained single-phase metals, the strength increases with strain because the dislocations become entangled and immobilized, and consequently they multiply to fulfill the applied deformation. However, such dislocation multiplication is not operative in nanocrystalline metals due to the small grain size. Computer simulation results indicate that most of the plastic deformation is accommodated at grain boundaries in FCC metals with less than 10 nm grain size [35,36]. At small grain sizes only emission and glide of individual dislocations occur. Therefore, the strain hardening rate is modeled as in composite materials [10,141], where the very small grains deform elastically (equivalent to a hard phase) while the larger

grains deform plastically via dislocation motion (equivalent to a soft phase). The incompatibility in deformation between the smaller and the larger grains creates internal stresses that escalate with strain and cause strain hardening. As stresses are increased, two competing relaxation mechanisms, grain boundary sliding and dislocation activity in the smaller grains, become operative. The latter mechanism is expected to result in a much faster reduction in the strain-hardening rate. When the grain boundary sliding is prevalent, the lowering of the local internal stresses reduces the probability of activating dislocations in the smaller grains. In addition, a recent model describes that the dislocations generated from grain boundaries also could glide and climb along the grain boundaries, resulting in the grain boundary sliding and rotational deformation, respectively [185]. It is therefore suggested that the continual strain hardening can be attributed to the continuous participation of smaller grains in the plastic deformation process via the grain boundary governed mechanism, i.e. grain boundary sliding and grain rotation.

As shown in Figure 5-4, samples #1 and #3 fractured in a premature manner (prior to achieving plastic instability) with plastic strains of 1.1% and 2.1%, respectively. Detailed fractography examinations revealed the existence of defects on the fracture surfaces of samples #1 and #3. Figure 5-5(a) illustrates one defect ($\sim 30 \mu\text{m}$ in size) located near the mid-section of sample #3. On the other hand, there were no detectable defects on the fracture surfaces of those specimens that exhibited necking behavior and large plastic strains. It is known that conventional ductile FCC metals such as nickel and copper are not notch sensitive. In other words, the strength of the notched sample at the maximum load is equal or larger than the tensile strength of the un-notched sample. In the

case of sample #3, however, the ratio of their individual maximum strength to that of specimen #2 or #4 is less than 1. Therefore, the defects in samples #3 act as notches and hence increase the local stresses. This behavior suggests that crack propagation in this material is stress-controlled. A further decrease of plastic elongation in sample #1 is accordingly attributed to the two observed defects on the fracture surface; one was in middle section and the other one located near the edge, as seen in Figures 5-5(b) and (c), respectively. The notch sensitivity of the nanocrystalline Ni-15%Fe samples is indicative of their low toughness, which is contrary to the tendency obtained in coarse-grained FCC materials where toughness increases with a reduction in grain size [123]. Based on the above discussion, it is anticipated that nanocrystalline metals with very small grain sizes will exhibit reasonable tensile elongation if they can be made without defects.



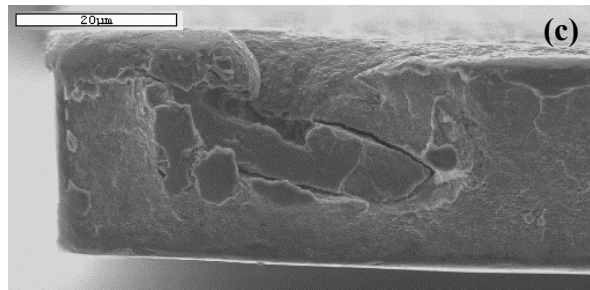


Figure 5-5. Defects on the fracture surfaces of (a) #3, (b) and (c) #1 samples.

Figure 5-6(a) shows a HRTEM picture of a deformed sample (after tensile test).

Figure 5-6(b) is the magnified image of the square area in the Figure 5-6(a), where one dislocation (red line) was observed within a grain of approximately 17 nm, implying possible dislocation activities in such small grains. This observation is consistent with the *in-situ* TEM study [63]. In addition, the grain boundary dislocations (Figure 5-3) could also participate in the plastic process during loading.

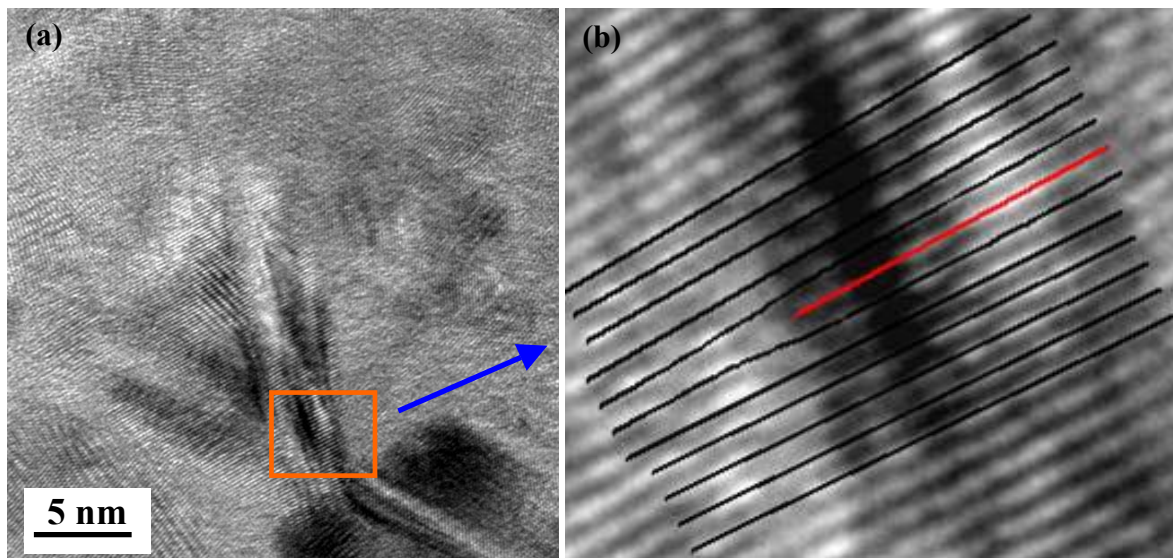


Figure 5-6. High resolution TEM micrograph of a deformed sample; (a) a 17 nm grain in the center; (b) amplified image of square region in (a) indicating the existence of a dislocation (red line).

Therefore, it is likely that the large plastic deformation achieved in the Ni-15%Fe alloy arises from a combination of dislocation activity and grain boundary sliding, but it is very difficult to determine the degree of contribution from each mechanism.

Mechanical twinning via partial dislocation emission from grain boundaries may also play a role in the plastic deformation of nanocrystalline metals, which has been confirmed by the computer simulation [24] and the experimental observations [27,143] on nanostructured aluminum. In nanocrystalline copper, twins and stacking faults in nanocrystalline copper were also found to be formed via partial dislocation emissions from grain boundaries [28]. However, it is difficult to distinguish the mechanical twins from processed twins introduced during sample preparation. Besides, it is not possible to evaluate the quantitative contribution from twinning in TEM. In order to characterize the role of twinning, more works need to be done by applying other techniques, such as neutron scattering, in bulk nanocrystalline materials.

It is noted that the stress-strain curve (Figure 5-4) of the as-deposited samples without defects (no noticeable defects were found on the fracture surface) exhibits a maximum indicative of plastic instability, which is a characteristic of the tensile behavior of the conventional ductile metals. Generally, the instability observed as the load drop can be due to these phenomena: (i) necking; (ii) the formation of shear bands; and (iii) microcracking. In order to make clear what causes the load drop, one specimen (#5) was partially loaded to approximately 2237 MPa (point A), prior to the maximum strength (2360 MPa, green arrow), as shown in Figure 5-7. The observations in the SEM revealed no deformation bands and microcracks. This sample was reloaded up to fracture and no defects like those shown in Figure 5-5 were detected. No. 6 specimen was loaded until

point B, which is slightly beyond maximum strength (orange arrow), but before the onset of fracture. Also, no microcracking or deformation bands were observed. As a result, the possibility that microcracking and the shear bands caused plastic instability is excluded.

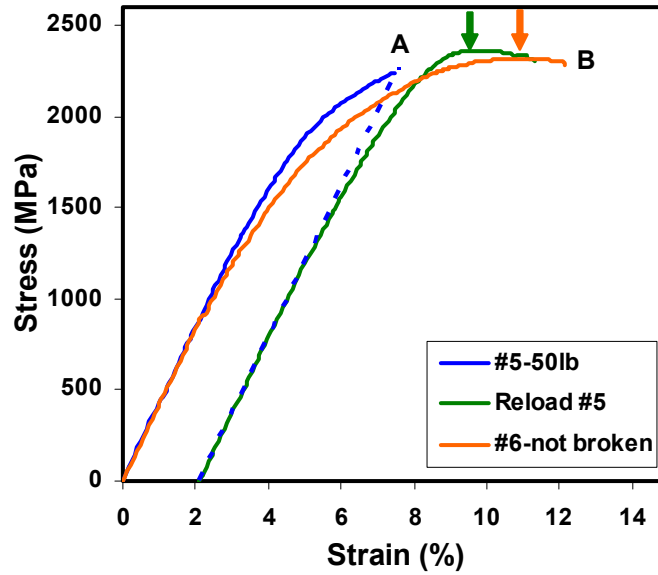


Figure 5-7. Engineering stress-strain curves of partially loaded Ni-15%Fe specimens.

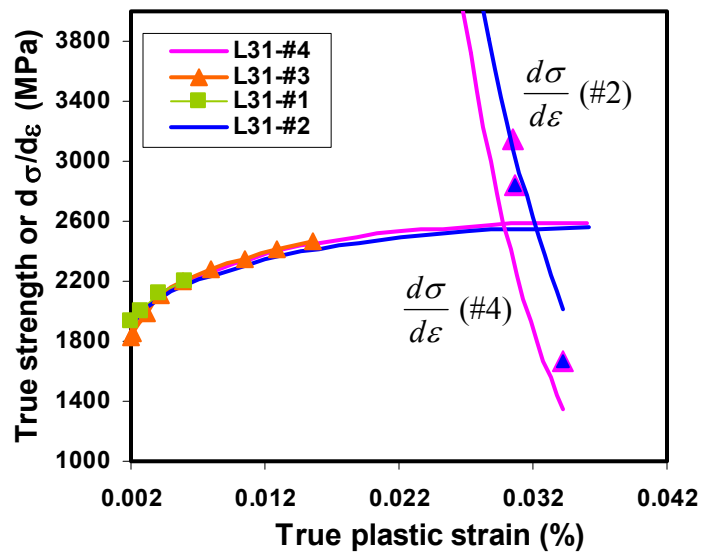


Figure 5-8. True stress-strain and strain hardening rate-strain curves.

Figure 5-8 presents the true stress (σ)-true strain (ϵ) and strain hardening rate ($d\sigma/d\epsilon$)-true strain (ϵ) curves. It is found that, for samples #2 and #4, their true stress-strain and $d\sigma/d\epsilon - \epsilon$ curves all intersected approximately at the maximum tensile stress. At this point, the increase of strength caused by strain hardening cannot compensate for the decrease in the cross section area (Considère criterion: $d\sigma/d\epsilon \leq \sigma$ [34]). Therefore, it is concluded that the load drop is due to the conventional necking of the samples.

5.1.3 Fracture Behavior

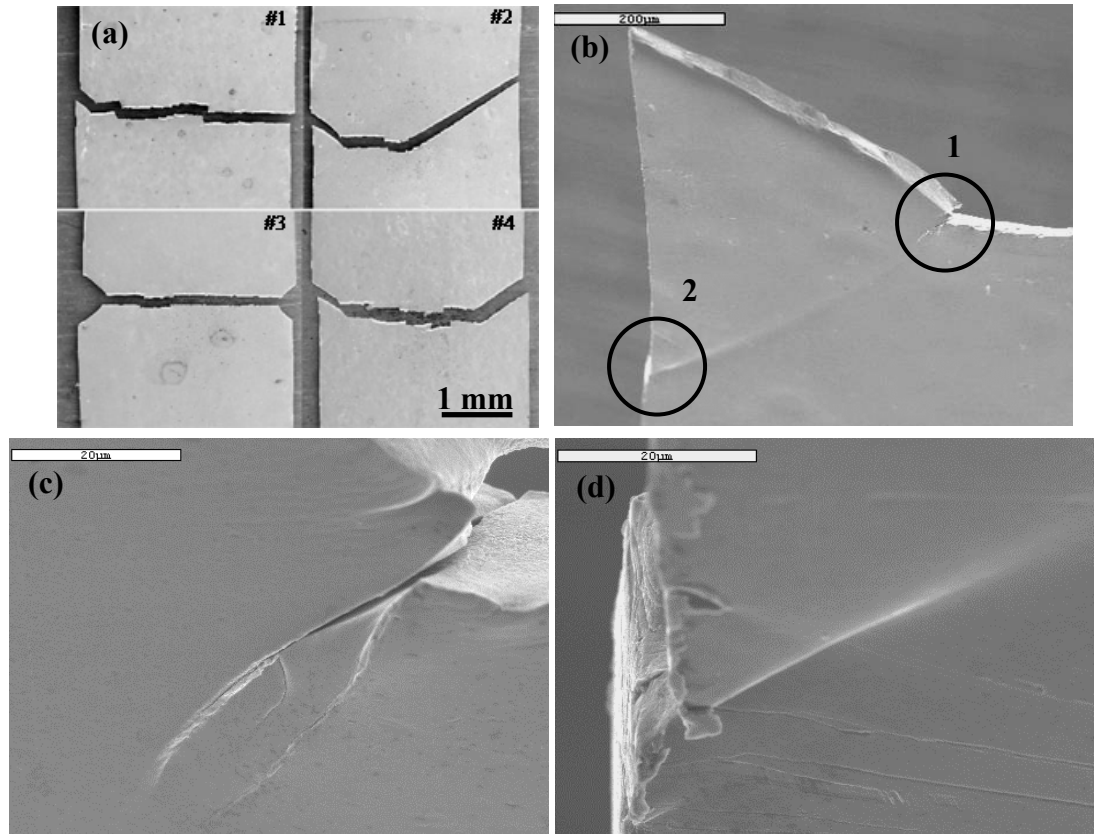


Figure 5-9. Fracture geometries. (a) fracture scenario of all four specimens; (b) shear lip in sample #4; (c) and (d) magnified images of circled regions 1 and 2 in (b), respectively.

Figure 5-9(a) demonstrates the fracture geometry of four samples. In general, the specimens failed with a flat mid-section and slanted fracture paths near the edges. Figure 5-9(b) presents the magnified image of the slanted region with an obvious shear trace in sample #4, which is representative of the defect-free samples. The enlarged picture of region 1 in Figure 5-9(b) is displayed in Figure 5-9(c), where the crack propagation and the displacement were examined along the shear direction. The advance of the crack along the shear trace was also observed in region 2, whose amplified micrograph is elucidated in Figure 5-9(d).

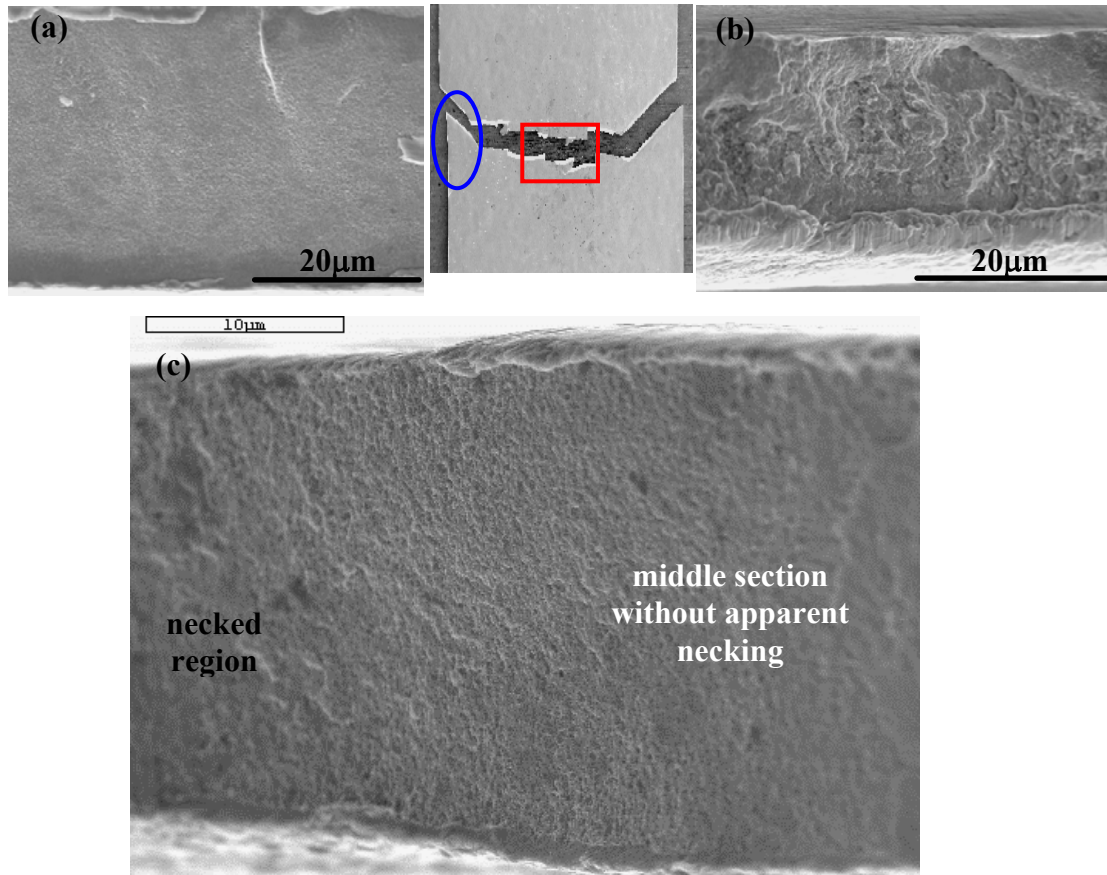


Figure 5-10. SEM photographs of the fracture surfaces. (a) and (b) taken from the mid-section and slanted regions, respectively; (c) shows a change from non-necked to necked portion.

Figure 5-10 illustrates the fracture surfaces in sample #4. Figure 5-10(a), taken from the flat mid-section (squared region), shows that the fracture surface is quite smooth with no noticeable area reduction, whereas the slanted portion, magnified from circled area, is noticeably necked with a rough fracture surface (Figure 5-10(b)). Figure 5-10(c) illustrates a manifest transition from the middle section with no notable necking into the evidently necked region. Detailed analysis exposes that the fracture surface exhibited microvoid structure regardless of in the flat or slant regions. Their respective high magnification images are displayed in Figures 5-11. It is found that the size of these microvoids is several times of the grain size. Similar phenomena have been observed in other nanocrystalline FCC metals [18,135]. The microvoid size with the scale of several grain sizes was suggested by computer simulation to be because of the development of shear planes around several grains [137]. A comparison of Figures 5-11(a) and (b) discloses that the voids were shallower in the flat areas, which is perhaps due to the different stress states. During the fracture process, the middle section had a plane-strain state, while the stress state was plane-stress condition near the edges.

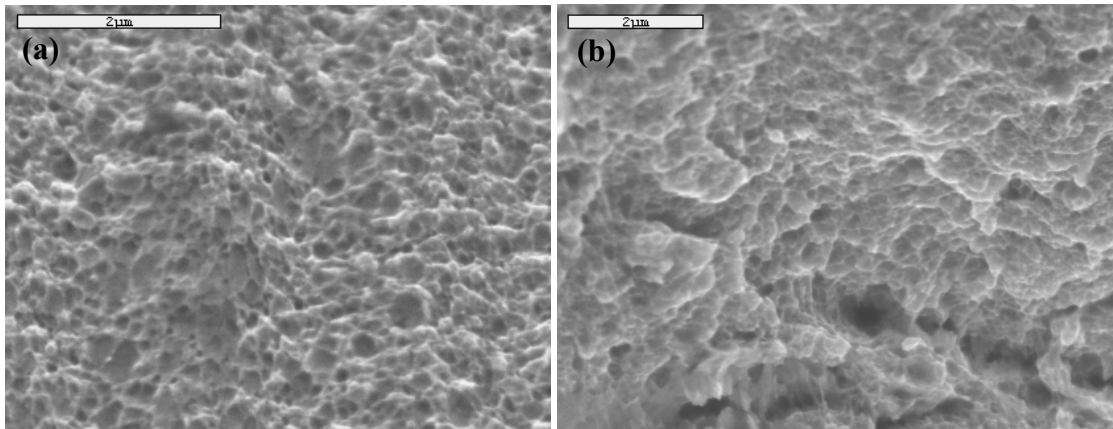


Figure 5-11. SEM images of the fracture surface showing (a) the middle section and (b) the slanted portion at high magnifications.

Although the fracture surface demonstrates the shallow microvoid structure, TEM observations using both dark field and bright field techniques revealed that the fracture within the shallow voids is in fact intergranular, as shown in Figure 5-12, where the crack propagated along the grain boundaries marked by arrows. This is in a good agreement with the computer simulation results of pure nickel that the fracture mode is intergranular as the grain size is reduced below 15 nm [138]. It is worth noting that, to date, no experimental results in bulk samples are available to witness the intergranular fracture in nanocrystalline materials.

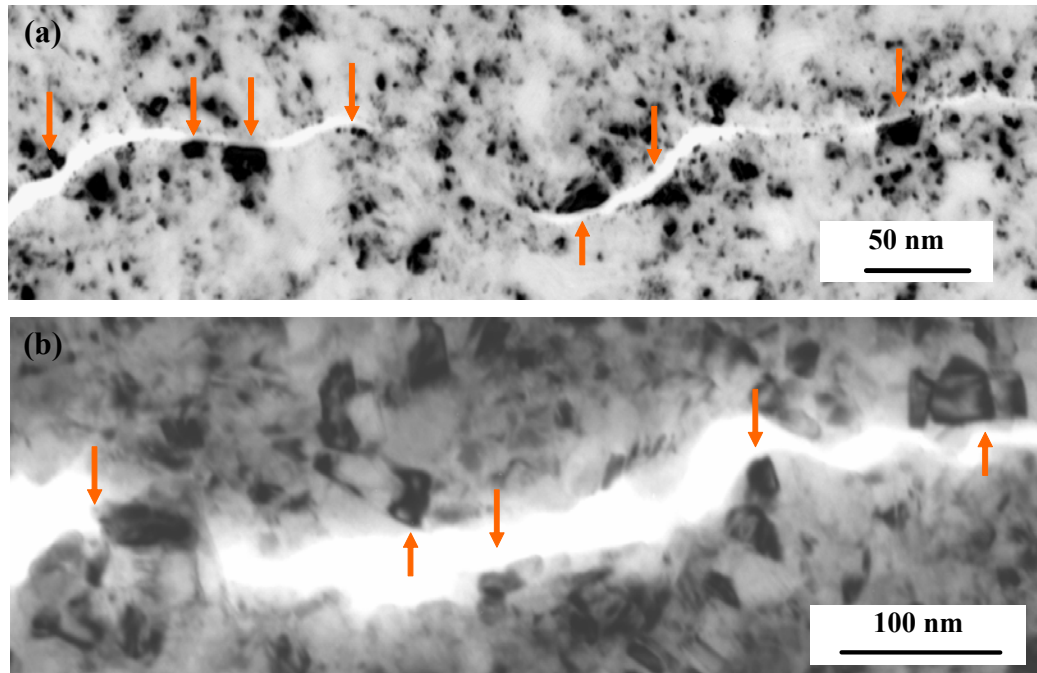


Figure 5-12. TEM micrographs of (a) dark field and (b) bright field, showing the intergranular fracture.

Once again, it is noted that, when talking about fracture behaviors, only defect-free samples are concerned. The issues related to the defects will be considered in the discussion section. Figure 5-13(a) shows that, within the narrow region close to the fracture surface, there are many deformation bands (localized deformation region marked

by arrows) and microcracks in the middle section, which are approximately parallel to the main fracture surface. For instance, in this figure, marks 'e' and 'f' denote two microcracks. It should be pointed out that no such deformation bands were observed in the areas far away from the fracture surface. This is in contrast to the results reported for nanocrystalline copper, where shear bands, oriented about 60 degrees relative to the tensile axis, were observed [186]. It is also of interests that there were no microcracks found near the fracture surface within the slanted section, but the apparent shear localization was observed, as shown in Figure 5-13(b). Considering that no shear bands were observed in the samples loaded close to the fracture point, the processes of microcracking and shear banding may be cooperative.

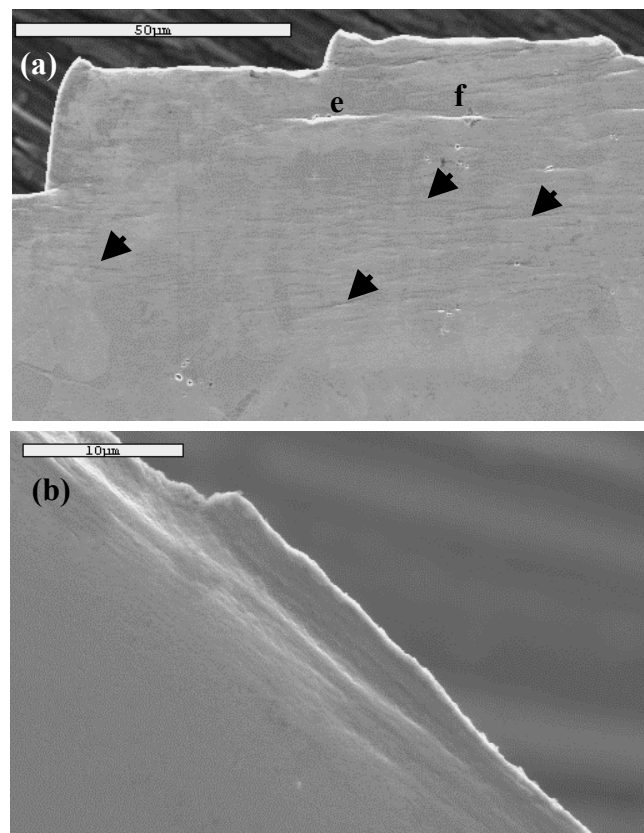


Figure 5-13. SEM observations of (a) middle section and (b) slant area.

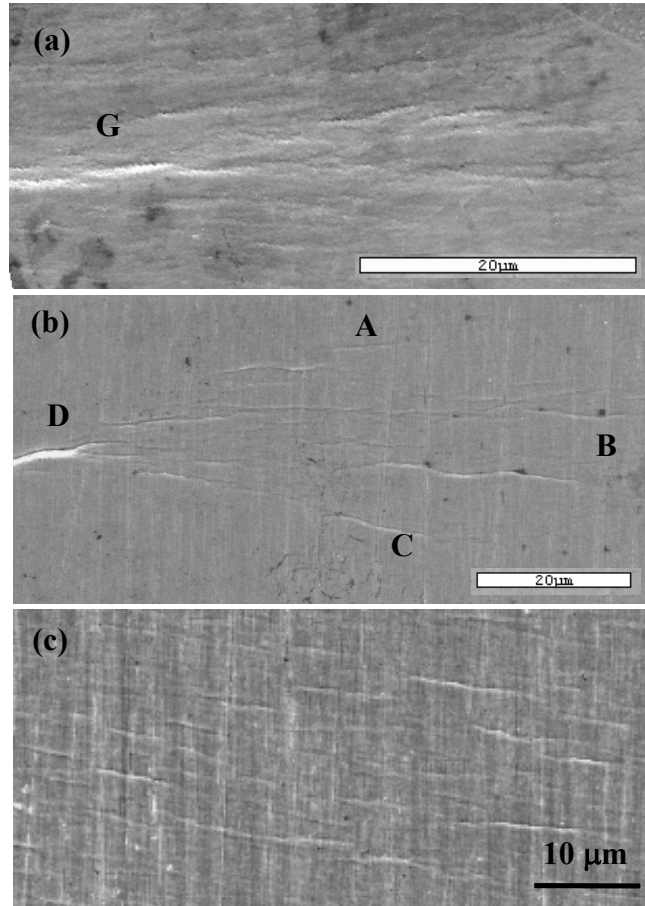
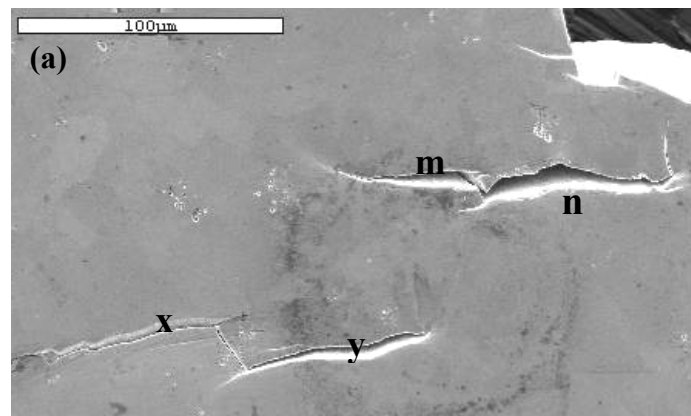


Figure 5-14. Notable plastic zones ahead of microcracks in (a) as-deposited and (b) annealed samples; (c) microcracking and deformation bands.

Figure 5-14(a) shows a noticeable plastic zone consisting of several deformation bands ahead of the crack tip 'G'. Figure 5-14(b) is another example of plastic zone ahead of microcrack 'D'. The plastic zone denotes one region which deforms plastically, for example the region 'ABCD' in Figure 5-14(b). Accordingly, with continuously straining, the crack will proceed forward, leaving deformation bands on both sides of the fracture surface. On the other hand, microcracks can nucleate and propagate along the pre-existing deformation bands, for example the microcracks 'e' and 'f' shown in Figure 5-14(a). One of the tensile specimens failed near the shoulder. However, microcracking and plastic localization were found in the mid-gage length as shown in Figure 5-14(c). These

pre-existing deformation bands could have developed by the formation of microcracks, which have not yet emerged to the surface. In this instance, the stress near the shoulder of the specimen was higher than that in the microcracked and necked region.

Detailed characterizations have exposed that the development of the stable microcracks was prior to final failure. When two adjacent cracks approach close enough, they may be connected together by cracking, as displayed in Figure 5-15(a), where the cracks 'm' and 'n' as well as 'x' and 'y' are linked by breaking the ligaments. Figure 5-15(b) was pictured within the similar location on the opposite side. It is found that these microcracks for example 'm' and 'n' penetrated through the thickness. The joining of such adjacent microcracks usually leaves a step behind. This is in a good agreement with the actual observation that there were many steps like 'EF' on the fracture surface, as presented in Figure 5-15(c), which was overlooked from the top of the fracture surface. The observation of such steps is clearer from side surface (Figure 5-15(d)). It is also observed that, on occasion, many steps developed within the shear lip section, as illustrated in Figure 5-15(e). These observations further confirm that the stable advancement of microcracking before final fracture.



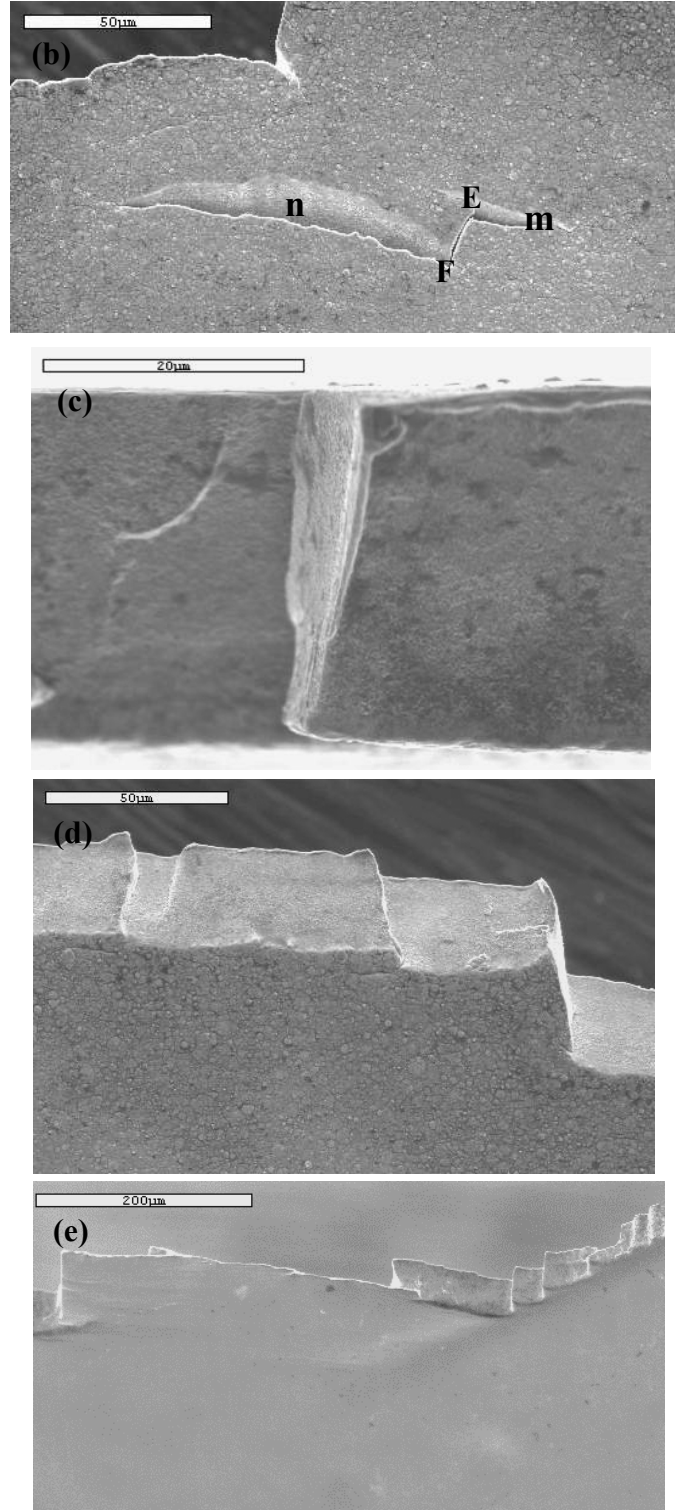


Figure 5-15. Connecting between two adjacent microcracks on the (a) substrate side and (b) the solution side; (c) and (d) the steps on the fracture surfaces.

5.2 Discussion

It is noteworthy that the tensile strength (2.4 GPa) and elongation (5.8%) of defect-free nanocrystalline Ni-15%Fe alloy (~9 nm) are comparable with those of commercial ultra-high strength alloys. For example quenched and tempered 300M steel with a strength of 2.34 GPa shows a tensile elongation of 6% [187]. The toughness of the Ni-15%Fe alloy can be estimated by considering the sample #3, where a defect (~30 μm) is located near the mid-section. Under uniform tension, the stress intensity factor for a center-cracked plate with a small crack is estimated by [188]:

$$K_I = \sigma\sqrt{\pi a} \quad (5-1)$$

Here, σ is the fracture stress and $2a$ is the crack length. Substituting the fracture stress (2280 MPa) and a (15 μm) into the above equation, the approximate K value is 16 $\text{MPa}\cdot\text{m}^{1/2}$, which is reasonable for many structural applications. For example this value is close to the range of high strength aluminum alloys' toughness, which is approximately 20-30 $\text{MPa}\cdot\text{m}^{1/2}$ [188]. Upon the comparison of the nanocrystalline Ni-15%Fe alloy and commercial high strength materials, it is concluded that the defect-free (i.e., absence of micron size voids and impurities) nanocrystalline metals are not "unusual" in respect to their mechanical properties and fracture behavior. Present study provides evidences for the potential possibility of nanocrystalline materials' applications based on conventional approaches.

Although the necking was decided to happen based on stress-strain curves, there is no considerable necking observed on the fracture surface in the middle section. This is probably associated to the limited area reduction on the fracture surface. The localized necking within the slant region is because the plane-stress condition at the later stage of

the fracture, which is not the cause of the load drop. In spite of the microvoid structure on the fracture surface, TEM observations reveal that the fracture is in fact the intergranular mode.

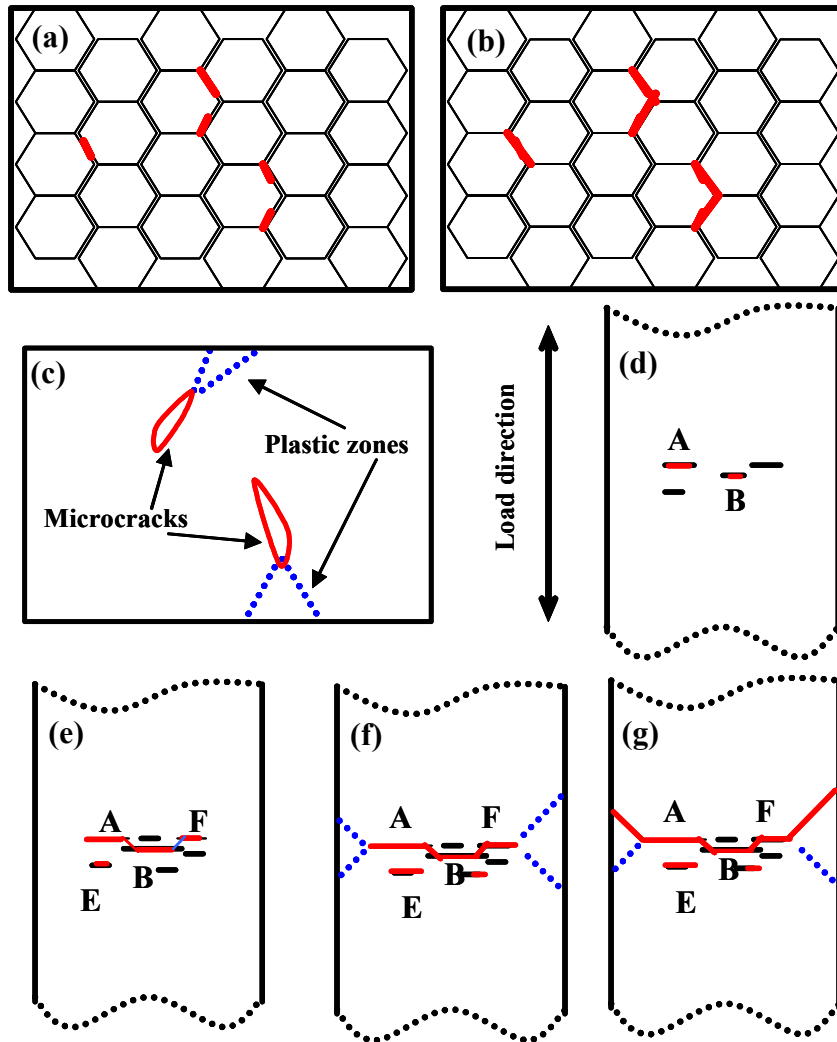


Figure 5-16. Schematic diagram describing the fracture procedures in defect-free nanocrystalline metals. Here, red marks are cracks and blue ones refer to either the plastic zone or the shear localization.

Fractographic analyses point to the fact that the fracture of the nanocrystalline Ni-15%Fe alloy is stress controlled, although the appearance is void like. We propose that the failure of defect-free tensile specimens begins with plastic localization (necking). It has been reported that the existence of nano-sized pores in nanocrystalline materials is

the intrinsic properties [72]. In the case of electrodeposited nanocrystalline materials, the preexisting nanovoids probably result from the hydrogen evolution or the space left as a consequence of grain joining during electrodeposition. Also, nanocracks can form at grain boundaries or triple points because of severe strain incompatibility in these sites [138]. Figure 5-16(a) demonstrates the cross-section of one tensile sample, where red lines refer to the nanopores or nanocracks sitting at the grain boundaries. These nanovoids or -cracks are the preferred sites for microcrack initiation. As soon as necking happens, a triaxial state of stress is introduced. Because of the maximum constraint in the center of the specimen, the new nanocracks nucleate at these pre-existing nanopores and then grow by connecting each other, as seen in Figure 5-16(b). As these nanocracks grow into microcracks and the plastic zone of these microcracks arrives on the surface, they appear as micro-size shear bands (Figures 5-16(c) and (d)). In Figure 5-16(d), the black and red lines denote the deformation band and microcrack, respectively. The corresponding experimental observations are presented in Figures 5-13 and 5-14. With continuous straining, when the microcracks such as “A” and “B” in Figure 5-16(d) propagate close enough, they adjoin together in the way of Figure 5-15(a). The schematic is displayed in Figure 5-16(e). Similar process is repeated until the main crack extends outward and approaches the edges. At this time, the plane stress condition along the width of the sample results in the strain localization, extensive necking and slanted fracture behavior. The shear localization (dotted blue lines) with approximately 45 degrees relative to the tensile axial occurs (Figure 5-16(f)). Furthermore, in the slanted segment, localization precedes cracking and no secondary microcracks were found (Figure 5-13(b)). Finally, the sample fails along the shear localization, as shown in Figure

5-16(g). Sometimes, the shear lips break off along both plastic localization directions at the moment of complete failure, as seen in sample #3 of Figure 5-9(a). A comparison of sample #3 and #4 in Figure 5-9(a) suggests that there is no apparent relationship between the elongation and the fracture geometry, confirming that the decreased plastic elongation in sample #3 is due to the presence of the defect.

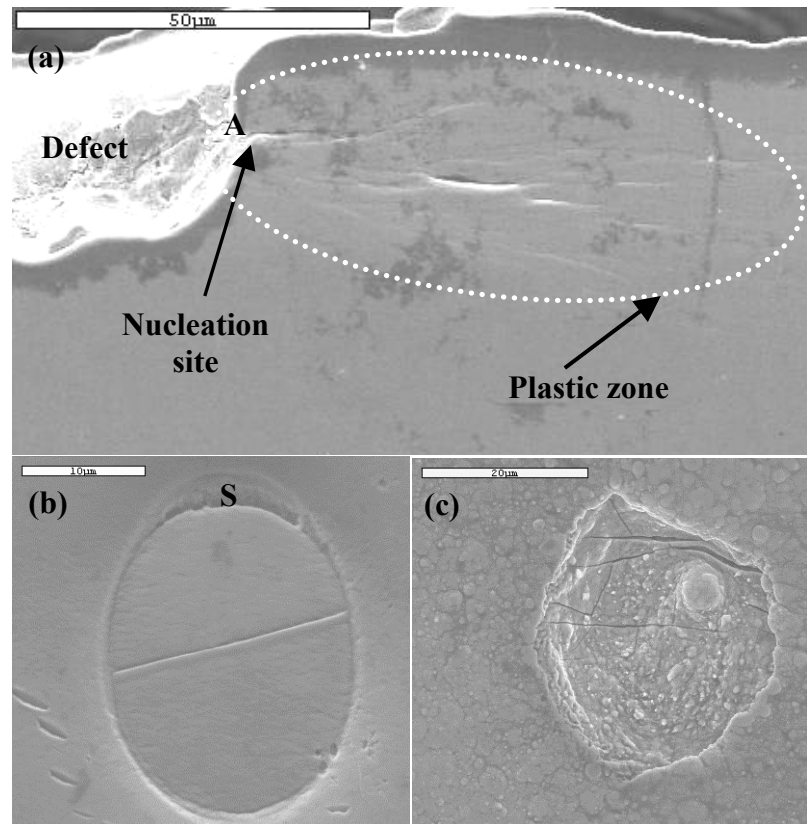


Figure 5-17. Microcrack nucleation at the defects. (a) cracking at defect; (b) detaching of defect from sample, resulting in microcrack 's'; (c) cracking developed inside defect.

With the presence of defects, for example in samples #1 and #3, the necking is no longer necessary for crack nucleation. The triaxial stress state and the stress intensity at the defect satisfy the requirement for crack nucleation. For example, Figure 5-17(a) elucidates that, as the stress intensity was high enough, the crack started to nucleate at the point A of the defect and an obvious plastic zone developed ahead the crack tip 'A'.

Sometimes, it is found that the cracking happened by detaching between defects and sample (Figure 5-17(b)) or breaking the defect itself firstly (Figure 5-17(c)), where the vertical direction is parallel to the tensile axial. In addition, detailed examinations reveal that the fracture features on the fracture surface and side surface in sample #3 and #1 are same as those in terms of defect-free samples #2 and #4. Let's look back at the Figure 5-9(a). In the case of sample #3, because the defect was in the middle, its fracture geometry is expected to be similar to those of #2 and #4 specimens. With regard to sample #1, the flat right end is due to one defect sitting at the right end, as presented in Figure 5-5.

5.3 Summary

As-deposited Ni-15%Fe alloy had a narrow grain size distribution and the average grain size was as small as approximately 9 nm. Tensile tests conducted at room temperature showed that the plastic elongation and the tensile strength are as high as 6% and 2.4 GPa, respectively. In contrast to the reported results, the achieved tensile ductility, as the grain size is less than 15 nm, is much more improved. In addition, it is found that the load drop was caused by necking. A comparison of present results with the ultra-high strength steel as well as the calculation of nanocrystalline Ni-15%Fe alloy's toughness reveal that the nanocrystalline materials are probably comparable with the conventional materials with super-high strength. That is, nanocrystalline metals are not intrinsically brittle and the nanocrystalline metals have potential structural applications. The limited tensile and the premature fracture were proven to be due to the presence of defects; and the nanocrystalline FCC metals are notch sensitive, which is different from the coarse-grained FCC metals.

Detailed fractographic examinations disclose the fact that the failure of defect-free tensile specimens begins with plastic localization-necking and the fracture is stress

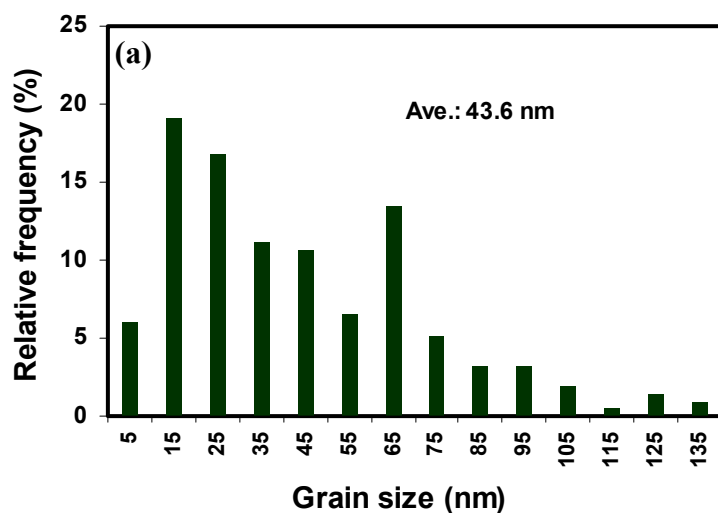
controlled. Furthermore, the tensile fracture of defect-free sample is governed by stable propagation of microcracks. It is also found that the development of microcracks and the formation of deformation bands are cooperative. With the existence of big defects, the crack preferably nucleated at these locations because of the weakness or stress intensity.

CHAPTER 6 THE INFLUENCE OF GRAIN SIZE ON MECHANICAL BEHAVIOR

It is extrapolated that, on the basis of the Hall-Petch relationship [110,111], the strength of metals increases with a reduction in the grain size. Nevertheless, it has been mentioned in chapter 2 that a reverse Hall-Petch has been observed experimentally and theoretically in many results [9,35,121]. That is, as the grain size is decreased below a critical value, the strength decreases with further a reduction in the grain size. This critical value, also called as the strongest grain size [122], is believed to be approximately 10-20 nm for FCC metals and of course depends on the nature of the material. The microhardness results for an electrodeposited Ni-20%Fe alloy suggest a critical value of 12 nm [9]. For pure nickel, based on the dislocation pile-up mechanism [3], this crossover value is approximately 10 nm. Across this critical grain size, it has been accepted that there exists a transition in the deformation mechanism. Computer simulations on Al [41] and Cu [42] whose strongest grain sizes are about 18 nm and 14 nm, respectively, have revealed that the deformation is mediated by dislocation activity when the grain size is larger than this critical value, whereas the grain boundary assisted deformation is dominant at smaller grain sizes. As a consequence, a change in the deformation and fracture behaviors is expected as the grain size is reduced below the crossover value. In this chapter, we performed tensile and nanoindentation tests on nanocrystalline pure nickel, Ni-6%Fe and Ni-15%Fe alloys to characterize the dependence of the deformation and fracture behaviors on the grain size.

6.1 Results and Discussion

As discussed in the chapter 4, addition of alloying element helps decrease the grain size. Thus, the deposits with different grain sizes were fabricated by adding different amounts of alloying element. The Ni-15%Fe deposit used in this chapter had a grain size of approximately 10 nm measured by XRD technique. Upon the discussion in chapter 4, it is reasonable to assume that this deposit's grain size is the same as that of the deposit used in the last chapter, i.e., about 9 nm, which was evaluated by TEM. Figure 6-1 demonstrates the grain size distributions of pure nickel and Ni-6%Fe alloy based on measuring more than 150 grains on several TEM dark field pictures. The average grain size for pure nickel and Ni-6%Fe alloy were approximately 44 and 53 nm, respectively, so that the nickel and Ni-6%Fe alloy fall into the large grain size range, i.e. larger than the critical grain size for these materials. Ni-15%Fe alloy is among the small grain size regime, i.e. smaller than the critical grain size for this material.



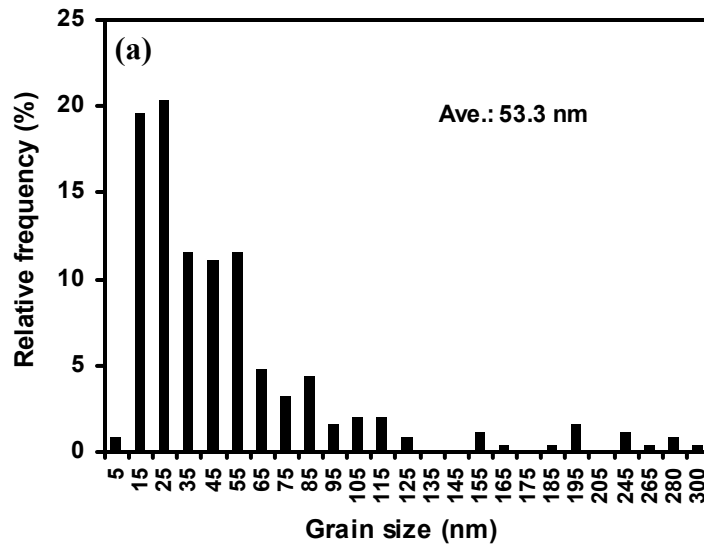


Figure 6-1. Grain size distributions in electrodeposited (a) nickel and (b) Ni-6%Fe samples.

6.1.1 Tensile Results

The tensile tests were carried out within a strain rate range of 2×10^{-4} s⁻¹ to 5×10^{-6} s⁻¹ at room temperature. Figure 6-2 displays the engineering stress-strain curves of nanocrystalline Ni, Ni-6%Fe and Ni-15%Fe alloys and their tensile properties are summarized in Table 6-1. In general, the strengths of these three nanocrystalline materials are several times higher than their respective coarse-grained counterparts. For example, the tensile strength of pure nickel (53 nm) was measured at 1061 MPa, while it is only 317 MPa in the case of typical coarse-grained nickel. Although Ni-6%Fe alloy's grain size is slightly larger than that of pure nickel, it is of interest that its strength is not lower than nickel's strength. In addition, the initial strain-hardening rate in Ni-6%Fe alloys is obviously higher than in pure nickel. This is relevant to the effect of alloying elements. The addition of alloying elements usually decreases the stacking fault energy and thus increases the strength [189]. In addition, recent computer simulations regarding nanocrystalline FCC metals reveal that not only the further emission of partial dislocations could be blocked but also the emitted partial dislocations on different slip

planes could interact with each other in the low stacking fault energy nanocrystals [23], which implies an increase in the strain-hardening rate. For the Ni-15%Fe alloy, however, the strength and strain-hardening rate are much higher than those of pure nickel and Ni-6%Fe alloy, which is in most part due to the difference in their grain size. This observation is consistent with the previous results – the smaller the grain size, the higher the strain-hardening rate [10]. The deformation of nanocrystalline materials is suggested to be similar to composite materials, i.e. the level of the plastic strain varies among grains with different sizes, and at a given stress level there exist a fraction of grains which deform only elastically [10,141]. In this case, the internal stresses that develop owing to the strain incompatibility among various grain sizes cause strain hardening. Therefore, the higher strain-hardening rate of the Ni-15% alloy is attributed to a higher level of strain incompatibility due to the presence of finer grains. Of course, further lowering of the stacking fault energy by further additions of iron may also contribute to the high strain-hardening rate. As revealed by simulation studies, the degree of grain boundary deformation as well as dislocation activity increases with increasing the applied strain [42]; these processes relieve the internal stresses and then reduce the strain-hardening rate with increasing strain.

One may question why the Ni-15%Fe alloy's strength is relatively higher than those of pure nickel and Ni-6%Fe alloy since the softening has been predicted by computer simulation as the grain size is about 9 nm. The reason is that the Ni-15%Fe alloy's grain size is close to the critical value on the side of the low grain size, whereas the grain sizes of nickel and Ni-6%Fe alloy are quite far away from the strongest grain

size and within the large grain size regime. That is, their distances to the critical grain size are different.

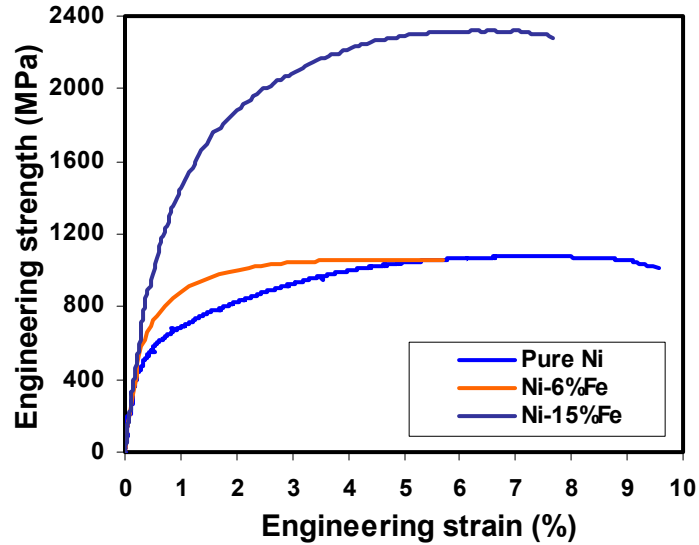


Figure 6-2. Tensile stress-strain curves of Ni, Ni-6%Fe and Ni-15%Fe alloys.

Table 6-1. Tensile results for Ni, Ni-6%Fe and Ni-15%Fe alloys.

Sample	$S_{0.2}$ (MPa)	S_{UTS} (MPa)	e_p^t (%)	e^{post} (%)
Ni-15%Fe 9 nm	1225	2320	6.7	1.1
	1610	2361	5.9	1.6
Ni-6%Fe 53 nm	752	1061	5.2	1.0
Ni 44 nm	544	1076	9.1	2.5
	446	1088	8.5	2.1

Both Figure 6-2 and Table 6-1 indicate that all samples showed post-uniform elongation, and their tensile elongations are comparable with pure nickel showing the highest tensile elongation. Figure 6-3 presents a comparison of the previous studies and present results considering the relationship between the grain size and the tensile strain in

FCC metals, where the dotted line is the separation of current and reported results. Figure 6-3(b) shows the results only for electrodeposited Ni and Ni-Fe alloys. The scatter in the data is perhaps due to the difference in the sample production techniques. In addition, processing techniques did not affect the change tendency in the tensile elongation with the grain size significantly. It is very explicit that, as grain size is less than 60 nm, the documented tensile elongation is usually lower than 4%. Impressively, current results show a significant improvement to the reported values. For instance, the tensile elongation of nanostructured Ni with 44 nm grain size is found to be as high as 8-9%. The improved elongation is attributed to the lack of large defects and the high quality of the deposits. Recent computer simulation has revealed the dislocation pile-ups within a 49 nm grain of Cu [42]. In addition, the dislocation activities have also been directly observed in the study of a 30 nm Ni using *in-situ* TEM technique [135]. Therefore, it is expected that the nickel and Ni-6%Fe samples studied here deformed plastically with a dislocation-governed mechanism. That is, the plasticity and the strain hardening come predominantly from the dislocation activities. Of course, grain boundary sliding may also play a role because of the gradual transition in the deformation mechanism with the grain size [41,42]. Figure 6-4 confirms that there are numerous dislocations in a deformed pure nickel sample, where circled region contains a dislocation pile-up. As similarly seen in chapter 5, it is of surprise that the Ni-15%Fe alloy with an average grain size of 9 nm also showed impressive tensile elongation of 6-7%. This experimental finding confirms the simulation predictions of enhanced plasticity via grain boundary-based deformation mechanisms in nanocrystals with less than the critical grain size [35,190]. The detailed discussion concerning the plasticity of Ni-15%Fe alloy has been stated in the last chapter.

In conclusion, plasticity was achieved during tensile testing of both types of nanocrystalline materials, although the mechanism of deformation varied from a dislocation-governed mechanism in Ni to a grain boundary based mechanism in the Ni-15%Fe alloy.

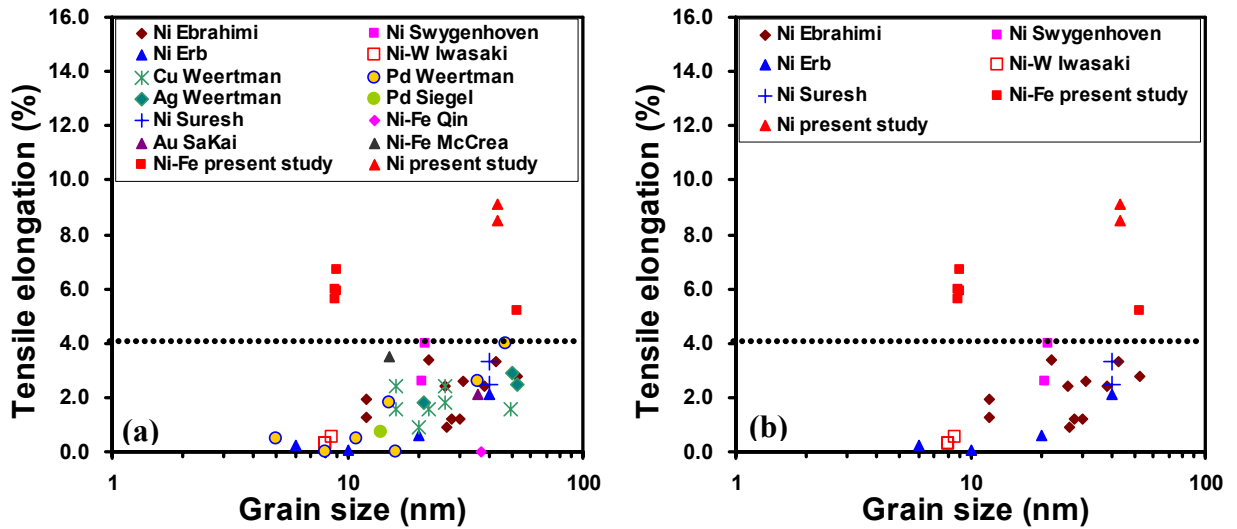


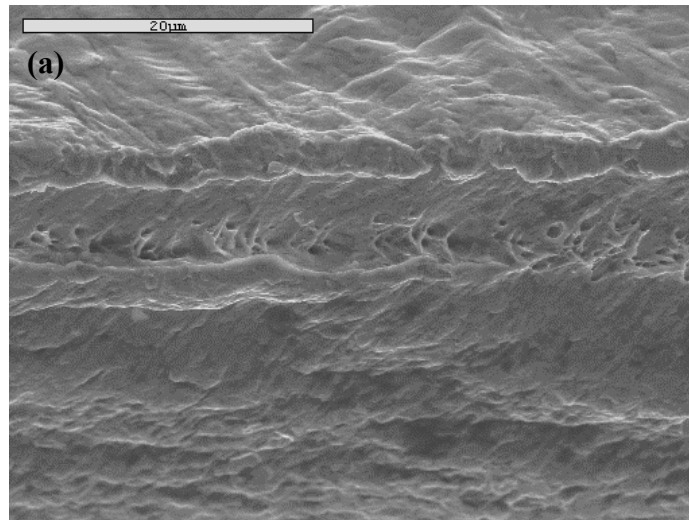
Figure 6-3. Tensile elongation in FCC metals as a function of the grain size.



Figure 6-4. TEM micrograph of a deformed nickel sample.

6.1.2 Fractography

In chapter 5, it was shown that the Ni-15%Fe alloy fractured without considerable necking and the fracture surface exhibited shallow microvoid structure, as seen in Figure 5-11. In the case of pure nickel with a grain size larger than 40 nm, however, Figure 6-5(a) illustrates the extensive reduction in area, characteristic of a ductile material. Consistently, the fracture surface displayed deep microvoids as shown in Figure 6-5(b). Similar fracture features were also obtained in the Ni-6%Fe samples, as seen in Figure 6-6(a). Furthermore, Ni-6%Fe samples even fractured in a knife-edge manner (Figure 6-6(b)). These observations strongly suggest that pure nickel and Ni-6%Fe specimens with the grain size beyond the critical value fractured by the microvoid coalescence mechanism, similar to the conventional ductile FCC metals [34,39]. Note that the failure of samples, independent of their grain size level, all began with necking.



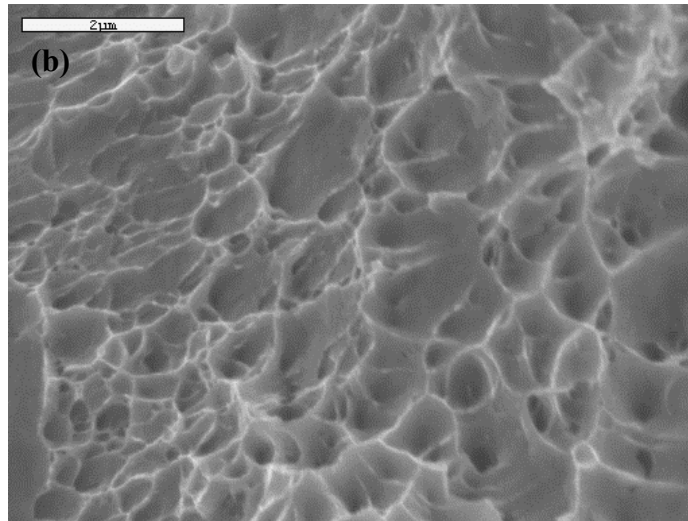


Figure 6-5. Fracture surfaces of pure nickel at (a) low and (b) high magnifications.

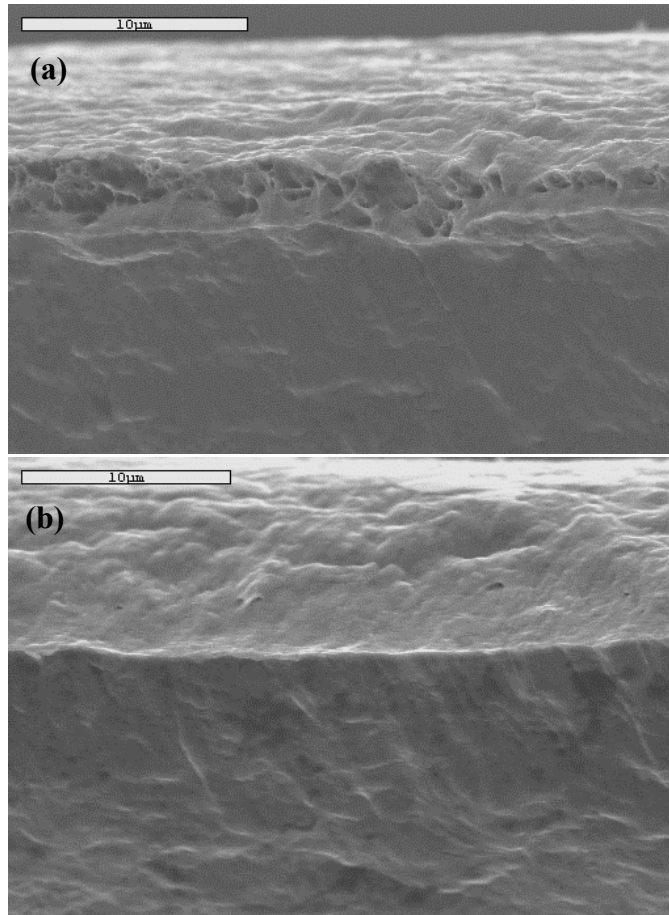


Figure 6-6. SEM micrographs showing (a) deep dimples and (b) knife-edge behavior on the fracture surface of the Ni-6%Fe samples.

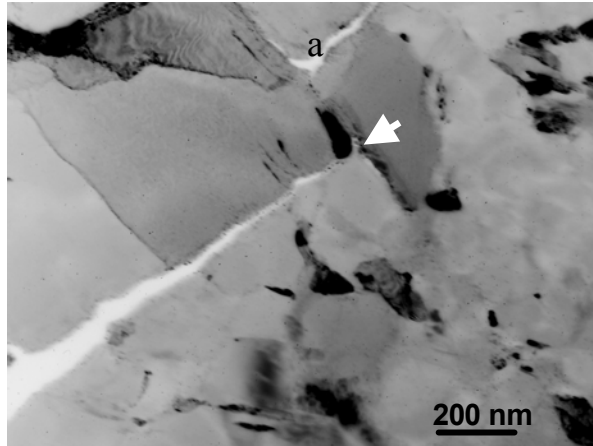
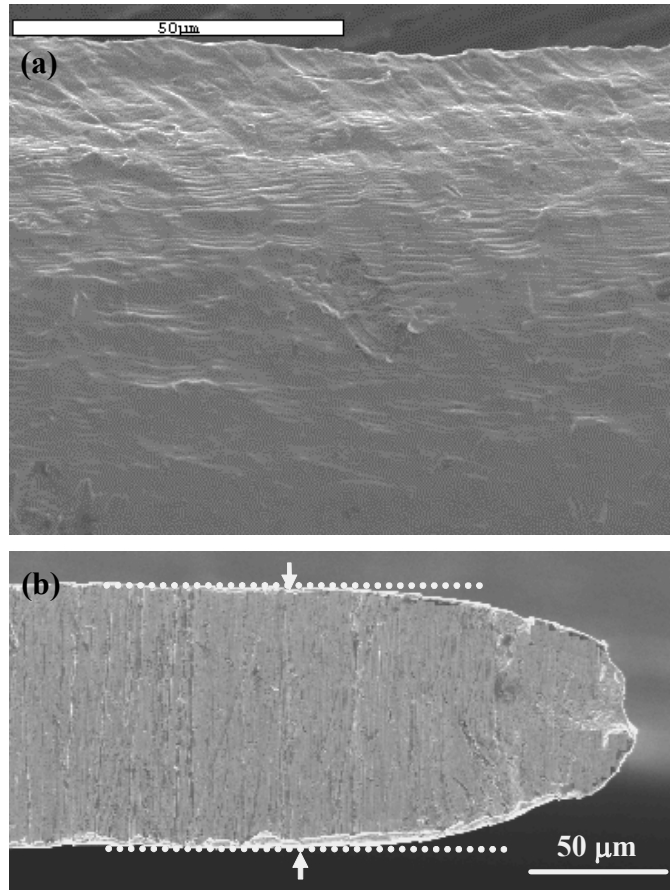


Figure 6-7. TEM dark filed image of pure nickel shows the mixture of intergranular and intragranular fractures.

Figure 6-7 presents the crack advancement in nanocrystalline nickel, where the main crack, propagated intragranularly, stopped at the grain boundary marked by a white arrow; then microcrack ‘a’ nucleated and propagated along the grain boundary. This observation suggests that the fracture behavior is a mixture of intergranular and intragranular manner in nanocrystalline nickel with a grain size of 44 nm. However, for Ni-15%Fe samples with a grain size of about 9 nm, the fracture was predominately intergranular manner, as seen in Figure 5-13.

Figure 6-8(a) shows that many deformation bands were also observed in the vicinity of the fracture surface of the pure nickel samples, similar to the observation made in Ni-15%Fe samples. However, no microcracking was detected in the case of pure nickel samples. It is worth noting that such deformation bands were only found in the areas near the fracture surface. The length of the region where deformation bands were detected was about 90 μm . Figure 6-8(b) presents the SEM photographs across the thickness of a broken specimen, where the arrows mark the beginning of plastic localization or necking. It is found that the necking length is approximately 120 μm ,

which is comparable to the scale of the deformation-band region. It is of importance that similar observations were made in the Ni-6%Fe samples. For example, Figure 6-8(c) shows the deformation bands near the fracture surface, where the deformation band region (the distance from fracture surface to the point having no deformation band) was measured at approximately 53 μm . The diffuse necking length was about 65 μm (Figure 6-8(d)), which is also comparable to the size of the deformation band region. Such observations in both nickel and Ni-6%Fe alloy insinuate that the deformation bands only developed within the diffuse necking regime. However, in terms of the Ni-15%Fe alloy, the deformation bands are associated with the plastic zone ahead of the microcracks.



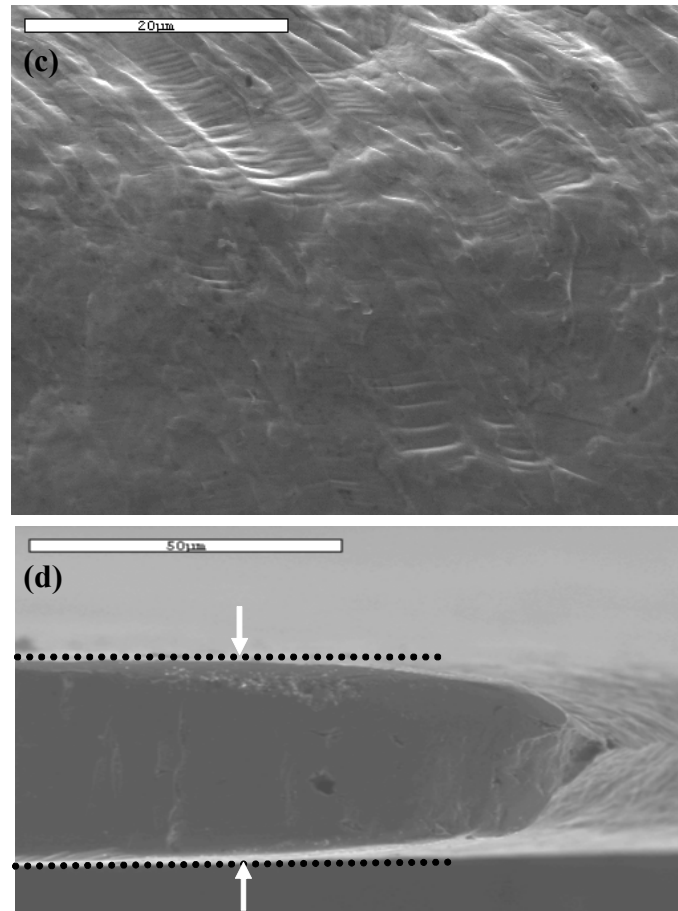


Figure 6-8. SEM images show the deformation bands in (a) pure nickel and (c) Ni-6%Fe alloy as well as the necking geometries of (b) pure nickel and (d) Ni-6%Fe alloy, respectively.

Figure 6-9 re-plots the engineering stress-strain curves for the Ni-15%Fe and Ni-6%Fe samples with and without defects. As discussed in the last chapter, the Ni-15%Fe samples exhibited notch sensitivity and fractured in a premature behavior when defects existed. Moreover, Figure 5-18 provided the evidences that the crack primarily nucleated at the defects due to the stress intensification. Interestingly, for the Ni-6%Fe alloy, the severe necking still happened even with the presence of defects, as displayed in Figure 6-10. The difference between defect-free and flawed samples is that the latter immediately broke with a reduced uniform elongation as soon as necking occurred, i.e., limited post uniform elongation; the former showed notable post-uniform strain, as shown in Figure

6-9. A comparison of the Ni-15%Fe and the Ni-6%Fe alloys proposes that the sensitivity to the notch decreases with increasing the grain size, consistent with the statement in the last chapter.

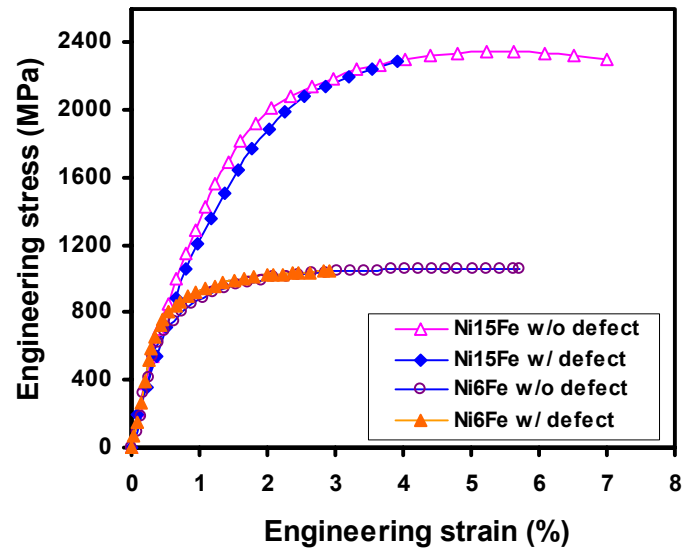


Figure 6-9. Stress-strain curves of Ni-6%Fe and Ni-15%Fe alloys with and without defects.

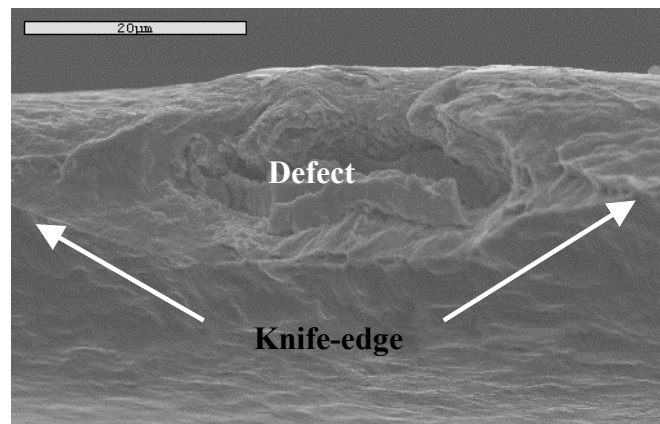


Figure 6-10. Fracture surface of one Ni-6%Fe sample with a defect.

6.1.3 Nanoindentation Results

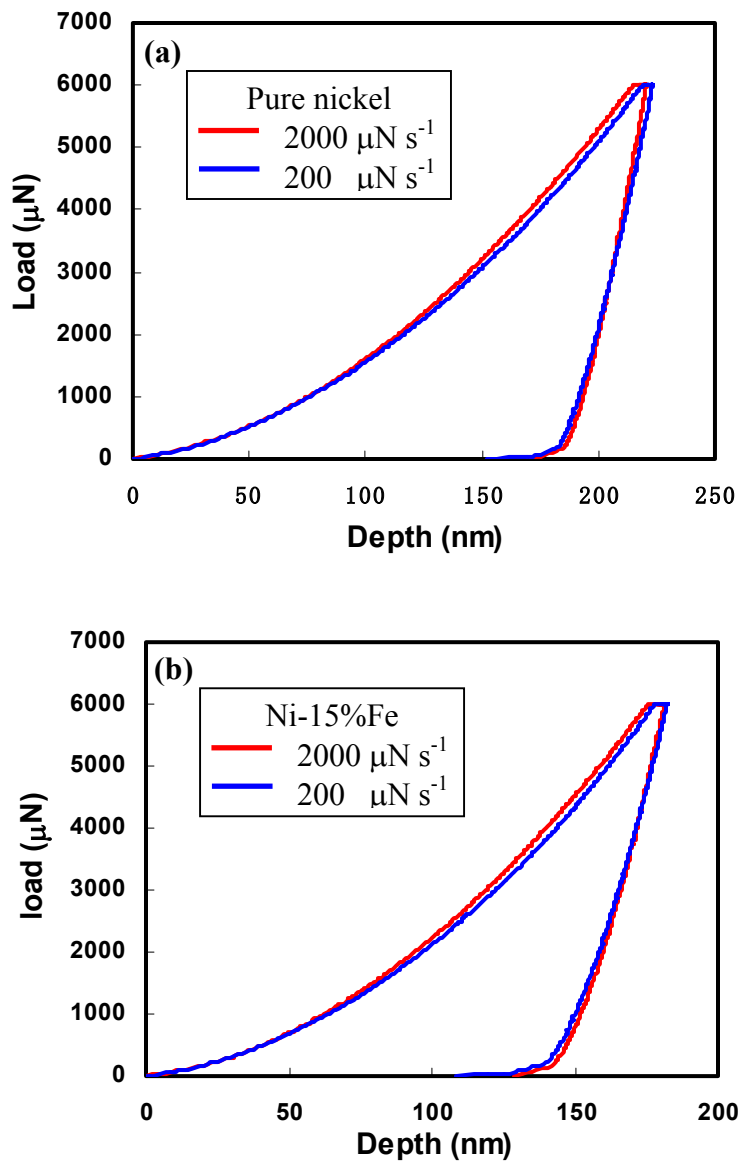


Figure 6-11. Load-displacement ($P-h$) curves of (a) pure nickel and (b) Ni-15%Fe alloy at two different load rates. Each curve is an average of five indents at given load rate.

Figure 6-11 presents the load-displacement curves conducted on pure nickel and Ni-15%Fe samples at two loading rates, respectively. It is evident that the indentation depth of about 215 nm in the case of pure nickel is much larger than that of approximately 178 nm for the Ni-15%Fe alloy obtained at the same load of 6000 μN .

This indicates that the Ni-15%Fe alloy is harder than pure nickel, which has been well characterized in tensile results. More importantly, both materials exhibited rate sensitivity, i.e., the strength increased with increasing the loading rate. Such strain rate sensitivity in nanocrystalline materials has been observed in previous studies [16,132]. However, careful examination reveals that the degree of loading rate sensitivity is similar in both materials, which contradicts the published results in that the enhanced strain-rate sensitivity with decreasing the grain size was obtained in nickel [132], where a model of grain boundary affected zone was suggested. Computer simulation results have shown that, in fact, both dislocation activity and grain boundary sliding are involved during plastic deformation [23,35,36,40-42], although there exists a transition in the deformation mechanism with the grain size [41,42]. Concerning the Ni-15%Fe alloy with a grain size less than 10 nm, it is believed that the grain boundary sliding, which is gradually involved with increasing the applied stress [42], plays a dominant role. As a result, the stress-driven diffusion is beneficial to the strain-rate sensitivity. For pure nickel, it has been proven by TEM observations that the dislocation activity is the major contribution to the plastic deformation even when the grain size is approximately 30 nm [135]. Accordingly, the dependence of the dislocation velocity on the strain rate is seemingly responsible for the observed rate sensitivity in pure nickel. In addition, due to the addition of iron into nickel, both the grain boundary composition and the stacking fault energy are changed. Thus, the dislocation emission and the grain boundary shifting may become more difficult. This is probably why no increased strain-rate sensitivity with decreasing the grain size was detected in the present study. In order to examine the strain-rate

sensitivity's dependence on the grain size, the experiments are better to be performed on the same materials with different grain size scales.

6.2 Summary

The tensile and constant load rate tests were conducted on electrodeposited nanocrystalline pure nickel, Ni-6%Fe and Ni-15%Fe alloys. The results demonstrate that single-phase nanocrystalline FCC metals are intrinsically ductile and their failure begins with necking. Additionally, their ductility and fracture manners are grain size dependent. For Ni and Ni-6%Fe alloy, whose grain sizes are beyond the crossover value, the plastic deformation is controlled by dislocation activity and the material shows large reduction in area, typical of conventional FCC metals. A comparison of pure and Ni-6%Fe alloy suggests that the addition of alloying element increase the strain-hardening rate and the strength. The deformation bands developed within the diffuse necking areas. However, in the case of Ni-15% alloy with a grain size below its critical value, where the strain-hardening rate and the strength are very high due to the small grain size and the alloying effect. The plastic deformation is dominated by the grain boundary sliding, and the ductility as evaluated by the reduction in area is very limited and extensive microcracking precedes the final failure. In FCC metals, the notch sensitivity seems to decrease with increasing the grain size. On the other hand, regardless of the grain size, both pure nickel and Ni-15%Fe alloy showed strain-rate sensitivity, which is contradict with the reported results for pure nickel [132]. This is possibly related to the change in the grain boundary composition and the decrease in the stacking fault energy resulted from alloying element addition.

CHAPTER 7 THE EFFECT OF LOW TEMPERATURE ANNEALING ON MECHANICAL PROPERTIES

It has been well known that the grain boundaries occupy a considerable volume fraction in the nanocrystalline materials, in particular as the grain size is less than 15 nm. At such small grain size level, the grain boundary sliding is believed to be the dominant deformation mechanism. Thus, the grain boundary plays an important role in deformation of nanocrystalline materials. In the past, most if not all studies emphasized the influence of the grain boundary volume fraction on the mechanical properties and the deformation behavior by varying the grain size [22,23,35-39,41,42,132]. The results concerning the role of the grain boundary state on the mechanical properties, specially in the aspect of experiment, are quite limited. It is the purpose of this chapter to evaluate the effect of the grain boundary state on the mechanical properties via low temperature annealing.

7.1 Experimental Results

7.1.1 Microstructure

In this study, the Ni-15%Fe deposit was used. The as-deposited samples were heat treated at 523 K for 90 min in argon atmosphere. Figure 7-1 presents the microstructures of as-deposited (AD) and annealed (AN) specimens, which were cut from the same deposit. It is clear that, besides the growth of few grains, there are no significant changes in the microstructure after low temperature heat treatment. The grain growth occurred in an abnormal manner. For example, one grain marked by the white arrow in Figure 7-1(b) grew to approximately 75 nm, while most grains remained unchanged in size or slightly

grew. The TEM dark field images further confirmed such abnormal grain growth, as demonstrated in Figure 7-2, where the insets are their respective selected area diffraction patterns. These observations are consistent with those in the case of pure nickel, which was annealed at 497 K for 75 min [45].

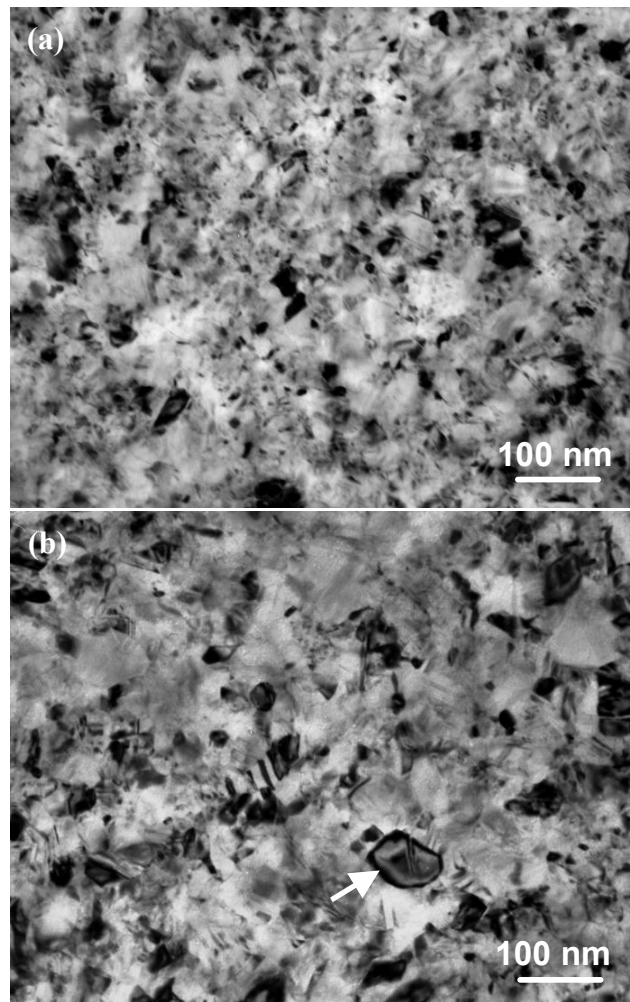


Figure 7-1. TEM bright field micrographs of (a) as-deposited and (b) annealed Ni-15%Fe specimens.

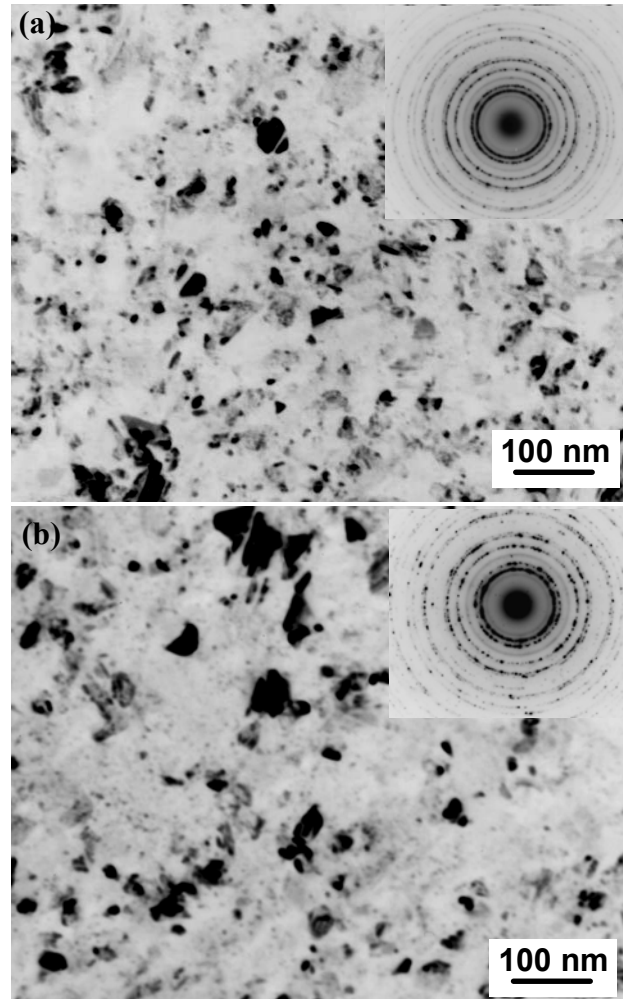


Figure 7-2. TEM dark field images of (a) as-deposited and (b) annealed Ni-15%Fe specimens. Insets denote the selected area diffraction patterns.

Figure 7-3 plots the grain size distribution based on measuring 726 and 539 grains on several TEM dark field images for the as-deposited and annealed specimens, respectively. A comparison of Figures 7-3(a) and (b) reveals that, within the grain size range of less than 30 nm, the grain size distributions in both cases are similar; the difference is that, in the annealed sample, there are several large grains. This observation once again confirms the abnormal grain growth. The average grain size is 8.8 and 11.1 nm for as-deposited and annealed specimens, respectively, which are consistent with the corresponding values of 10 and 15 nm measured by the XRD line broadening method.

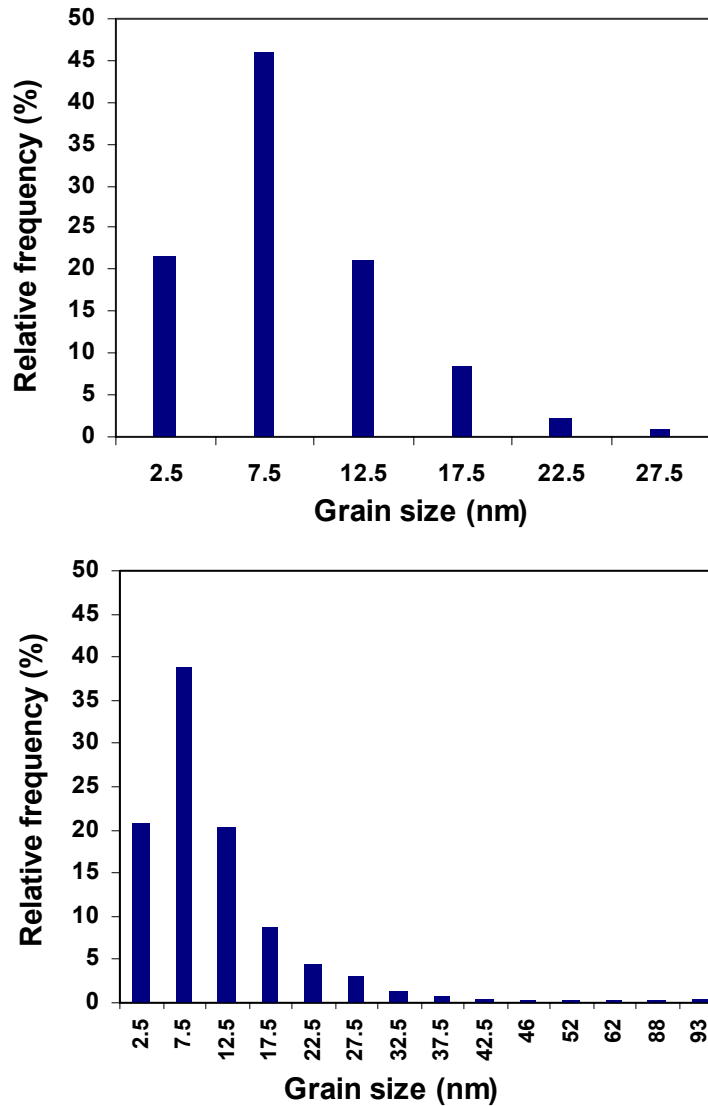


Figure 7-3. Grain size distribution of (a) as-deposited and (b) annealed samples.

7.1.2 Tensile Results

Figure 7-4 illustrates the tensile engineering stress-strain curves for as-deposited and annealed Ni-15%Fe samples, where each curve is representative of at least two tests. The results are presented in Table 7-1. As can be seen in both Figure 7-4 and Table 7-1, in spite of the increase in the grain size, annealing at 523 K raised the yield strength at 0.2% offset noticeably from 1502 ± 163 MPa to 1746 ± 66 MPa, whereas decreased the tensile elongation considerably, from 6.1% to 1.7%. It is worthy of pointing out that, in

the case of annealed specimens, also, the stress-strain curves show a maximum i.e., plastic instability preceded fracture. Moreover, SEM examinations of the fracture surface of the annealed samples did not reveal the presence of any micrometer size defect. The increase in the strength and the loss of tensile elongation in the annealed sample are in good agreement with the theoretical predictions [128], where the different degrees of grain boundary order were created by the computer simulation to mimic the as-deposited and annealed samples. The results show that the samples with relaxed boundaries had a higher strength [128]. It is also of interest that the initial strain-hardening rate increased after annealing, as seen in Figure 7-4.

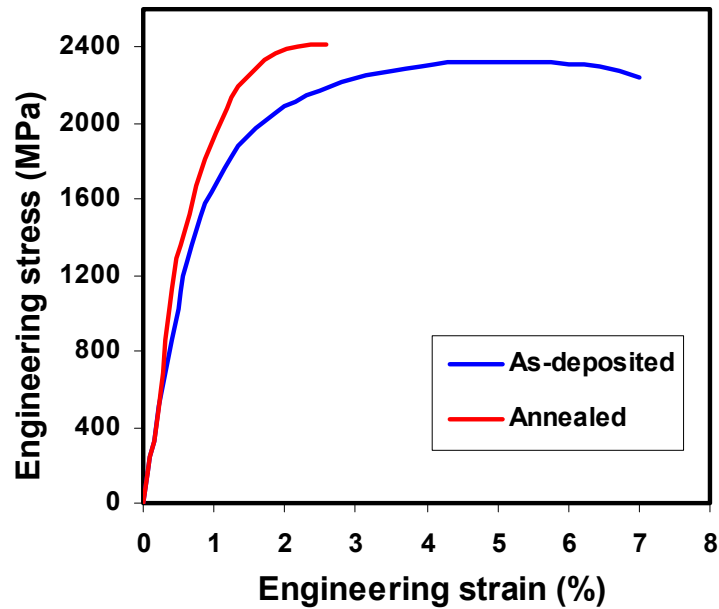


Figure 7-4. Tensile stress-strain curves of as-deposited and annealed Ni-15%Fe samples.

Table 7-1. A summary of the tensile results.

Sample	Yield strength (MPa)	Tensile strength (MPa)	Plastic elongation (%)
As-deposited	1634	2326	6.0
	1540	2386	5.6
	1225	2320	6.7
	1610	2361	5.9
Annealed	1812	2417	1.7
	1680	2230	1.65

7.1.3 Constant Load Rate Indentation

Figure 7-5 displays the load-displacement curves obtained from the as-deposited and the annealed specimens. In both cases, two different load rates were applied and each curve is the average of five indents. Firstly, it was found that the indentation depth was around 178 nm at maximum load of 6000 μN for the as-deposited samples, whereas the indentation depth was decreased to approximately 168 nm for the annealed specimens at the same load level, which indicates that the hardness increased after annealing. This finding is in agreement with the tensile results, as shown in both Figure 7-4 and Table 7-1. When applying the constant load rate tests, the maximum load was kept constantly for the specific time period. The constant load holding period can be assumed to be equivalent to creep test. It was found that the displacement was recognizably smaller in the annealed sample than the value achieved in the as-deposited case, implying less relaxation in the former. The most important observation in Figure 7-5 is that the as-deposited samples exhibited an apparent load-rate sensitivity, i.e., with decreasing the load rate, a larger indentation depth was achieved at the same load level, as seen in Figure 7-5(a). However, Figure 7-5(b) elucidates that no detectable difference was observed

between the two different applied load rates. In other words, annealed samples showed rate independent plastic flow within the currently used load rate range.

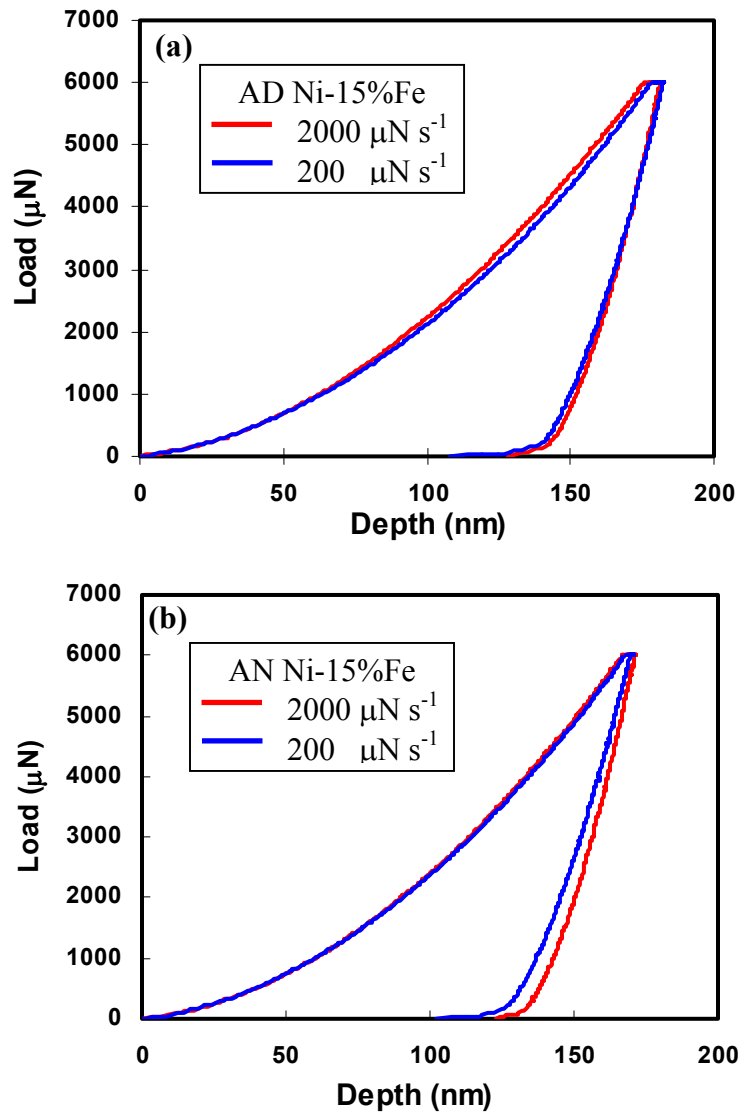


Figure 7-5. Load-displacement (P-h) curves for (a) as-deposited and (b) annealed Ni-15%Fe samples.

7.2 Discussion

Figure 7-6 illustrates the grain boundary between grains 1 and 2 in an electrodeposited Ni-Fe alloy. It is clear that the grain boundary is atomistically sharp and the crystallinity is maintained up to the grain boundary, indicating that the grain boundary in nanocrystalline materials, at least in the electrodeposited metals, is the same as in the conventional materials. This observation has also been confirmed in both the experimental [108,135] and the theoretical [107,191,192] aspects. That is, the significant role of the grain boundary in the deformation process in nanocrystalline materials is not due to the change in the grain boundary structure, but the increase in the volume fraction. In addition, the volume fraction of the triple junctions also increases with a reduction in the grain size [16].

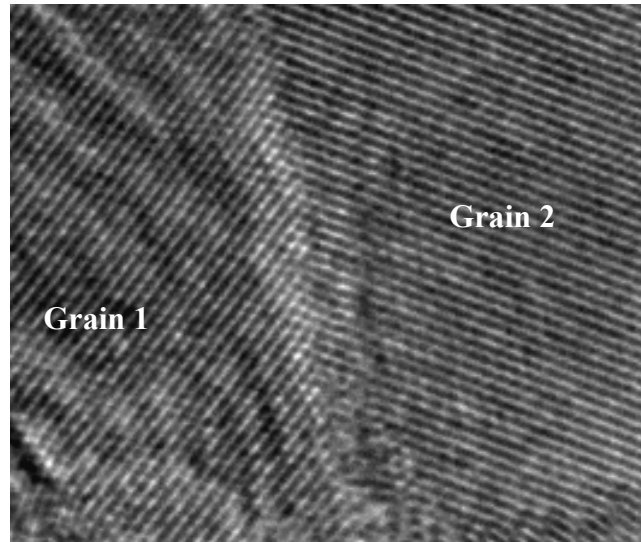


Figure 7-6. High resolution TEM image of electrodeposited Ni-Fe samples shows no evidence of second phase at the grain boundary.

In the case of the as-deposited Ni-15%Fe samples having a grain size less than 10 nm, the plastic deformation was a combination of grain boundary sliding and the dislocation activity. As suggested in the chapter 5, the large internal stresses arising from

the strain incompatibility between the grains with different grain sizes can be relieved by the events occurred at the grain boundaries, for example, grain boundary creep [26,193], and rotation of grains [40,142,184]. As a consequence, the continuous participation of differently sized grains in the plastic process resulted in the continual strain hardening. Low temperature annealing gave rise to the grain boundary relaxation. Computer simulation has revealed that, after annealing, an approximately 0.1 eV/atom shift in the peak value of the cohesive energy distribution towards the lower energy was detected in the nanocrystalline nickel with a grain size of about 12 nm [128]. Furthermore, experimental results regarding the nanocrystalline Ni-Fe alloys confirmed the atom movement from energetically unfavorable positions into low energy sites during low temperature treatment [90]. In addition, such heat treatment, to some extent, can remove part of defects such as residual stress and nanovoids, which developed during sample preparation. The relaxation of the grain boundaries can make the grain boundary activities such as the dislocation emission from the grain boundaries, grain rotations as well as the grain boundary sliding more difficult, and consequently increase the yield strength (Figure 7-4). Consistently, the very high initial strain-hardening rate of the annealed samples can be attributed to the development of high levels of internal stresses, which arise from the difficulty of the grain boundary sliding. Because of the diminished grain boundary creep and sliding, a plastic flow independence of load rate is anticipated, as observed in Figure 7-5. The decrease in the tensile elongation was associated with a relatively fast drop in the strain-hardening rate at low plastic strains, which promotes plastic instability. This observation implies that, without the continual participation of the smaller grains via the grain boundary sliding, the deformation of the larger grains does

not provide further strain hardening, resulting in immediate necking. On the other hands, a recent model has been proposed that the grain boundary diffusion is of benefit to suppress the generation of nanocracks at the grain boundary in nanocrystalline materials and so improve the ductility [194]. In other words, the low temperature annealing in some sense expedites the crack nucleation, resulting in the early failure and then the low tensile elongation. Above discussions point to a fact that not only the volume fraction but also the state of grain boundary plays the significant function in the process of plastic deformation for nanocrystalline materials.

7.3 Concluding Remarks

Both tensile and indentation experiments have been employed on the as-deposited and the annealed Ni-15%Fe specimens. The results show that the annealing for 90 min at 523 K led to an increase in the strength and a reduction in the tensile elongation. Such low temperature heat treatment also gave rise to an increase in the initial strain-hardening rate. In addition, it was found that as-deposited samples exhibited the recognized loading rate sensitivity, whereas the flow stress was independent of the loading rate after annealing. These observed phenomena are suggested to be associated with the grain boundary relaxation due to the low temperature annealing. In closing, this study confirms that the grain boundary does play an important role in the deformation of nanocrystalline materials; also, the grain boundary state is a key factor when considering the mechanical responses under the applied stress.

CHAPTER 8 THERMAL STABILITY AND GRAIN GROWTH KINETICS

Because of a high volume fraction of grain boundaries, which are in a non-equilibrium state, nanocrystalline materials have a strong tendency to transform into coarse-grained polycrystals. As shown in last chapter, the low temperature annealing mainly relaxed the grain boundaries. At elevated temperatures, the grain growth is not avoidable. Nanocrystalline materials' unique properties such as mechanical [154] and magnetic [149] properties are all grain size dependent. As a consequence, the study of the thermal stability in such materials is crucial to the emerging applications. In this chapter, isochronal and isothermal experiments were conducted on electrodeposited Ni-Fe alloys to evaluate their thermal stabilities and to understand the growth kinetics operative in the nanostructured materials. Because Ni-15%Fe and Ni-21%Fe alloy are soft magnetic materials and have a promising industrial application perspective, they were selected to be analyzed.

8.1 Isochronal Annealing

8.1.1 Effect of Temperature on Grain Size

Annealing as-deposited samples led to the microstructural recovery and grain growth. The grain size obtained from the XRD line broadening analysis as a function of the annealing temperature is displayed in Figure 8-1, in which the data regarding pure Ni [45,66], and Ni-50%Fe [45] alloys were extrapolated from corresponding references on the basis of a 90 minute annealing time. It is found that, regardless of the material type, there exist two distinct regimes. At low temperatures, the average grain size increased

gradually. However, when the annealing temperature was increased beyond a transition temperature, a rapid grain growth took place. This transition temperature was approximately 473 K and 573 K for pure nickel and Ni-Fe alloys, respectively, indicating that the Ni-Fe alloys are thermally more stable than pure nickel. This is probably associated with the addition of alloying element, which changes the mobility of the grain boundary, i.e. the solute drag effect on the grain boundary migration [162]. Such finding is more clearly confirmed by a comparison between Ni-15%Fe and Ni-21%Fe alloys, because they were fabricated under similar conditions resulting in the comparable impurity level. Generally speaking, the impurity has a function of pinning the grain boundary. It is likely concluded that the addition of iron into nickel enhances the thermal stability of nanostructures. In addition, the addition of the second phase formation element also improves the thermal stability. For example, due to the formation of a second phase, nanocrystalline nickel-1.2 wt.%P exhibited no structural changes after annealing at temperatures up to 473 K [164].

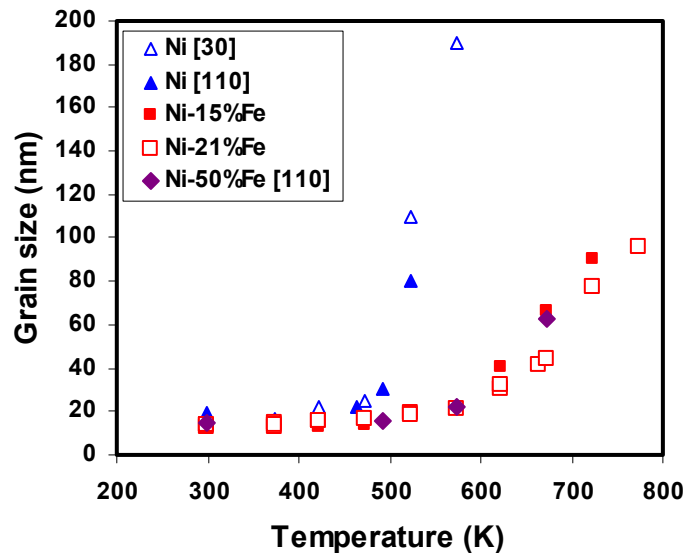


Figure 8-1. Variation of grain size as a function of annealing temperature for electrodeposited Ni and Ni-Fe alloys.

Parallel to the grain growth with annealing temperature, the crystallographic texture also changed. Table 8-1 shows the results of texture evaluation as expressed by the XRD peak intensity ratio, $I_{(111)}/I_{(200)}$. These results show that the as-deposited alloy had a slight (111) out of plane texture, as detailed in the chapter 4. In addition, the current results indicate that, increasing the annealing temperature, the texture of the annealed Ni-15%Fe and Ni-21%Fe alloys is reduced so that the orientation is closer to random. This result demonstrates that the grains with close to random orientation grew at the expense of the as-deposited (111) textured grains, which agrees well with the reported results about heat treatment of electrodeposited Ni-50%Fe alloys at 673 K [45]. However, another previously reported study [154] show that, after annealing at 673 K, the Ni-45%Fe alloy had a tendency to develop a (111) texture. These inconsistencies are probably associated with differences in levels of impurities and initial grain size and texture of the as-deposited materials.

Table 8-1. The texture of two Ni-Fe alloys annealed at different temperatures.

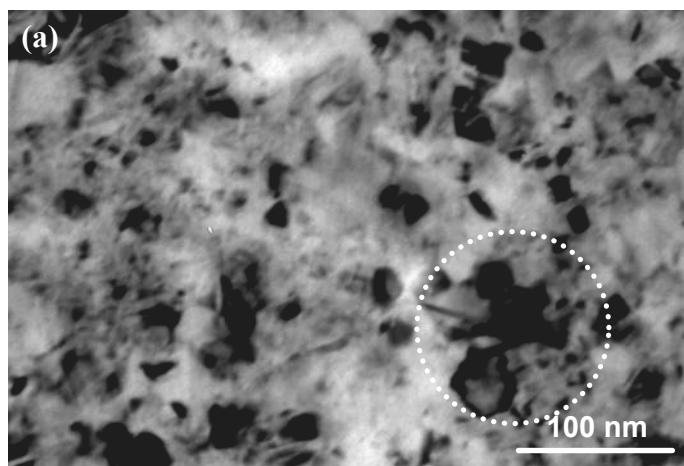
Temperature (K)		AD	373	423	473	523	573	623	663	673	723	773	
$I_{(111)}/I_{(200)}$	Ni-21%Fe	Set A	4.8	----	4.3	----	3.8	----	3.3	----	----	----	2.4
		Set B	4.2	3.7	----	4.3	----	3.7	----	2.7	2.9	2.7	----
	Ni-15%Fe	4.0	----	3.8	----	3.7	----	3.3	----	3.3	3.3	----	

Note: the standard ratio of $I_{(111)}/I_{(200)} = 1.7$.

Figure 8-2 shows the microstructures of various Ni-15%Fe samples annealed at different temperatures for 90 minutes. The as-deposited microstructure is found to be homogeneous, Figure 8-2(a). After being annealed at 523 K, the abnormal grain growth took place, i.e. few grains suddenly grew and the others remained nearly unchanged, as seen in Figure 8-2(b), where a grain of approximately 80 nm is embedded in the

nanocrystalline matrix. As the temperature was raised up to 673 K, most grains grew and connected to each other (Figure 8-2(c)). It is worth noting that there still are some nanograins kept un-grown. These TEM observations are in a good agreement with those obtained in heat treatment of electrodeposited nickel [43,44].

Abnormal grain growth was also obtained in other nanocrystalline systems such as silver and palladium [195]. However, the mechanism of abnormal grain growth in nanocrystalline materials has been not well understood. Abnormal grain growth can occur when the normal grain growth is inhibited, or when a pure material consists of some huge grains, as compared with the average grain size. Although the electrodeposited nickel and Ni-Fe alloys usually own a narrow grain size distribution, due to the presence of the low angle grain boundaries or nanocrystalline clusters with small misorientations, for example, the circled region in Figure 8-2(a), the abnormal grain growth could happen by coalescence of subgrains via slight grain rotation [43,44]. On the other hand, despite the tight grain size distribution in as-deposited sample, it is still possible that some pre-existing grains are already big enough to be the nucleation site.



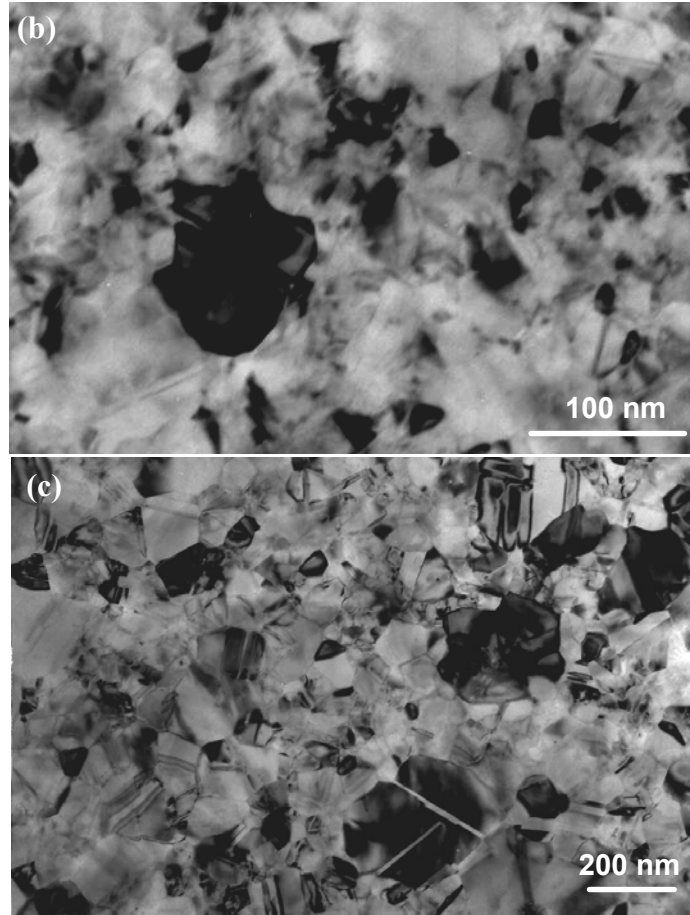


Figure 8-2. TEM micrographs of Ni-15%Fe alloy. (a) as-deposited; (b) annealed at 523 K and (c) annealed at 673 K.

8.1.2 Effect of Temperature on Internal Stresses

Figure 8-3(a) presents the lattice strain measured by the XRD line broadening analysis as a function of the annealing temperature. The scatter in the results can be attributed to the presence of internal stresses. Due to the presence of point defects, impurities, porosities or grain boundaries in the samples, there exists a local deviation of atoms from their equilibrium position. As a result, electrodeposits are heavily stressed. It can be seen that, after annealing at 373 K, the lattice strain decreased slightly. Since the grain size did not change after heat treatment at this temperature, the reduction in the lattice strain is probably associated with the local lattice relaxation of the grain boundary

regions and the remove of the point defects. Consistent with the variations in the grain size, the rate of lattice strain reduction increased with the annealing temperature. As the temperature reached up to 773 K, approximately 90% of the lattice strain was released, suggesting that the strain free grains grew and then eliminated most of the as-deposited grains. At high annealing temperatures, the lattice diffusion became possible and the reduction of microstructural defects such as vacancy clusters resulted in the further release of the internal strains. The change in the lattice strain with the grain size is plotted in Figure 8-3(b), where two regimes are observed. It appears that the drastic drop in the lattice stain happened with a slight increase in the grain size at the early stage, which is associated with the significant change in the grain boundary volume fraction with the grain size. For example, when the grain size is 10 nm, based on the equation (2-1) the grain boundary volume fraction was calculated to be approximately 13.6%. However, as the grain size is 20 nm, the grain boundary volume fraction decreases down to about 7%. Of course, due to the newly grew defect-free grains, the decrease in the microstructural defects may also play a role in the reduction in the lattice strain. When the grain size is larger than about 22 nm, the lattice strain became gradually decreased with increasing the grain size. It is interesting that this transition point is approximately corresponding to the point to begin the rapid grain growth in Figure 8-1. This observation suggests that most of lattice strain has been released within the low temperature range. As presented in the chapter 4, Ni-15%Fe deposits had a lower lattice strain than that in the Ni-21%Fe deposits. Therefore, the differences between Ni-15%Fe and Ni-21%Fe alloys, in Figure 8-3, probably come from the lower initial lattice strain in the former.

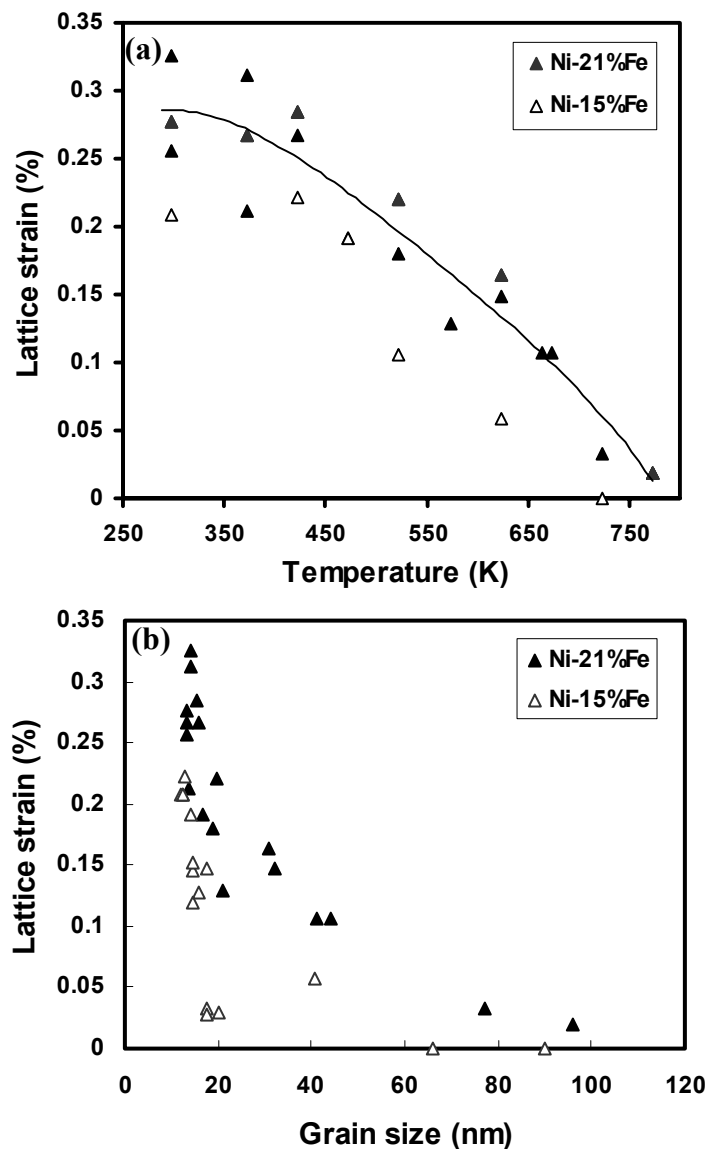
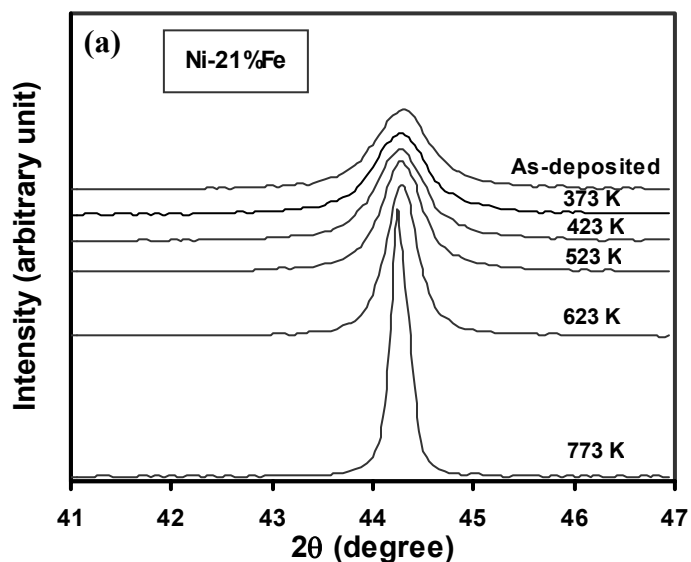


Figure 8-3. Change of the lattice strain with (a) annealing temperature and (a) grain size.

Figure 8-4 illustrates the (111) XRD peaks for as-deposited and annealed samples. It can be seen that, in the case of Ni-21%Fe alloy, the position of the (111) peak remained unchanged until the annealing temperature was increased as high as 623 K. However, the position of the (111) peak shifted noticeably toward a lower angle when the sample was annealed at 773 K. For the Ni-15%Fe alloy, the (111) peak's position started to shift at the temperature of 623 K. It was reported in the chapter 4 that the internal stresses in

nickel-iron alloys are high enough to cause bending in the deposits. This change in the lattice parameter is believed to be associated with the release of internal stresses that caused the bending of the deposits. Microstructural studies [43,45] have revealed that annealing of electrodeposited alloys results in abnormal grain growth, i.e. the microstructure of annealed samples consists of regions with two types of grains: the nanosize grains and the large grains. The studies on a nickel-50% iron alloy show that nanosize grains only occupied approximately 30% volume fraction of the structure after 673 K annealing [45]. In addition, Figure 8-2(b) shows that after 523 K annealing, only few grains abnormally grew and these large grains were isolated. However, the 673 K annealing caused many grains to grow and these grew grains connected to each other, as shown in Figure 8-2(c). It is anticipated that the samples will remain bent as long as the regions with the nanosize grains are connected. As a result, it is suggested that the sudden change in the measured lattice parameter occurs when the highly stressed nanosize grains are dispersed enough to allow the relaxation of the whole sample. The early shift of the Ni-15%Fe alloy's (111) peak is perhaps related to its both smaller initial internal stress and the lower thermal stability as compared with the Ni-21%Fe alloy.



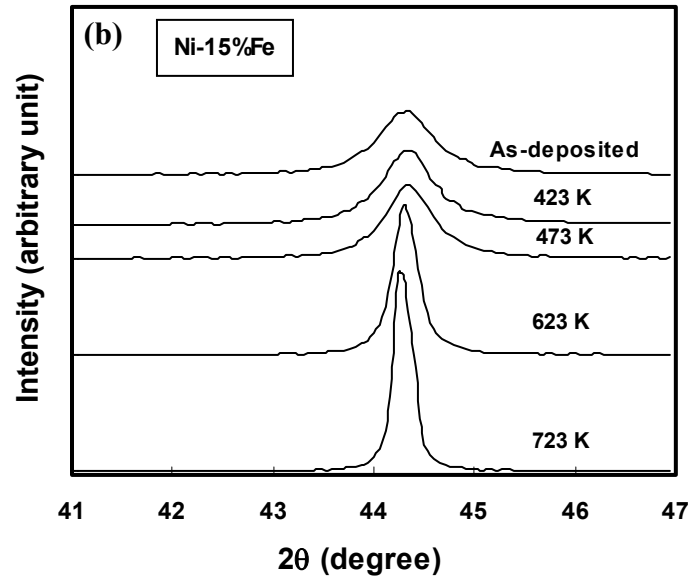


Figure 8-4. The profile of (111) XRD peak at different annealing temperatures in cases of (a) Ni-21%Fe and (b) Ni-15%Fe samples.

8.1.3 Microhardness

Figure 8-5 illustrates the change in the microhardness with the annealing temperature. After low temperature annealing, the microhardness increased slightly, although the grain size remained almost constant. This increase in hardness is consistent with the reported results in chapter 7. When increasing the temperature beyond 573 K, the microhardness began to decrease quickly as a result of the rapid grain growth. This observation correlates with the analysis of the grain growth as presented in Figure 8-1. It is worth noting that the hardness value of the as-deposited Ni-15%Fe sample is much lower than that shown in chapter 4, which has been stated in chapter 3 and proven to be due to the surface condition. The hardness values measured here on well polished surface are more accurate. However, the tendency of the change in hardness with iron content presented in the chapter 4 still stands.

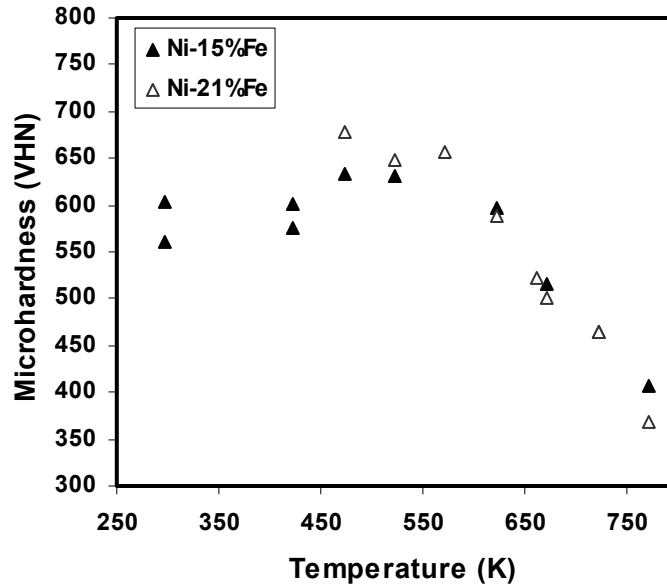


Figure 8-5. Variation of hardness with the annealing temperatures.

8.2 Isothermal Annealing

8.2.1 Microstructure

As can be seen in Figure 8-1, there are low and high temperature ranges corresponding to the slow and rapid grain growth, respectively. The transition temperature is 573 K for Ni-15%Fe alloy. In order to understand the grain growth kinetics, two temperatures of 523 and 673 K were chosen to carry out the isothermal tests, so that 523 K is within the low temperature range and 673 K is larger than the transition temperature. The Ni-15%Fe samples cut from the same deposit were used in this type of test.

The measured grain sizes by XRD line broadening technique are plotted in Figure 8-6 against the annealing time. The results show that, in the circumstance of 673 K, the grain growth rate was high in the early stage and then became moderate. For instance, the grain size skyrocketed from the initial grain size of about 12.6 nm to as high as 34 nm

only after 5 seconds of annealing. The grain growth became proportional to the annealing time at annealing times above 60 seconds. Similar observations were also obtained in studies of pure nickel [196] and Ni-45%Fe [154] alloys, which were heat treated at 693 and 673 K, respectively. For 523 K, the extreme grain growth also took place within the early stage and in less than 60 seconds. But, the grain size increased from 12.6 nm to only approximately 16 nm. After such an initial rapid growth interval, it seems that the grain size gradually leveled off. A comparison of the results between 523 and 673 K annealings reveals that the grain growth rate strongly depends on the temperature, no matter which stage.

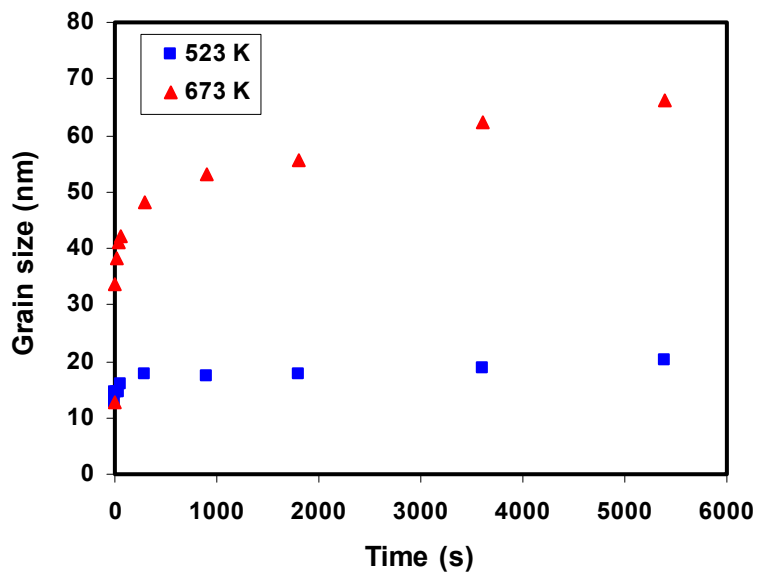


Figure 8-6. The grain size as a function of annealing time for nanocrystalline Ni-15%Fe deposits at 523 K and 673 K.

Figure 8-7 presents the change in the internal strain against the annealing time. The drastic drop of the lattice strain within the initial one minute corresponds to the rapid grain growth observed within this time period at 673 K. Beyond this point, the lattice strain became negligible. With regard to the annealing at 523 K, the internal strain was not eliminated completely and remained at an approximately constant level after five

minutes of annealing, which is parallel to the corresponding phenomenon obtained for the grain growth.

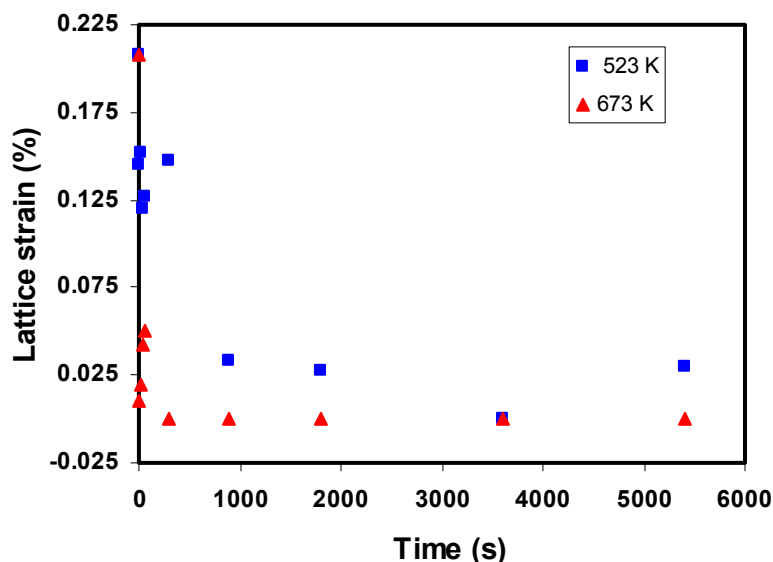


Figure 8-7. The lattice strain versus the annealing time for nanocrystalline Ni-15%Fe deposits at 523 K and 673 K.

Figure 8-8 displays the change in the microstructure with the annealing time at 523 K. It is obvious that several grains grew after 90 minute annealing (Figure 8-8(a)), and the abnormal grain growth continued up to 3210 minutes, as seen in Figure 8-8(c). However, comparing Figure 8-8(c) with Figure 8-8(d) reveals that the grains no longer grew significantly with further increasing the annealing time, indicating that the equilibrium state was approached at this point. The final structure is a mixture of some large grains and nanocrystalline grains. Combined the discussion about abnormal grain growth and such TEM observations, the grain growth process is probably suggested as: i) nucleation and abnormal grain growth in the initial state; ii) continuous abnormal grain growth stage and iii) final equilibrium state. In addition, a comparison of Figure 8-8 and Figure 2-13 [45] further confirms that the Ni-15%Fe alloy is more thermally stable than pure nickel.

In the case of high temperature, unfortunately, no TEM micrographs were taken. However, it is clear that, within the present applied time period, the grains did not stop growing, as presented in Figure 8-6. A study on nanocrystalline nickel proposed that the equilibrium state is possibly obtainable even at high temperatures [43]. More dedicated work need to be done about Ni-15%Fe alloy annealed at high temperatures with longer time period.

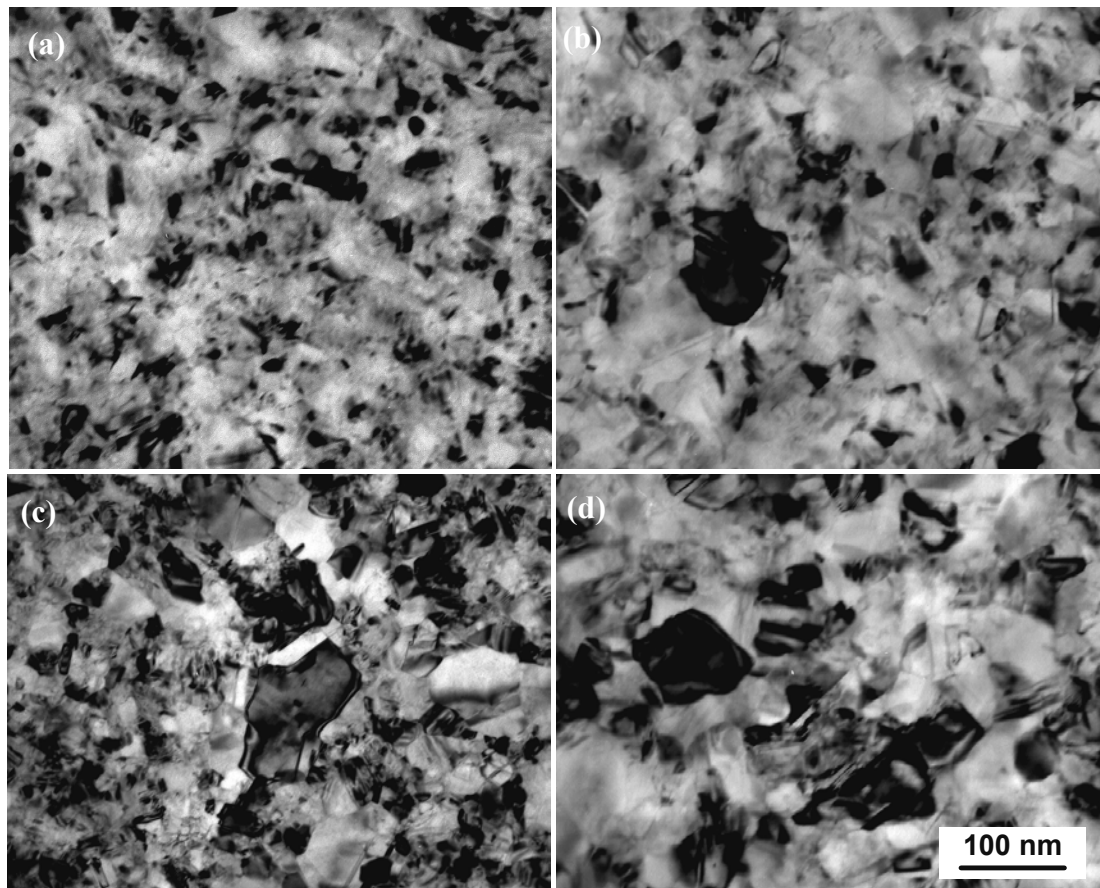


Figure 8-8. TEM bright field images of nanocrystalline Ni-15%Fe specimens annealed at 523 K. (a) as-deposited; (b) 90 min; (c) 3210 min and (d) 7490 min.

Table 8-2 summarizes the crystallographic texture for different annealing times at both 523 K and 673 K annealing temperatures. As stated in the section of isochronal test, the change in the texture mainly depended on the ‘new’ grains, which grew in a close to random orientation. At the low temperature of 523 K, the texture was unchanged after one minute, which is parallel to the observed limited grain growth (Figure 8-6). Of course, under 673 K annealing, the gradual change in texture toward the random orientation results from the continuous grain growth within this time period.

Table 8-2. Texture as a function of time at two annealing temperatures.

		Time (s)				
		0	60	1800	3600	5400
$I_{(111)}/I_{(200)}$	523	4.0	3.9	3.8	----	3.77
	673	4.0	3.6	3.4	3.3	3.3

Note: the standard ratio of $I_{(111)}/I_{(200)} = 1.7$.

Figure 8-9 plots the change in the (111) peak as a function of annealing time at 523 K and 673 K. In both cases, the gradual narrowing of the (111) peak with increasing annealing time is parallel to the continuous grain growth. The bigger degree of peak thinning in case of 673 K heat treatment is due to the corresponded faster grain growth as compared to in the circumstance of 523 K annealing at any given annealing time stage; so did the degree of the shift in the (111) peak position. The reason considering the peak position shift toward the lower 2θ angle has been detailed in the last section of isochronal annealing.

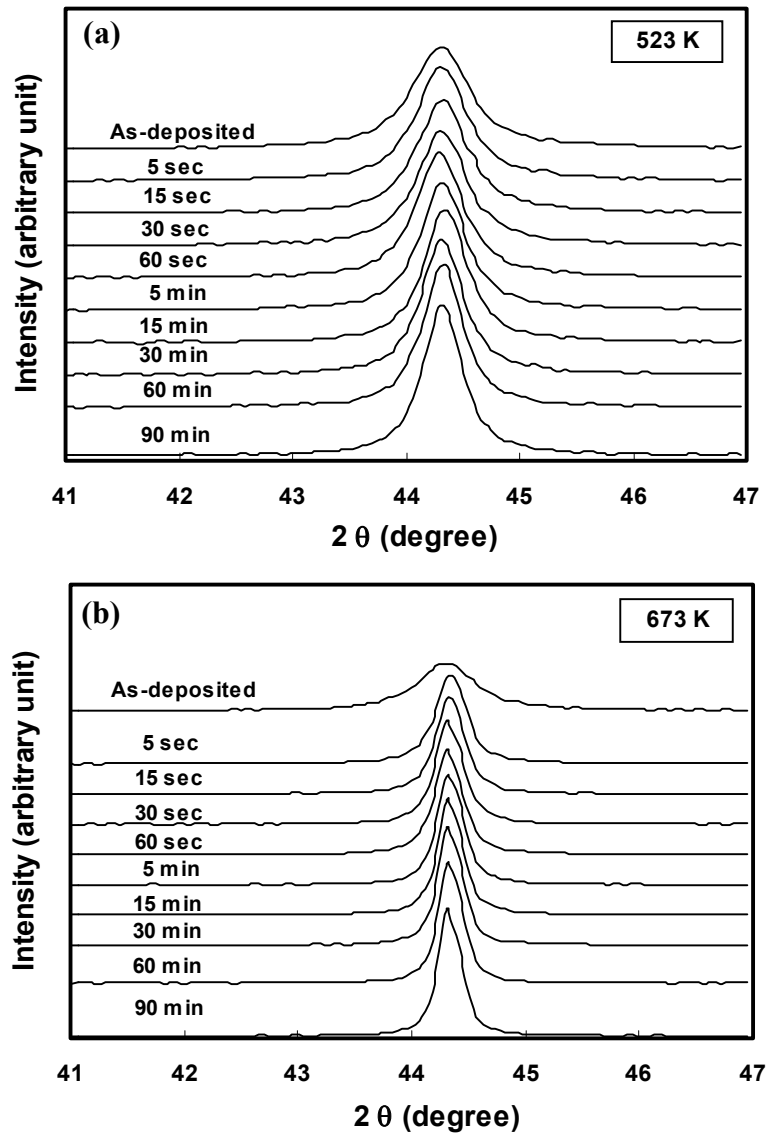


Figure 8-9. The profile of XRD (111) peak as a function of annealing time at (a) 523 K and (b) 673 K.

8.2.2 Microhardness

The change in the microhardness as a function of grain size is presented in Figure 8-10, where the microhardness values of the Ni-15%Fe and Ni-21%Fe specimens were plotted together due to the negligible difference in the composition. Additionally, in order to rule out the effect of low temperature annealing on the increase of the strength, as presented in the last chapter, the data measured on the as-deposited and short time

annealed sample (included in the circle) were not included into this Hall-Petch curve. It is of interest that an inverse Hall-Petch relationship was obtained. Such phenomena have also been observed in the as-deposited FCC Ni-Fe alloys [9,17], which is suggested to be related to the change in the deformation mechanism. The details were discussed in the last three chapters. In such case, the strongest grain size was calculated to be approximately 18.7 nm, which is comparable with that of about 12 nm for electrodeposited Permalloy [9].

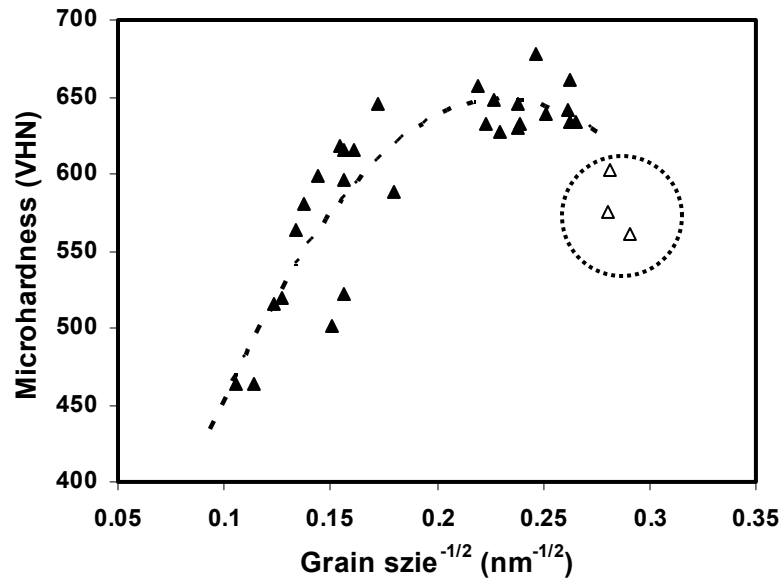


Figure 8-10. Microhardness as a function of the grain size in case of Ni-15%Fe and Ni-21%Fe alloys.

8.3 Analysis

The theory dealing with the grain growth has been well established in conventional materials [169,197-199]. Basically, the driving force for grain growth is to reduce the system energy via decreasing the grain boundary volume fraction, and the driving pressure on a grain boundary originates from its curvature. Based on the assumption of

normal grain growth, a linear relationship between the grain growth rate and the inverse grain size has been suggested [197-199]:

$$dD(t)/dt = k / D(t) \quad (8-1)$$

Here, $D(t)$ is the average grain size after annealing time t , and k is a temperature dependent constant. Integrating the equation 8-1 results in the equation [169]:

$$D(t)^2 - D_0^2 = kt \quad (8-2)$$

where D_0 is the initial grain size. As a fact, the normal grain growth is practically rare. Therefore, the most used equation is rewritten from equation 8-2 with a time component n to replace 2 in equation 8-2:

$$D(t)^n - D_0^n = kt \quad (8-3)$$

This equation is also called the generalized parabolic grain growth model and describes the isothermal grain growth, which does not follow the ideal conditions in equation 8-2. The rate constant k is expressed with a function of activation energy Q and absolute temperature T as follows, where R is the universal gas constant:

$$k = k_0 \exp(-Q/RT) \quad (8-4)$$

Combining the equations 8-3 and 8-4, the widely applied Arrhenius-type equation can be in such form:

$$D(t)^n - D_0^n = k_0 t \exp(-Q/RT) \quad (8-5)$$

Now, it is clear that the grain growth is governed by two key parameters: the time exponent n and the activation energy Q .

For the purpose of computing the time component n , equation 8-3 is typically modified as:

$$D(t) - D_0 = k't^{1/n} \quad (8-6)$$

where, k' has the same meaning as k . The grain size difference $D(t) - D_0$ against the annealing time at two isothermal measurements in case of Ni-15%Fe alloy was plotted in Figure 8-11, in which the linear relationship is obtained. The time exponent n is calculated from the slopes to be approximately 7, which is in a perfect agreement with the value of 6-7 measured for nanocrystalline nickel (starting grain size: 20 nm) annealed in a temperature range from 603 K to 683 K [155]. It is noted that the annealing temperature did not have significant influence on the time exponent values.

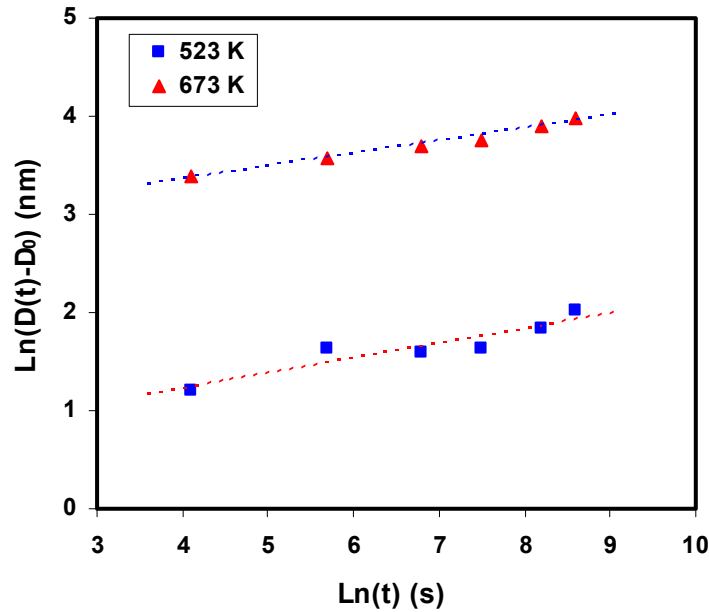


Figure 8-11. Plot of $\ln(D(t)-D_0)$ as a function of $\ln(t)$ for the Ni-15%Fe alloy isothermally annealed at 523 K and 673 K, respectively.

Apart from the time exponent, the activation energy Q is another critical factor to understand the microscopic mechanism controlling the grain growth. Ignoring the effects of slightly different composition and the temperature on the time exponent values, the Arrhenius curves for the grain growth of the Ni-15%Fe and Ni-21%Fe alloys with a time exponent of 7 were plotted in Figure 8-12 by substituting the isochronal experiment

results into equation 8-5. It is found that both curves exhibit two distinct slopes resulting in different activation energies at low and high temperatures. For the Ni-15%Fe alloy, the activation energies at low and high temperatures are $72.9 \text{ kJ mol}^{-1} \text{ K}^{-1}$ and $207.5 \text{ kJ mol}^{-1} \text{ K}^{-1}$, respectively. The corresponding values of activation energy, for the Ni-21%Fe alloy, were $52.3 \text{ kJ mol}^{-1} \text{ K}^{-1}$ and $203.2 \text{ kJ mol}^{-1} \text{ K}^{-1}$.

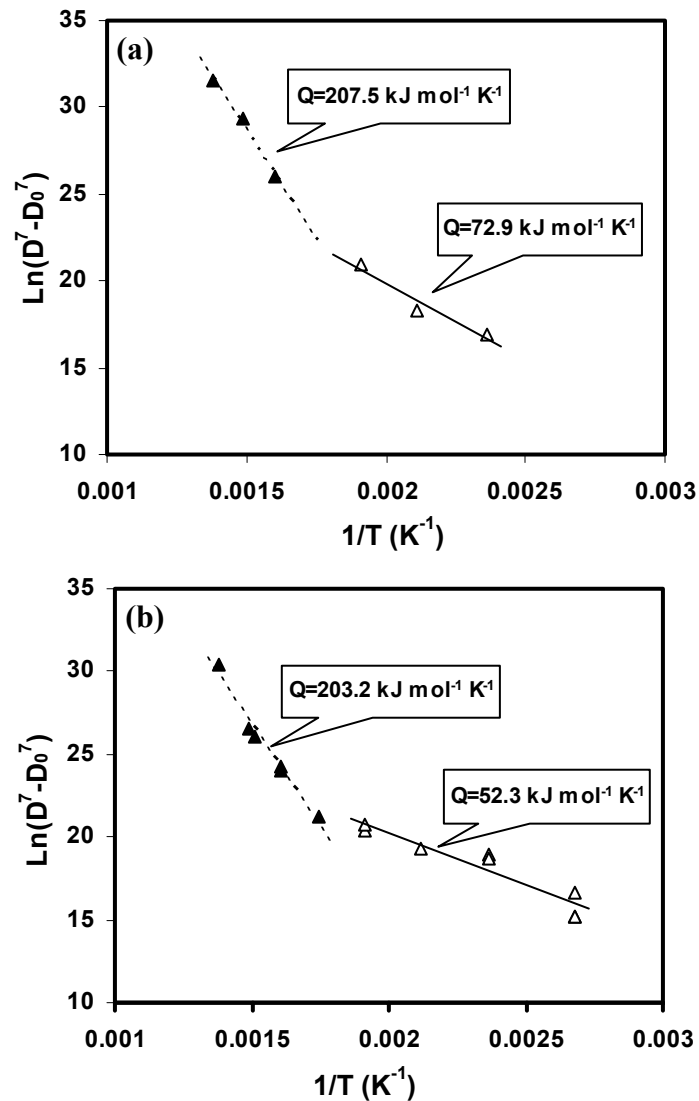


Figure 8-12. The Arrhenius curves for the grain growth in electrodeposited (a) Ni-15%Fe and (b) Ni-21%Fe alloys.

From literature, the activation energy for lattice diffusion in Ni-20%Fe and the grain boundary self-diffusion in conventional nickel are reported to be $274.6 \text{ kJ mol}^{-1} \text{ K}^{-1}$ and $104.1 \text{ kJ mol}^{-1} \text{ K}^{-1}$, respectively [200]. A comparison of the activation energies suggests that the grain growth in the nanocrystalline Ni-Fe alloys studied here is governed by different mechanisms at low and high temperatures. At low temperatures, mainly the movement of atoms within the grain boundaries achieves the grain growth. The higher activation energies calculated for the high temperature regime suggest that, as the annealing temperature is increased, the contribution of the lattice diffusion becomes more significant, implying more participation of the lattice diffusion in the grain growth process. A study of electrodeposited nanocrystalline iron also demonstrates that the grain growth exhibits two regimes [157]. The authors have suggested that the activation energies of grain boundary self-diffusion in nanocrystalline and conventional iron are different. In low and high temperature ranges, the activation energies of the grain growth correspond to the values of grain boundary self-diffusion in nanocrystalline and coarse-grained polycrystalline iron, respectively [157]. However, the results in the last chapter, recent experimental [135] and simulation [107] results all show that the structure of the grain boundaries is similar in nanocrystalline and coarse-grained materials. Therefore, the activation energy for grain boundary diffusion is expected to be the same in both materials.

It is worthy of mentioning that, within low temperature range, the computed activation energy in the case of Ni-21%Fe alloy is much lower than that for the Ni-15%Fe deposits, indicating the faster grain boundary diffusivity in the former. This is probably relevant to the higher internal stresses found in the Ni-21%Fe alloy, which

enhance the diffusion process at the grain boundaries. Without such influences, their activation energies are excellently consistent with each other at high temperatures. In addition, the activation energies measured in the current nanocrystalline alloys, at low or high temperatures, are lower than those for conventional counterparts. It has been verified that there are many intrinsic processing defects in electrodeposited materials [72]. Such porosities at grain boundaries have a function of strengthening the grain boundary diffusion because of the large free volume, and therefore, a smaller activation energy is expected. Some argue that the grain boundary diffusion rate is inherently higher in nanocrystalline materials than in the coarse-grained counterparts due to the differences in the grain boundary structures in both cases [148]. However, as discussed in the last paragraph, this possibility has been ruled out, at least in the current study.

In addition to the generalized parabolic growth model, another model of grain growth with impediment has been suggested by taking account of a limitation grain size D_∞ as time $t \rightarrow \infty$ [197,201]. Consequently, the equation 8-3 is adjusted as:

$$\frac{D_0 - D(t)}{D_\infty} + \ln\left(\frac{D_\infty - D_0}{D_\infty - D(t)}\right) = k''t \quad (8-7)$$

Figure 8-6 shows that, in the current study, the applied annealing time is not long enough to make the grain growth reach an equilibrium state, in particular at high temperatures. Accordingly, it is not possible here to evaluate this model. However, a study concerning nanocrystalline iron demonstrates that the grain growth is time and temperature dependent; the grain growth with impediment model worked well at high temperatures and longer time, while the generalized parabolic growth model had better fit at low temperatures and short times [150]. The applied parameters in the present heat

treatment experiments belong to the latter regime. It is therefore concluded that the current results can be well interpreted by the generalized parabolic growth model.

8.4 Summary

Isochronal heat treatment results show that, below 573 K, the grain size increased gradually from approximately 12 nm to 22 nm; above 573 K the grains grew more rapidly. Accompanied with the grain growth, the lattice strain decreased. The sudden change in the lattice parameter after annealing at temperatures higher than 623 K is attributed to the loss of connectivity of the nanosize grains, which are highly stressed. An addition of alloying element is believed to benefit the thermal stability. At 673 K, the grain growth rate is initially high, resulting in an abrupt increase in the grain size from about 12 nm to 42 nm within one minute. However, the change in the grain size was only approximately 4 nm for annealing at 523 K during the same time period. Beyond this time, the grains grew slowly in both cases. Of course, the grain growth rate at 673 K was much higher than at 523 K. Parallel to the sudden grain growth in the early stage, the lattice grain dropped rapidly.

It is suggested that the low temperature regime (below 575 K) is accommodated mainly by the grain boundary diffusion, while the high temperature regime is assisted by the lattice diffusion. Under current applied parameters, our results support the generalized parabolic growth model. The grain growth still can be described by

$$D(t)^n - D_0^n = k_0 t \exp(-Q/RT), \text{ where } n \text{ is } 7.$$

CHAPTER 9 CONCLUSIONS

Electrodeposition has proven to be a powerful technique to synthesize nanocrystalline metallic materials. By changing the ratio of nickel to iron ion in the electrolyte, Ni-Fe alloys with different compositions were fabricated without using additives. The results show that the composition distribution was very homogenous throughout the deposits. Furthermore, TEM observations disclosed that the grain size distribution was relatively tight. An addition of above 15% iron into nickel caused a drastic decrease in the grain size. Accompanyingly, the texture changed from a strong (100) to a slight (111) orientation. Within the iron content range of 15% to 60%, the grain size remained nearly constant at a scale of approximately 11 nm. However, with increasing the iron content in the deposits, the lattice strain continuously increased. As the iron concentration was equal to or more than 35%, due to the large residual stresses, a network of microcracking was observed. Interestingly, the microcrack pattern was dependent of the iron content. In addition, the microhardness also varied with the iron content, and a maximum was obtained within the iron content of approximately 15% to 20%.

Because of the low internal stresses, the Ni-15%Fe alloy with a grain size of around 10 nm was chosen to carry out the tensile tests. The results illustrate that this material had a strength as high as 2.4 GPa. It is of surprise that the tensile elongation to failure was up to 6%, which is the first time to show that FCC nanocrystalline metals exhibit such high tensile ductility at a grain size level of approximately 10 nm. This enhanced plastic

elongation probably originates from high quality of the deposit and mixed contributions from grain boundary sliding, dislocation motion and a high strain hardening rate. Compared with the published results and the conventional ultrahigh strength 300M steel, current study indicates that, in fact, nanocrystalline FCC metals are not intrinsically brittle and have a promising prospect for practical applications.

In general, the fracture surface showed a microvoid structure. At high magnifications, it was found that the microvoid geometry depended on the stress state, and the scale of microvoid was approximately several times of the grain size. Despite the microvoid-like fracture surface, TEM observation revealed that the fracture path was intergranular.

On the side surface of tensile samples, the deformation bands, plastic zone and the adjoining of secondary microcracks were found. Detailed analysis uncovered that the development of plastic zone and the advancement of the microcracks are cooperative. The plastic zone firstly develops ahead of a microcrack; 'new' microcracks nucleate preferably within such plastic zones and then connect with the main crack, and so on. On the basis of comprehensive fractographic examination, in the case of defect-free specimens, the fracture was determined to begin with necking although the area reduction was relatively limited. A model was developed to describe the failure course in defect-free nanocrystalline FCC metals. With the presence of large defects, the crack propagation was easily initiated at these defects due to the stress concentration, consequently resulting in loss of ductility due to notch sensitivity.

On the other hand, when the grain size is larger than 40 nm, it was found that the deformation and fracture behaviors changed. In addition to the improved tensile

elongation, both Ni and Ni-6%Fe samples failed with severe necking preceding fracture and in some cases the knife-edge behavior was observed. Additionally, the observation of deep dimple structure strongly suggests the void coalescence mechanism. Similar to the Ni-15%Fe alloy were found, the deformation bands were seen near the fracture surface, but no secondary microcracks. It is further determined that, in the issue of pure nickel and Ni-6%Fe alloy having a grain size larger than 40 nm, the deformation bands only developed within the diffusive necking region. The difference in these tensile behaviors is thought to result from the change in the deformation mechanism. Computer simulations suggest that, as the grain size is reduced below approximately 15 nm, the deformation is dominated by grain boundary sliding; while the dislocation activity is believed to govern the plastic process when the grain size is beyond 20 nm. Finally, a comparison between pure nickel and Ni-6%Fe alloy shows that the addition of the alloying element led to the increase in both the strength and the initial strain-hardening rate, which is associated with lowering the stack fault energy by adding the iron into the nickel.

Due to the grain boundary relaxation at low temperatures, the strength and the ductility were found to increase and decrease, respectively, which is consistent with the prediction by computer simulation. Further confirmation was achieved by constant load-rate indentation tests, where the as-deposited samples exhibited an apparent load rate sensitivity, while the annealed specimens were load rate independent. This is ascribed to the reduced degree of the grain boundary sliding's participation in the plastic deformation after annealing.

Apart from the grain boundary relaxation, the grains have a strong tendency to grow at elevated temperatures, which was examined using isothermal and isochronal experiments in the current study. The results showed that alloying element has a function of enhancing the thermal stability because of its drag force on the grain boundary. For isothermal test at 523 K and 673 K, the grain size increased rapidly within the first one minute and then the grain growth became gradual as the time was further increased. Parallel to the grain growth, the lattice strain decreased. Also, the position of the (111) peak shifted toward a lower angle value because of the release of the internal stresses. It is suggested that the sudden shift occurs because the grown grains connect to each other. The isochronal annealings were conducted within a temperature range of 373 k to 773 k for 90 minutes. Two temperature ranges were noted. Within the low temperature region, the computed activation energy was comparable to that for the grain boundary diffusion. While, as the temperature was raised beyond 573 K, the deduced activation energy was in a good agreement with the lattice diffusion activation energy. Regardless of the annealing temperature, the grain growth was suggested to follow the generalized parabolic grain growth mechanism described by the equation of $D(t)^n - D_0^n = k_0 t \exp(-Q/RT)$, where the time exponent n was measured to be approximately 7.

In summary, in this dissertation, the nanocrystalline Ni-Fe alloys were systemically characterized in the mechanical and thermal aspects. The results render deep insights into more understanding about nanocrystalline materials, and provide solid evidences for future applications of nanomaterials.

LIST OF REFERENCES

1. Gleiter H., *Prog. Mater. Sci.* **33**, 223 (1989).
2. Granqvist C.G., and Buhrman R.A., *J. Appl. Phys.* **47**, 2200 (1976).
3. Ebrahimi F., Bourne G.R., Kelly M.S., and Matthews T.E., *NanoStruct. Mater.* **11**, 343 (1999).
4. Gleiter H., *Phys. Blätter* **47**, 753 (1991).
5. Weertman J.R., Farkas D., Hemker K., Kung H., Mayo M., Mitra R., and Van Swygenhoven H., *MRS Bull.* **24**, 44 (1999).
6. Aravinda C.L., and Mayanna S.M., *Trans. Inst. Metal Finish.* **77**, 87 (1999).
7. Osaka T., Takai M., Sogawa Y., Momma T., Ohashi K., Saito M., and Yamaha K., *J. Electrochem. Soc.* **146**, 2092 (1999).
8. Osaka T., Takai M., Hayashi K., Sogawa Y., Ohashi K., Saito M., and Yamaha K., *Nature* **387**, 796 (1998).
9. Cheung C., Palumbo G., and Erb U., *Scripta Metall. Mater.* **31**, 735 (1994).
10. Ebrahimi F., Ahmed Z., and Morgan K.L., *Mat. Res. Soc. Proc.*, **634**, B2.7.1 (2001).
11. Dalla Torre F., Van Swygenhoven H., and Victoria M., *Acta Mater.* **50**, 3957 (2002).
12. Legros M., Elliott B.R., Rittner M.N., Weertman J.R., and Hemker K.J, *Philo. Mag. A* **80**, 1017 (2000).
13. Wang Y.M., Ma E., and Chen M.W., *Appl. Phys. Lett.* **80**, 2395 (2002).
14. Jeong D.H., Erb U., Aust K.T., and Palumbo G., *Scripta Mater.*, **48**, 1067 (2003).
15. Zhou F., Liao X.Z., Zhu Y.T., Dallek S., and Lavernia E.J., *Acta Mater.* **51**, 2777 (2003).
16. Wang N., Wang Z., Aust K.T., and Erb U., *Mater. Sci. Eng. A* **237**, 150 (1997).
17. Cheung C., Djuanda F., Erb U., and Palumbo G., *NanoStruct. Mater.* **5**, 513 (1995).

18. Iwasaki H., Higashi K., and Nieh T.G., *Scripta Mater.* **50**, 395 (2004).
19. Morgan K.L., Ahmed Z., and Ebrahimi F., *Mat. Res. Soc. Symp.* **634**, B3.11.1 (2001).
20. Koch C.C., *Scripta Mater.* **49**, 657 (2003).
21. Qin X.Y., Lee J.S., and Lee C.S., *J. Mater. Res.* **17**, 991 (2002).
22. Yamakov V., Wolf D., Salazar M., Phillpot S.R., and Gleiter H., *Acta Mater.* **49**, 2713 (2001).
23. Yamakov V., Wolf D., Phillpot S.R., Mukherjee A.K., and Gleiter H., *Nature Mater.* **3**, 43 (2004).
24. Yamakov V., Wolf D., Phillpot S.R., Mukherjee A.K., and Gleiter H., *Nature Mater.* **1**, 45 (2002).
25. Yamakov V., Wolf D., Phillpot S.R., and Gleiter H., *Acta Mater.* **50**, 5005 (2002).
26. Yamakov V., Wolf D., Phillpot S.R., and Gleiter H., *Acta Mater.* **50**, 61 (2002).
27. Liao X.Z., Zhou F., Lavernia E.J., Srinivasan S.G., Baskes M.I., He D.W., and Zhu Y.T., *Applied Phys. Lett.* **83**, 632 (2003).
28. Liao X.Z., Zhou F., Lavernia E.J., He D.W., and Zhu Y.T., *Applied Phys. Lett.* **83**, 5062 (2003).
29. Li H.Q., and Ebrahimi F., *Acta Mater.* **51**, 3905 (2003).
30. Ebrahimi F., Zhai Q., and Kong D., *Mater. Sci. Eng. A* **255**, 20 (1998).
31. Youngdahl C.J., Sanders P.G., Eastman J.A., and Weertman J.R., *Scripta Mater.* **37**, 809 (1997).
32. Van Swygenhoven H., and Weertman J.R., *Scripta Mater.* **49**, 625 (2003).
33. Ma E., *Scripta Mater.* **49**, 663 (2003).
34. Dieter G.E., *Mechanical Metallurgy*, 3rd ed. McGraw-Hill, Boston, 1986.
35. Schiøtz J., Di Tolla F.D., and Jacobsen K.W., *Nature* **391**, 561 (1998).
36. Van Swygenhoven H., and Derlet .M., *Phys. Rev. B* **64**, 224105 (2001).
37. Van Swygenhoven H., Caro A., and Farkas D., *Mater. Sci. Eng. A* **309-310**, 440 (2001).

38. Van Swygenhoven H., Spaczer M., Caro A., and Farkas D., *Phys. Rev B* **60**, 22 (1999).
39. Van Swygenhoven H., Spaczer M., Farkas D., and Caro A., *NanoStruct. Mater.* **12**, 323 (1999).
40. Schiøtz J., Vegge T., Di Tolla F.D., and Jacobsen K.W., *Phys. Rev. B* **60**, 11971 (1999).
41. Yamakov V., Wolf D., Phillpot S.R., Mukherjee A.K., and Gleiter H., *Philo. Mag. Lett.* **83**, 385 (2003).
42. Schiøtz J., and Jacobsen K.W., *Science* **301**, 1357 (2003).
43. Klement U., Erb U., EL-Sherik A.M., and Aust K.T., *Mater. Sci. Eng. A* **203**, 177 (1995).
44. Wang N., Wang Z., Aust K.T., and Erb U., *Acta Mater.* **45**, 1655 (1997).
45. Thuvander M., Abraham M., Cerezo A., and Smith G.D.W., *Mater. Sci. Technol.* **17**, 961 (2001).
46. Taylor W.P., Brand O., and Allen M.G., *J. MEMS* **7**, 181 (1998).
47. O'Sullivan E.J., Cooper E.I., Romankiw L.T., Kwietniak K.T., Trouilloud P.L., Horkans J., Jahnes C.V., Babich I.V., Krongelb S., Hegde S.G., Tornello J.A., LaBianca N.C., Cotte J.M., and Chainer T.J., *IBM J. Res. Dev.* **42**, 681 (1998).
48. Knodle J.M., *Printed Circuit Fabrication* **58**, 10 (1987).
49. Chinnasamy C.N., Narayanasamy A., Ponpandian N., Chattopadhyay K., and Saravanakumar M., *Mater. Sci. Eng. A* **304-306**, 408 (2001).
50. Chinnasamy C.N., Narayanasamy A., Chattopadhyay K., and Ponpandian N., *NanoStruct. Mater.* **12**, 951 (1999).
51. Lorenz T., Moske M., Kufler H., Geisler H., and Samwer K., *J. Appl. Phys.* **78**, 4765 (1996).
52. Frase H.N., Shull R.D., Hong L.-B., Stephens T.A., Gao Z.-Q., and Fultz B., *Nanostruct. Mater.* **11**, 987 (1999).
53. Pekała M., Oleszak D., Jartych E., and Żurawicz J.K., *Nanostruct. Mater.* **11**, 789 (1999).
54. Gong W., Li H., and Chen J., *J. Appl. Phys.* **69**, 5119 (1991).
55. Sander P.G., Eastman J.A., and Weertman J.R., *Acta Mater.* **45**, 4019 (1997).

56. Koch C.C., and Cho Y.S., *NanoStruct. Mater.* **1**, 207 (1992).
57. Daroczi L., Beke D.L., Posgay G., Zhou G.F., and Bakka H., *Nanostruct. Mater.* **2**, 515 (1993).
58. Li M., Birringer R., Johnson W.L., and Shull R.D., *Nanostruct. Mater.* **3**, 407 (1993).
59. Tellkamp V.L., Melmed A., and Lavernia E.J., *Metall. Mater. Trans. A* **32**, 2335 (2001).
60. Zhang X., Wang H., Scattergood R.O., Narayan J., and Koch C.C., *Mater. Sci. Eng. A* **344**, 175 (2003).
61. Shull R.D., and Bennett L.H., *Nanostruct. Mater.* **1**, 83 (1992).
62. Tsoukatos A., Wan H., and Hadjipanayis G.C., *Nanostruct. Mater.* **4**, 49 (1994).
63. Hugo R.C., Kung H., Weertman J.R., Mitra R., Knapp J.A., and Follstaedt D.M., *Acta Mater.* **51**, 1937 (2003).
64. Alexandrov I.V., Zhu Y.T., Lowe T.C., and Valiev R.Z., *Powder Metallurgy* **41**, 11 (1998).
65. Czerwinski F., *J. Electrochem. Soc.* **143**, 3327 (1996).
66. Natter H., Schmelzer M., and Hempelmann R., *J. Mater. Res.* **13**, 1186 (1998).
67. Dehlinger U., and Giesen F., *Z. Metallk.* **24**, 197 (1932).
68. Lu L., Wang L.B., Ding B.Z., and Lu K., *J. Mater. Res.* **15**, 270 (2000).
69. Nieman G.W., Weertman J.R., and Siegel R.W., *Scripta Metall. Mater.* **24**, 145 (1990).
70. Karimpoor A.A., Erb U., Aust K.T., and Palumbo G., *Scripta Mater.* **49**, 651 (2003).
71. Iwasaki H., Higashi K., and Nieh T.G., *Mat. Res. Soc. Symp. Proc.* **740**, I3.28.1 (2003).
72. Petegem S.V., Torre F.D., Segers D., and Swygenhoven H.V., *Scripta Mater.* **48**, 17 (2003).
73. Brenner A., *Electrodeposition of Alloys*, Vol. 1, chap. 31, Academic Press, New York, 1963.
74. Nakamura K., Umetani M., and Hayashi T., *Surf. Technol.* **25**, 111 (1985).
75. Gangasingh D., and Talbot J.B., *J. Electrochem. Soc.* **138**, 3605 (1991).

76. Yin K.M., and Lin B.T., Surf. Coat. Technol. **78**, 205 (1996).
77. Andricacos P.C., Arana C., Tabib J., Dukovic J., and Romankiw L.T., J. Electrochem Soc. **136**, 1336 (1989).
78. Clauss R.J., and Tremmel R.A., Plating **51**, 803 (1973).
79. Tremmel R.A., Plating and Surface Finishing **68** (2), 30 (1981).
80. Dennis J.K., and Such T.E., Nickel and Chromium Plating, 2nd edition, Butterworth & Co (publisher) Ltd., Cambridge, 1986, p321.
81. Leith S.D., Ramli S., and Schwartz D.T., J. Electrochem. Soc. **146**, 1431 (1999).
82. Grimmitt D.L., Schwartz M., and Nobe K., Plat. Surf. Finish. **75**, 94 (1988).
83. Kieling V.C., Surface Coating Technology **96**, 135 (1997).
84. Grimmitt D.L., Schwartz M., and Nobe K., J. Electrochem. Soc. **140**, 973 (1993).
85. Jette E.R., and Foote F., Trans. A.I.M.M.E. **120**, 259 (1936).
86. Hadian S.E., and Gabe D.R., Surface and Coating Technology **122**, 118 (1999).
87. Czerwinski F., Electrochimica Acta. **44**, 667 (1998).
88. Czerwinski F., and Kedzierski Z., J. Mater. Sci. **32**, 2957 (1997).
89. Fultz B., Kuwano H., and Ouyang H., J. Appl. Phys. **77**, 3458 (1995).
90. Frase H.N., Fultz B., Roberts J.L., and Spooner S., Phil. Mag. **80**, 1545 (2000).
91. Van Swygenhoven H., Spaczér M., and Caro A., NanoStruct. Mater. **12**, 629 (1999).
92. Birringer R., Herr U., and Gleiter H., Trans. Jpn. Inst. Metal. **27**, 43 (1986).
93. Gifkins R.C., Metall. Trans.A **7A**, 1225 (1976).
94. Van Swygenhoven H., and Caro A., Appl. Phys. Lett. **71**, 12 (1997).
95. Van Swygenhoven H., Spaczer M., and Caro A., Proc. MRS Fall Meeting, 1998.
96. Birringer R., Herr U., and Gleiter H., Physics Let. A **102**, 365 (1984).
97. Birringer R., Mater. Sci. Eng. A **117**, 33 (1989).
98. Zhu X., Birringer R., Herr U., and Gleiter H., Phys. Rev. B **35**, 9085 (1987).

99. Haubold T., Birringer R., Lengeler B., and Gleiter H., *Phys. Lett. A* **135**, 461 (1989).
100. Ranganathan S., Divakar R., and Raghunathan V.S., *Scripta Mater.* **44**, 1169 (2001).
101. Fitzsimmons M.R., Eastman J.A., Mullerstach M., and Wallner G., *Phys. Rev. B* **44**, 2452 (1991).
102. Eastman J.A., Fitzsimmons M.R., and Thompson L.J., *Philos. Mag. B* **66**, 667 (1992).
103. Thomas G.J., Siegel R.W., and Eastman J.A., *Scripta Metall. Mater.* **24**, 201 (1990).
104. Wunderlich W., Ishida Y., and Maurer R., *Scripta Metall. Mater.* **24**, 403 (1990).
105. Ganapathi S.K., and Rigney D.A., *Scripta Metall. Mater.* **24**, 1675 (1990).
106. Siegel R.W., and Thomas G.J., *Ultramicroscopy* **40**, 376 (1992).
107. Van Swygenhoven H., Farkas D., and Caro A., *Phys. Rev. B* **62**, 831 (2000).
108. Kumar K.S., Van Swygenhoven H., and Suresh S., *Acta Mater.* **51**, 5743 (2003).
109. Mills M.J., and Daw M.S., *Mat. Res. Soc. Proc.* **183**, 15 (1990).
110. Hall E.O., *Proc. Phys. Soc. Lond. B* **64**, 747 (1951).
111. Petch N.J., *J. Iron Steel Inst. Lond.* **173**, 25 (1953).
112. Conrad H., *Mater. Sci. Eng. A* **341**, 216 (2003).
113. Siegel R.W., and Fougere G.E., *NanoStruct. Mater.* **6**, 205 (1995).
114. Qin X.Y., Zhu X.G., Gao S., Chi L.F., and Lee J.S., *J. Phys.: Condens. Matter.* **14**, 2605 (2002).
115. Sakai S., Tanimoto H., and Mizubayashi., *Acta Mater.* **47**, 211 (1999).
116. Ebrahimi F., and Zhai Q., *Scripta Mater.* **39**, 1401 (1998).
117. Xiao C.H., Mirshams R.A., Whang S.H., and Yin W.M., *Mater. Sci. Eng. A* **301**, 35 (2001).
118. Sanders P.G., Youngdahl C.J., and Weertman J.R., *Mater. Sci. Eng. A* **234-236**, 77 (1997).
119. Erb U., *NanoStruct. Mater.* **6**, 533 (1995).

120. El-Sherik A.M., Erb U., Palumba G., and Aust K.T., *Scripta Metall. Mater.* **27**, 1185 (1992).
121. Nieh T.G., and Wadsworth J., *Scripta Metall. Mater.* **25**, 955 (1991).
122. Yip S., *Nature* **391**, 532 (1998).
123. Hertzberg R.W., *Deformation and Fracture Mechanism of Engineering Materials*, 3rd ed. New York: John Wiley and Sons, 1989, p392.
124. Zhang X., Wang H., Scattergood R.O., Narayan J. Koch C.C., Sergueeva A.V., and Mukherjee A.K., *Acta Mater.* **50**, 4823 (2002).
125. Qin X.Y., Zhu X.G., Gao S., Chi L.F., and Lee J.S., *Scripta Mater.* **46**, 611 (2002).
126. Gray III G.T., Lowe T.C., Cady C.M., Valiev R.Z., and Aleksandrov I.V., *NanoStruct. Mater.* **9**, 477 (1997).
127. McFaden S.X., Mishra R.S., Valiev R.Z., Zhilyaev A.P., and Mukherjee A.K., *Nature* **398**, 684 (1999).
128. Hasnaoui A., Van Swygenhoven H., and Derlet P.M., *Acta Mater.* **50**, 3927 (2002).
129. Ebrahimi F., Zhai Q., and Kong D., *Scripta Mater.* **39**, 315 (1998).
130. Emery R.D., and Povirk G.L., *Acta Mater.* **51**, 2067 (2003).
131. Emery R.D., and Povirk G.L., *Acta Mater.* **51**, 2079 (2003).
132. Schwaiger R., Moser B., Dao M., Chollacoop N., and Suresh S., *Acta Mater.* **51**, 5159 (2003).
133. Johnson D.R., *Toughness of Tempered Bainitic Microstructures in a 4150 Steel*, Master's Thesis, University of Tennessee, 1990.
134. Dodd B., and Bai Y., *Ductile Fracture and Ductility*, Academic Press Inc., London, 1987, p2.
135. Kumar K.S., Suresh S., Chisholm M.F., Horton J.A., and Wang P., *Acta Mater.* **51**, 387 (2003).
136. Ebrahimi F., and Zhai Q., *Scripta Mater.* **39**, 1410 (1998).
137. Hasnaoui A., Van Swygenhoven H., and Derlet P.M., *Science* **300**, 1550 (2003).
138. Farkas D., Van Swygenhoven H., and Derlet P.M., *Phys. Rev. B* **66**, 060101(R) (2002).
139. Chokshi A.H., Rosen A., Karch J., and Gleiter H., *Scripta Metall.* **23**, 1679 (1989).

140. Yip. S., *Nature Mater.* **3**, 11 (2004).
141. Mitra R., Ungar T., Morita T., Sanders P.G., and Weertman J.R., The 1999 Weertman J.R. Symposium, ed. Chung Y.-W., Dunad D.C., Liaw P.K., and Olsen G.B., TMS Publication, Warrendale, PA, 1999, p553.
142. Ke M., Hackney S.A., Milligan W.W., and Aifantis E.C., *NanoStruct. Mater.* **5**, 689 (1995).
143. Chen M., Ma E., Hemker K.J., Sheng H., Wang Y., and Cheng X., *Science* **300**, 1275 (2003).
144. Derlet P.M., and Van Swygenhoven H., *Philo. Mag. A* **82**, 1 (2002).
145. Gleiter H., *Physica Stat. Sol. B* **172**, 41 (1992).
146. Larikov L.N., *Metallofizika Noveyshie Tehnologii.* **17**, 3 (1995).
147. Bokstein B.S., Brose H.D., Trusov L.I., and Khvostantseva T.P., *NanoStruct. Mater., Proc. of 2nd Intl. Conf. on NanoStruct. Materials*, Stuttgart University, Germany, **6**, 873 (1999).
148. Kolobov Y.R., Grabovetskaya G.P., Ivanov M.B., Zhilyaev A.P., and Valiev R.Z., *Scripta Mater.* **44**, 873 (2001).
149. Przenioslo R., Winter R., Natter H., Schmelzer M., Hempelmann R., and Wagner W., *Phys. Rev. B* **63**, 054408 (2001).
150. Malow T.R., and Koch C.C., *Acta Mater.* **45**, 2177 (1997).
151. Metha C.S., Smith D.A., and Erb U., *Mater. Sci. Eng. A* **204**, 227 (1995).
152. Jiang H., Zhu Y.T., Butt D.P., Alexandrov I.V., and Lowe T.C., *Mater. Sci. Eng. A* **290**, 128 (2000).
153. Natter H., and Hempelmann R., *J. Phys. Chem.* **100**, 19525 (1996).
154. Czerwinski F., Li H., Megret M., Szpunar J.A., Clark D.G., and Erb U., *Scripta Mater.* **37**, 1967 (1997).
155. Iordache M.C., Whang S.H., Jiao Z., and Wang Z.M., *NanoStruct. Mater.* **11**, 1343 (1999).
156. Natter H., Löffler M.-S., Krill C.E., and Hempelmann R., *Scripta Mater.* **44**, 2321 (2001).
157. Natter H., Schmelzer M., Löffler M.-S., Krill C.E., Fitch A., and Hempelmann R., *J. Phys. Chem. B* **104**, 2467 (2000).

158. Czerwinski F., Szpunar J.A., and Erb U., *J. Mater. Sci.: Mater. Electronics* **11**, 243 (2000).
159. Weissmüller J., *NanoStruct. Mater.* **3**, 261 (1993).
160. Krill C.E., Klein R., Janes S., and Birringer R., *Mater. Sci. Forum* **179-181**, 443 (1995).
161. Eckert J., Holzer J.C., and Johnson W.L., *J. Appl. Phys.* **73**, 131 (1993).
162. Knauth P., Charai A., and Gas P., *Scripta Metall. Mater.* **28**, 325 (1993).
163. Perez R.J., Jiang H.G., Dogan C.P., and Lavernia E.J., *Metall. Trans. A* **29**, 2469 (1998).
164. Boylan K., Ostrander D., Erb U., Palumbo G., and Aust K.T., *Scripta Metall. Mater.* **25**, 2711 (1991).
165. Höfler H.J., and Averbach R.S., *Scripta Metall. Mater.* **24**, 2401 (1990).
166. Bansal C., Gao Z., and Fultz B., *NanoStruct. Mater.* **5**, 327 (1995).
167. Gao Z., and Fultz B., *NanoStruct. Mater.* **4**, 939 (1994).
168. Gao Z., and Fultz B., *NanoStruct. Mater.* **2**, 231 (1993).
169. Humphreys F.J., and Hatherly M., *Recrystallization and Related Annealing Phenomena*, Pergamon, New York, 1995, p284.
170. Kaur I., Gust W., and Kozma L., *Handbook of Grain and Interphase Boundary Diffusion Data*, Ziegler Press, Stuttgart, 1989.
171. Ahmed Z., Master's Thesis, University of Florida, (2001).
172. Grimmett D.L., Schwartz M., and Nobe K., *J. Electrochem. Soc.* **137**, 3414 (1990).
173. Yin K.M., and Lee C.C., *J. Chem. Tech. Biotechnol.* **70**, 337 (1997).
174. Koryta J., Dvořák J., and Boháčková V., *Electrochemistry*, Methuen & Co. Ltd, London, 1970, p136.
175. Cardarelli F., *Materials Handbook*, Springer, New York, 1999, p36 and p39.
176. Petrovic J.J., *J. Mater. Sci.* **36**, 1579 (1999).
177. Hausch G., and Warlimont H., *Zeitschrift für Metalkunde*, **63**, 547 (1972).
178. Oniciu L., and Muresan L., *Reviews of Appl. Chem.* **29**, 565 (1991).

179. Li H., Czerwinski F., and Szpunar J.A., *NanoStruct. Mater.* **9**, 673 (1997).
180. Valiev R.Z., Alexandrov I.V., Zhu Y.T., and Lowe T.C., *J. Mater. Res.* **17**, 5 (2002).
181. Wang Y., Chen M., Zhou F., and Ma E., *Nature* **419**, 912 (2002).
182. Valiev R.Z., Kozlov E.V., Ivanov Y.F., Lian J., Nazarov A.A., and Baudalet B., *Acta Metall. Mater.* **42**, 2467 (1994).
183. Li H.Q., Master's Thesis, University of Science and Technology at Beijing, 1997.
184. Matlock D.K., Zia-Ebrahimi F., and Krauss G., *Deformation Processing and Structure*, Mater. Sci. Seminar, ASM Publication, Metals Park, OH, 1984, p47.
185. Gutkin M.Y., Ovid'ko I.A., and Skiba N.V., *Acta Mater.* **51**, 4059 (2003).
186. Wang Y.W., Wang K., Pan D., Lu K., Hemker K.J., and Ma E., *Scripta Mater.* **48**, 1581 (2003).
187. *ASM Metals Handbook*, ASM International, ed. 10, Materials Park, OH, 1990, vol. 1, p435.
188. *ASM Handbook: Fatigue and Fracture*, ASM International, ed. 10, Materials Park, OH, 1996, vol. 19, p462 and p385.
189. Meyers M.A., and Chawla K.K., *Mechanical Metallurgy: Principles and Applications*, Prentice Hall, Inc., Englewood Cliffs, NJ, 1984.
190. Van Swygenhoven H., *Science* **296**, 66 (2002).
191. Van Swygenhoven H., Caro A., and Farkas D., *Scripta Mater.* **44**, 1513 (2001).
192. Keblinski P., Wolf D., Phillpot S.R., and Gleiter H., *Scripta Mater.* **41**, 631 (1999).
193. Kim H.S., Estrin Y., and Bush M.B., *Acta Mater.* **48**, 493 (2000).
194. Ovid'ko I.A., and Sheinerman A.G., *Acta Mater.* **52**, 1201 (2004).
195. Günther B., Kumpmann A., and Kunze H.-D., *Scripta Metall. Mater.* **27**, 833 (1992).
196. Hibbard G.D., McCrea J.L., Palumbo G., Aust K.T., and Erb U., *Scripta Mater.* **47**, 83 (2002).
197. Burke J.E., *Trans. Metall. Soc. AIME.* **180**, 73 (1949).
198. Smith C.S., *Trans. Metall. Soc. AIME.* **175**, 15 (1948).

199. Burke J.E., and Turnbull D., Prog. Metal Phys. **3**, 220 (1952).
200. Smithells Metals Reference Book 7th ed., edited by Brandes E.A, Brook G.B., Butterworth-Heinemann Ltd., Boston, 1992, p13-82 and p13-117.
201. Grey E.A., and Higgins G.T., Acta Metall. **21**, 309 (1973).

BIOGRAPHICAL SKETCH

Hongqi Li was born in Henan Province, P.R. China, on May 12, 1972. He received his B.E. and M.E. degrees from the Materials Physics Department of the University of Science and Technology at Beijing in 1995 and 1997, respectively. After graduation, he continued toward his Ph.D. study in the same university until August 2000, when he was admitted to the Department of Materials Science and Engineering of the University of Florida to begin his current Ph.D. career in Dr. Ebrahimi's research group.